Noise Generation from Expansion Devices in Refrigerant

G. M. Singh, E. Rodarte, N. R. Miller and P. S. Hrnjak

ACRC TR-152 July 1999

For additional information:

Air Conditioning and Refrigeration Center
University of Illinois
Mechanical & Industrial Engineering Dept.
1206 West Green Street
Urbana, IL 61801

(217) 333-3115

Prepared as part of ACRC Project 72
Modes of Propagation of an Acoustic Signal from
Expansion Devices and Investigation of Possible Attenuation
P. S. Hrnjak and N. R. Miller, Principal Investigators

The Air Conditioning and Refrigeration Center was founded in 1988 with a grant from the estate of Richard W. Kritzer, the founder of Peerless of America Inc. A State of Illinois Technology Challenge Grant helped build the laboratory facilities. The ACRC receives continuing support from the Richard W. Kritzer Endowment and the National Science Foundation. The following organizations have also become sponsors of the Center.

Amana Refrigeration, Inc.
Brazeway, Inc.
Carrier Corporation
Caterpillar, Inc.
Chrysler Corporation
Copeland Corporation
Delphi Harrison Thermal Systems
Frigidaire Company
General Electric Company
Hill PHOENIX
Honeywell, Inc.
Hussmann Corporation
Hydro Aluminum Adrian, Inc.
Indiana Tube Corporation
Lennox International, Inc.
Modine Manufacturing Co.
Peerless of America, Inc.
The Trane Company
Thermo King Corporation
Visteon Automotive Systems
Whirlpool Corporation
York International, Inc.

For additional information:

Air Conditioning & Refrigeration Center
Mechanical & Industrial Engineering Dept.
University of Illinois
1206 West Green Street
Urbana IL 61801

217 333 3115

Table of Contents

Chapter Page

Appendix

Chapter 1

Introduction

1.1 Background

For a number of years, it has been known that flow control and throttling valves can be a significant source of noise in industrial facilities. It has also become evident that the expansion device in refrigeration systems can also be a significant source of noise. Literature reviews and personal accounts have yielded reports of a variety of expansion noises, from cavitation-induced noise in control valves of water systems, to the popping of vapor bubbles in the capillary tubes of household refrigerators, to the hissing at the exit of orifice tubes in automotive air conditioning systems, to tonal noises at the exit of large industrial control valves throttling air. In many cases such noise can be distracting, annoying, and sometimes, as in the latter case, dangerous. Much work has been done on noise from control valves in air and water systems [1] but very little work has been done to date on noise from expansion devices in refrigeration systems.

Expansion noise can be generated by the mechanical vibration of the expansion device or by the aerodynamic noise generated within the fluid flow. The mechanical vibrations can be flow-induced or due to the relative motion of mechanical components. The aerodynamic noise, a combination of shear, turbulence, and/or shock wave interaction [1,2], can be generated within the expansion device or at the exit. This aerodynamic noise can then propagate downstream and interact with downstream components, such as piping and heat exchangers, inducing vibrations and, in some cases, even resonance. Mechanical vibrations of the device itself can also travel downstream through connected solid components and interact with the flow-induced vibrations and the aerodynamic noise. All of these vibrations in the system can then propagate as sound waves through the air and become air-borne noise that we can hear. These phenomena are illustrated in Figure 1.1.

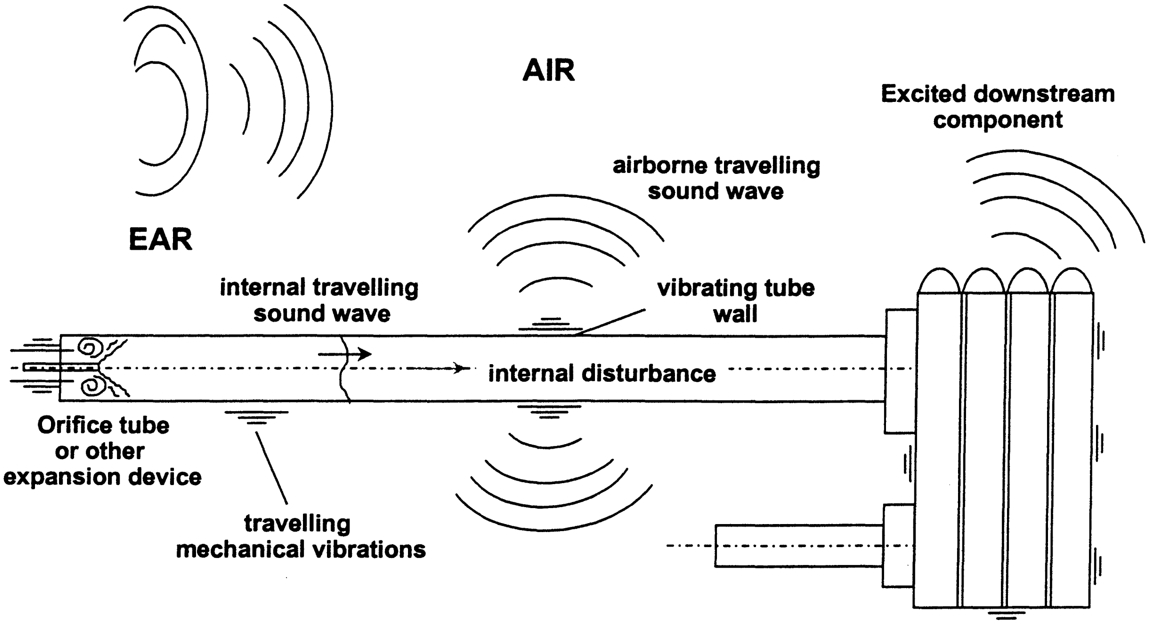

Figure 1.1 – Overview of expansion noise

Investigation of expansion noise in refrigerant presents many challenges. One challenge is to understand the specific operating conditions (mass flow rate, inlet and outlet pressure, temperature, subcooling, quality, or superheat) that generate the most significant noise and what type of expansion device is noisiest given those conditions. Making measurements of expansion noise in refrigerant can be challenging, as well. If internal sound pressure measurements are desired, the microphones must be able to withstand the high static refrigerant pressure, yet sensitive enough to measure the dynamic sound pressure of the expansion noise above the static pressure of the refrigerant. Using microphones to measure internal sound pressure also means a method must be devised to mount the microphone diaphragms internal to the flow without disturbing the flow or allowing refrigerant leakage to the environment. Further, vibrations, reflected sound waves, and other disturbances to noise measurements must be minimized and accounted for in the data. Finally, natural system inconsistencies such as pressure and mass flow rate oscillations generated by the pump must also be minimized.

1.2 Objectives and scope

The objectives of this project are to experimentally measure the downstream internal sound pressure and external pipe wall vibrations from a variety of expansion devices over a wide range of operating conditions, investigate the attenuation of acoustic energy with propagation, investigate the interaction of expansion noise with other system components, and explore the physical mechanisms of the noise generated by expansion devices. The overall goals of this project are to develop a set of procedures for predicting the noise propagated to the environment from expansion devices and to gain a better understanding of expansion noise generation and propagation mechanisms.

1.3 Operation of expansion devices

An expansion device is, generally, a device which generates a rapid and significant pressure drop in the working fluid of a system. Examples of some of the most commonly used expansion devices in refrigeration systems are shown in Figure 1.2. All expansion devices generate a pressure drop due to the sudden contraction and expansion of the fluid at the inlet and exit of the device, respectively. There may be additional pressure drop due to friction along the length of the device for expansion devices with extended interiors. Most expansion devices are assumed to be isenthalpic or nearly isenthalpic.

1.3.1 Orifice plate

An orifice plate generates a pressure drop due to the sudden contraction and sudden expansion of the fluid at the inlet and exit of the plate, respectively. This pressure drop is, in general, a function of the fluid, the outer tube diameter, and the orifice diameter. Equations to calculate the pressure drop trough an orifice can be found in fluid mechanics and duct design handbooks such as [3] and [4].

1.3.2 Orifice tube

An orifice tube is basically just an extended orifice plate. Pressure drop is generated by contraction and expansion at the inlet and exit of the tube, but since the tube is of extended length, additional pressure drop is achieved by friction along the length of the tube. The inlet and outlet pressure drop relations are similar to those for an orifice plate and can also be found in [3] and [4]. The length of the tube is just a constant-diameter pipe and the pressure drop along the length can be evaluated for pure vapor flow or liquid flow using known pipe-flow pressure-drop laws (Fanno flow, Moody charts, Orifice [Bernoulli] equation) as found in [3], [5], and [6]. When two-phase flow is present and the flow is choked (as is normally the case for two-phase flow), empirical or semi-empirical methods must be used. An excellent reference on orifice tube flow and choked-flow models for orifice tubes is [7].

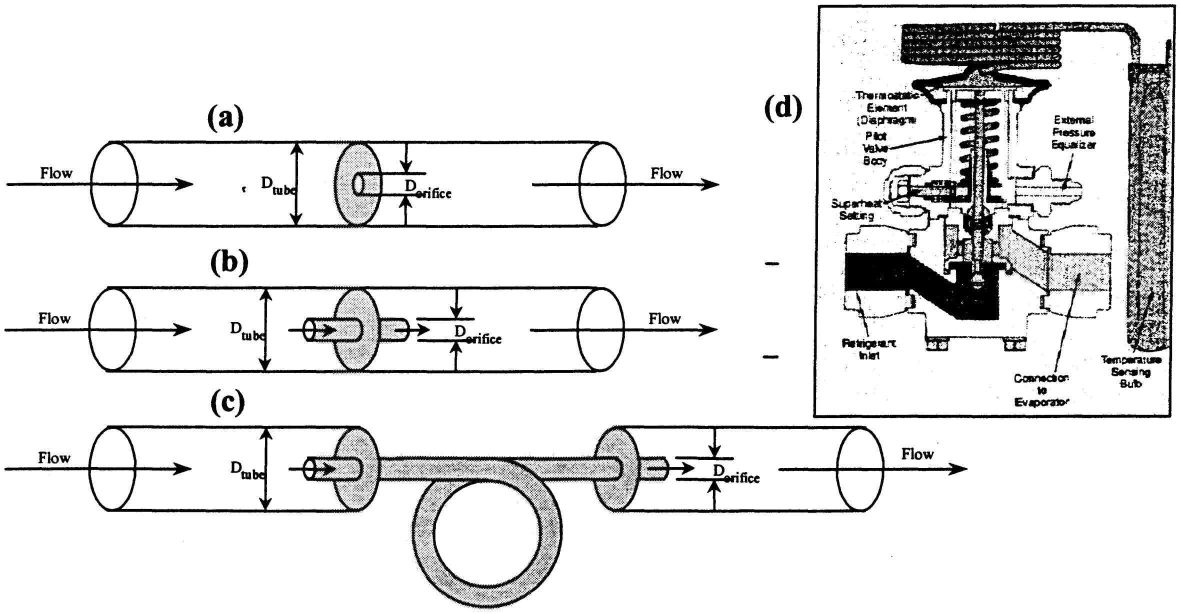

Figure 1.2 – An illustration of some commonly used refrigeration expansion devices
a) Orifice plate b) Orifice tube c) Capillary tube d) Thermostatic Expansion Valve (from [33])

1.3.3 Capillary tube

A capillary tube is just a very long orifice tube. Thus, a larger fraction of the total pressure drop is accomplished via friction in a capillary tube compared to an orifice tube. Inlet, outlet, and frictional pressure drop for pure liquid and vapor flow can be evaluated in the same manner as for an orifice tube. A very good reference for determining cap tube friction factors is [8]. Choked two-phase flow requires a cap tube model such as in [8].

1.3.4 Expansion valves

Expansion valves, like the thermostatic expansion valve shown in Figure 1.2, generate pressure drop by sudden contraction and expansion, and are often treated as isentropic, as well as isenthalpic. Valves, unlike orifice plates or tubes, can change the opening of their effective orifice diameter. There are many types of expansion valves, including ball valves and thermostatic and electronic expansion valves. Ball and globe valves (and similar types of valves) can change their orificial openings manually. Thermostatic expansion valves can change their openings automatically in response to the exit temperature of the downstream evaporator. Electronic expansion valves can change their openings by a manual or automatic change of a control signal applied to the valve.

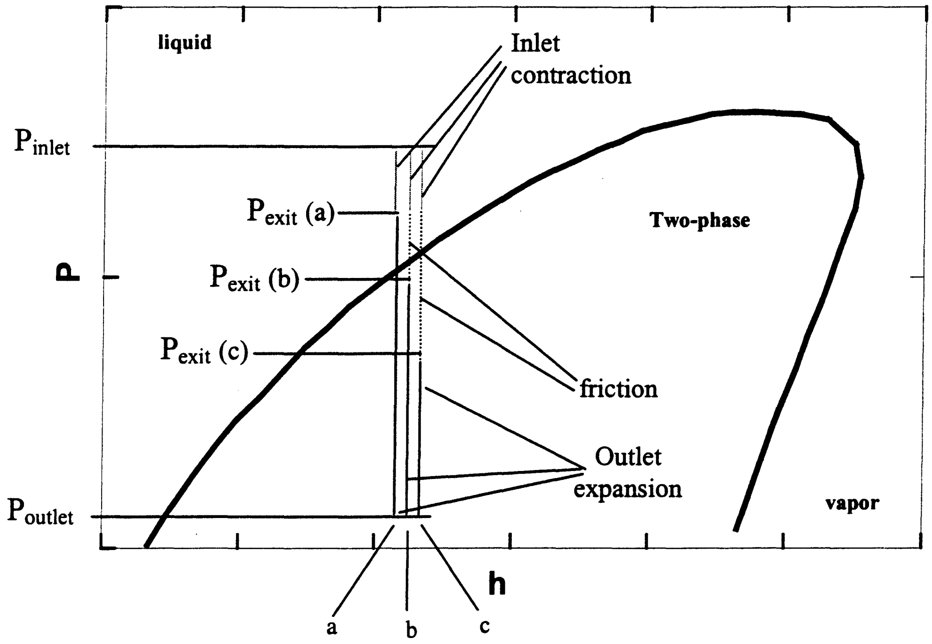

Figure 1.3 – A qualitative illustration of three typical expansion processes on a pressure-enthalpy diagram.

a) Expansion valve b) Orifice tube c) Capillary tube

A qualitative illustration of the expansion process on a Pressure-Enthalpy diagram for orifice tubes, capillary tubes, and expansion valves is given in Figure 1.3. Note the relative influence of frictional pressure drop for each expansion device. It is also important to note that when a non-isentropic expansion device is choked, as is usually the case for compressible fluids, the friction may actually drive the exit-plane pressure (P_{exit}) *below* the downstream or outlet pressure (P_{outlet}). An example of this is shown in Figure 1.4. The effect of this is to cause the refrigerant to increase in pressure, or recompress, after it exits the device.

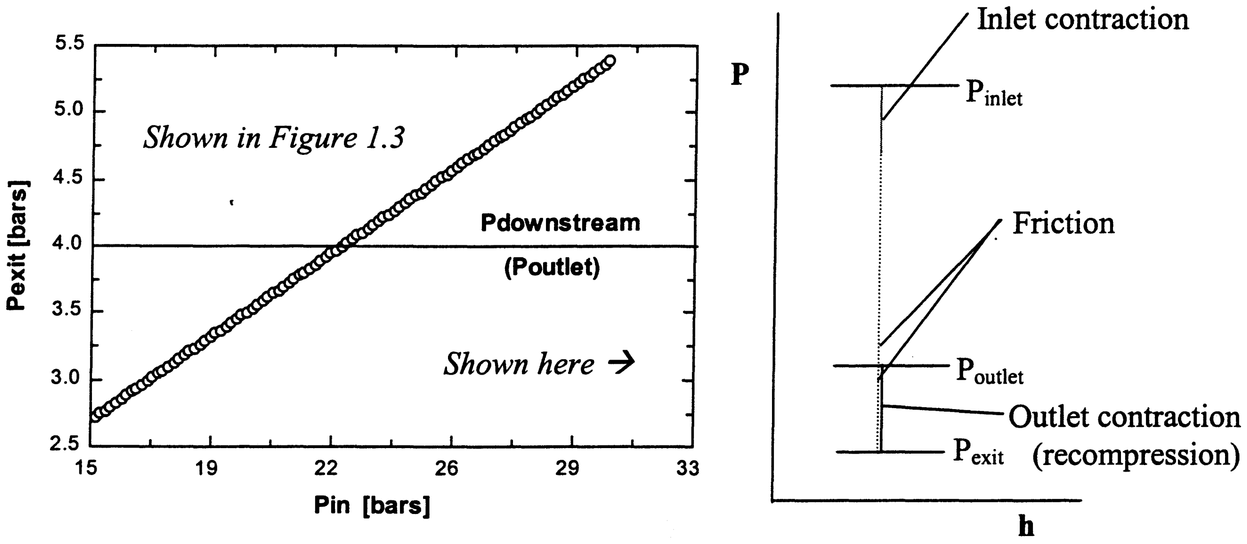

Figure 1.4 - Recompression after the exit of an expansion device

(Calculated for an ideal gas through a choked capillary tube, $f = 0.003$, $\gamma = 1.07$, $D = 1.626$mm, $L = 127$in. Calculations done as described in Appendix L)

1.4 Sound waves in duct flow

1.4.1 Plane waves

Sound waves are, in general, simply a density disturbance, as caused by the excitation of a source, which propagates through a fluid as a travelling series of pressure compressions and rarefactions. This is illustrated for a single-frequency noise in a duct flow in Figure 1.5.

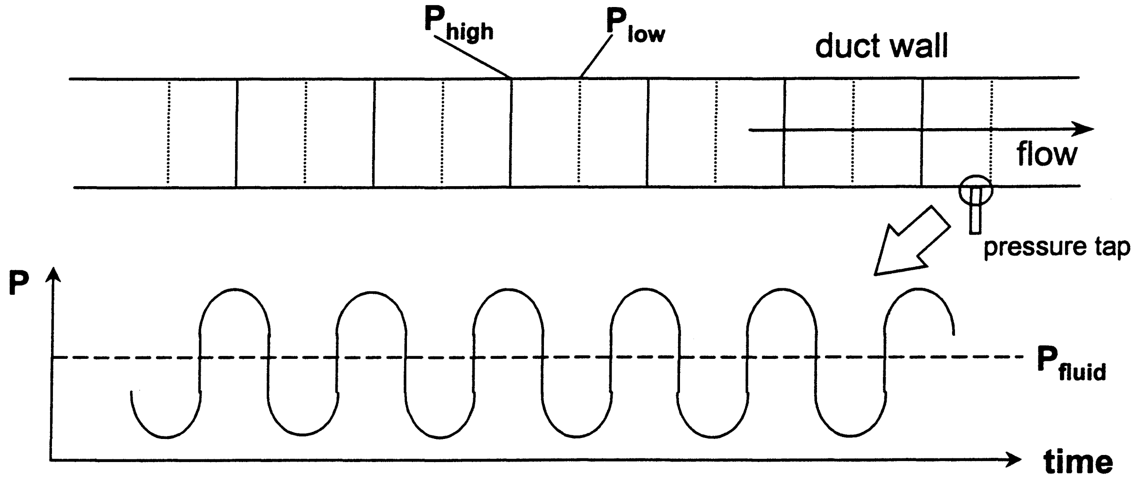

Figure 1.5 – Illustration of a single-frequency sound wave in a duct flow
P_{fluid} is the static pressure of the fluid

In general, however, sources emit sound containing many different frequencies, with sound waves generated at each emitted frequency. The low frequency sound waves in duct flow propagate as plane waves, whose wavefronts are planes of uniform sound pressure perpendicular to the direction of propagation. Plane waves are given mathematically [9] by:

$$P = P_o e^{-j2\pi fx/c(1+M)} \quad (1.1)$$

where f is the frequency of the sound wave, x is the distance along the propagation direction (duct axis, for duct flow), c is the speed of sound in the medium, and M is the mach number.

High frequency sound waves in duct flow can be of different shapes, called higher modes. Each mode has a minimum frequency above which it, and all lower modes, can propagate. The frequency below which only plane waves can propagate is called the first cut-off frequency and is given by

$$f_{cutoff} = .586c/d \quad (1.2)$$

where d is the diameter of the (circular) tube. Thus for a measured sound in a duct flow, all of the sound waves below the first cut-off frequency propagate as plane waves and all the sound waves above that frequency propagate as plane waves plus higher order modes (waves of more complex shapes).

In a duct, plane waves can be disturbed out of their planar shape by some obstruction or other disturbance, but will return to a planar shape within 2-3 duct diameters [10]. Also, as plane waves travel along the duct they will attenuate with distance, i.e. the magnitude of their sound pressure will decrease with distance. Both of these concepts are illustrated in Figure 1.6.

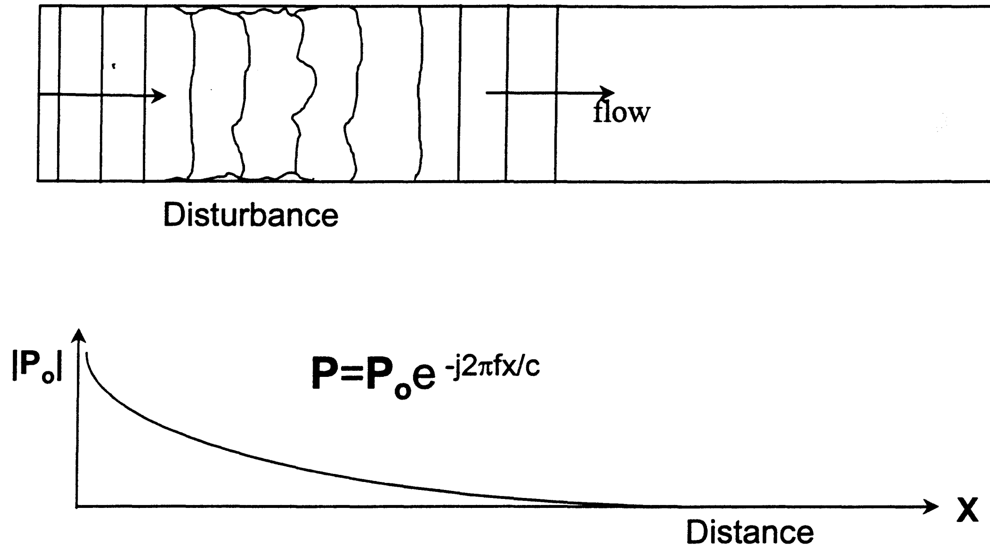

Figure 1.6 – Disturbance and attenuation of plane waves in duct flow

It should be noted that there are many mechanisms of sound wave attenuation with distance in a tube, including friction, turbulence, and heat transfer effects. Also, sound wave attenuation is a function of frequency, as well. As such, the actual attenuation curve for a given duct flow and frequency will likely be different from the profile sketched in Figure 1.6. Much more on sound wave attenuation can be found in [11].

1.4.2 Reflections and standing waves in a duct

When sound waves travel inside a tube any area change, medium change, or physical disturbance to the flow (such as sharp bends or elbows) creates reflections [9]. This is illustrated in Figure 1.7. Simply stated, only an infinite, smooth tube filled with a constant-property medium will be free of reflections.

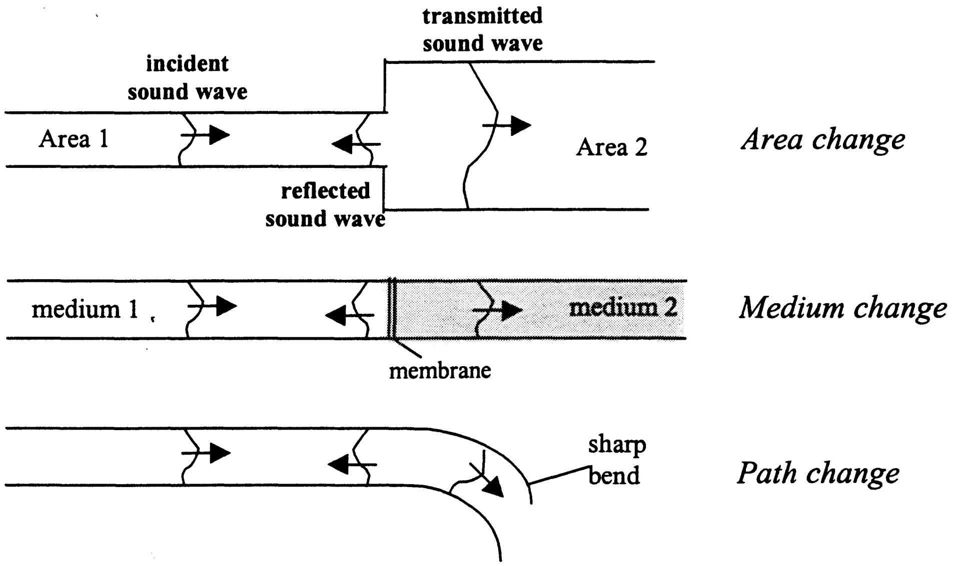

Figure 1.7 – Possible sources of reflection of sound waves in duct flow

When incident and reflected sound waves in a tube interact they form a standing wave pattern in the tube [12]. Standing waves in a tube, like standing waves on a string, will form only at discrete frequencies related to the tube length [9,12,13]. When both the incident and reflected waves are plane waves (e.g. for all waves with frequency below the first cut-off), any standing waves will be plane waves given mathematically by

$$\mathbf{P(f,x)=P_i(f)e^{-j2pfx/c(1+M)}+P_r(f)e^{j2pfx/c(1-M)}} \qquad (1.3)$$

where P(f, x) is the Fourier Transform of the measured acoustic pressure at location x, P_i (f) is the Fourier Transform of the incident acoustic pressure at x, P_r (f) is the Fourier Transform of the reflected acoustic pressure at x, and f is the frequency of the wave.

Standing waves in a duct, like standing waves on a vibrating string, will have peaks and nodes. An internal sound measurement will measure the standing wave pattern at that point. Since reflections are a function of the physical set-up of the system, every system will produce a different standing wave pattern for a given incident acoustic signal. Therefore, every system may give a different measurement of internal sound pressure for a given incident acoustic signal at every point downstream of the expansion device. Since standing waves can only be generated when reflections are present, reflections from downstream components must be eliminated or accounted for in measurements of internal sound pressure.

1.4.3 Coherence

Coherence is a measure of agreement between the sound pressures measured at two different microphones. The mathematical definition of coherence [14] is:

$$\gamma^2 = \frac{G_{12} G_{12}^*}{G_{11} G_{22}} \qquad (1.4)$$

where $G_{11}=F_1F_1^*$ is the power spectrum measured at microphone 1, $G_{12}=F_1F_2^*$ is the cross-spectrum between microphones 1 and 2, F stands for the Fourier Transform of the measured sound pressure and (*) indicates the complex conjugate.

A coherence of unity (1) at a given frequency means perfect agreement between the sound pressures at that frequency, i.e. the two sound pressures were identical at that frequency at that instant of time. Coherence, by definition, is on the range 0-1 and a coherence of zero means the two measured signals are totally incoherent. If the two microphones are perfectly (or nearly) matched, then all sound waves in the plane wave region (i.e. sound waves whose frequencies are below the first cut-off frequency) should have a coherence of one when measured between two microphones in the same plane (or spaced closely apart, assuming the sound pressure attenuation between them is negligible).

Chapter 2

Experimental Test Facility

A simplified schematic of the experimental test facility is shown in Figure 2.1. Low-pressure liquid refrigerant (State 1) is pumped nearly isenthalpically by a diaphragm pump to a high-pressure liquid (State 2). A diaphragm pump is used to allow for unrestricted oil and oil concentration adjustment and to provide high pressure ratios. The pump speed is controlled by an attached variable frequency drive. Following the pump is a standard pulsation damper. The pulsation damper uses a chamber of compressed gas (Nitrogen, in our case) surrounding a flexible refrigerant tube to help quell pulsations, as illustrated in Figure 2.2.

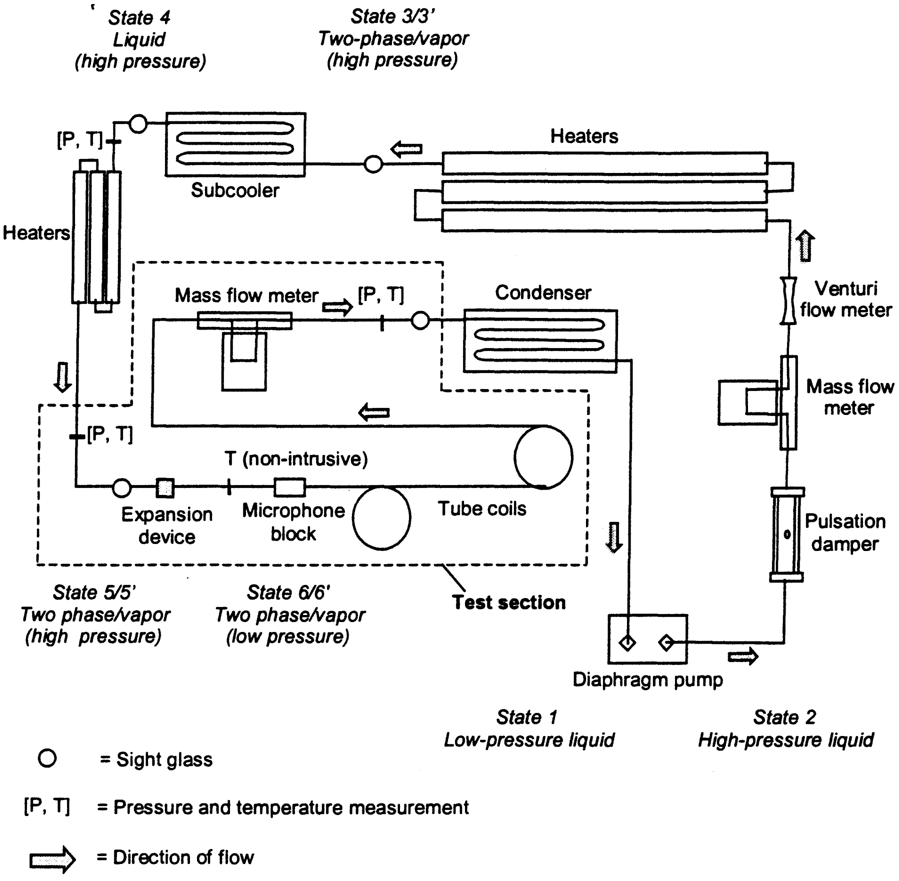

Figure 2.1 - Simplified schematic of experimental test facility

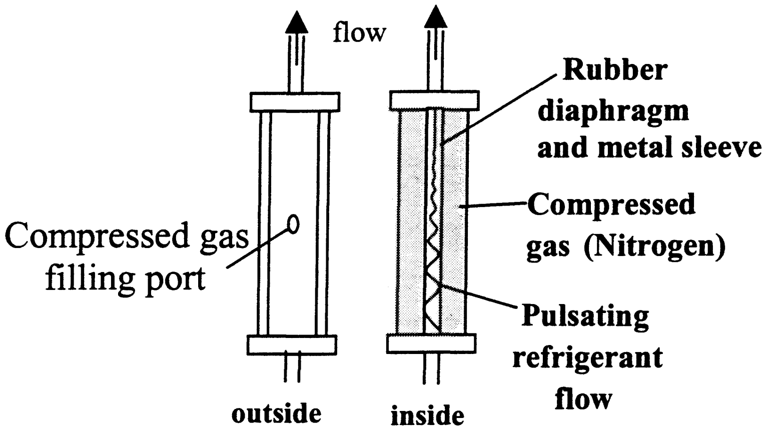

Figure 2.2 - Simple schematic of pulsation damper

Following the pulsation damper is a mass flow measurement on the system's high-pressure side. After the flow meter, the liquid refrigerant is heated to a two-phase condition (State 3) or a superheated vapor condition (State 3') at the system's high pressure. The refrigerant is then condensed back to liquid and subcooled at the system's high pressure (State 4). The idea behind partially or fully vaporizing the refrigerant before subcooling it again is to provide a "vapor cushion" between the heaters and the subcooler to absorb pressure pulsations generated by the pump. The vapor cushion and pulsation damper are meant to compliment each other and provide adequate damping to keep the pressure and mass flow rate to the expansion device steady during steady-state operation of the system. The subcooler is a co-axial heat exchanger cooled by a water-potassium formate mixture which is itself cooled by a dual-chiller system.

After condensation and subcooling, the refrigerant is again heated to a two-phase condition (State 5) or a pure vapor condition (State 5'). The purpose of these heaters is to control the state of the refrigerant at the inlet of the test section. The test section is supported by vibration isolators in order to minimize the transmission of vibrations to the test section from the rest of the system. The isolators are spring-and-damper systems that limit the vibrations transmitted through them (see Appendix D). Internal sound pressure measurements are made in the test section, and a close up of this part of the test section is shown in Figure 2.3.

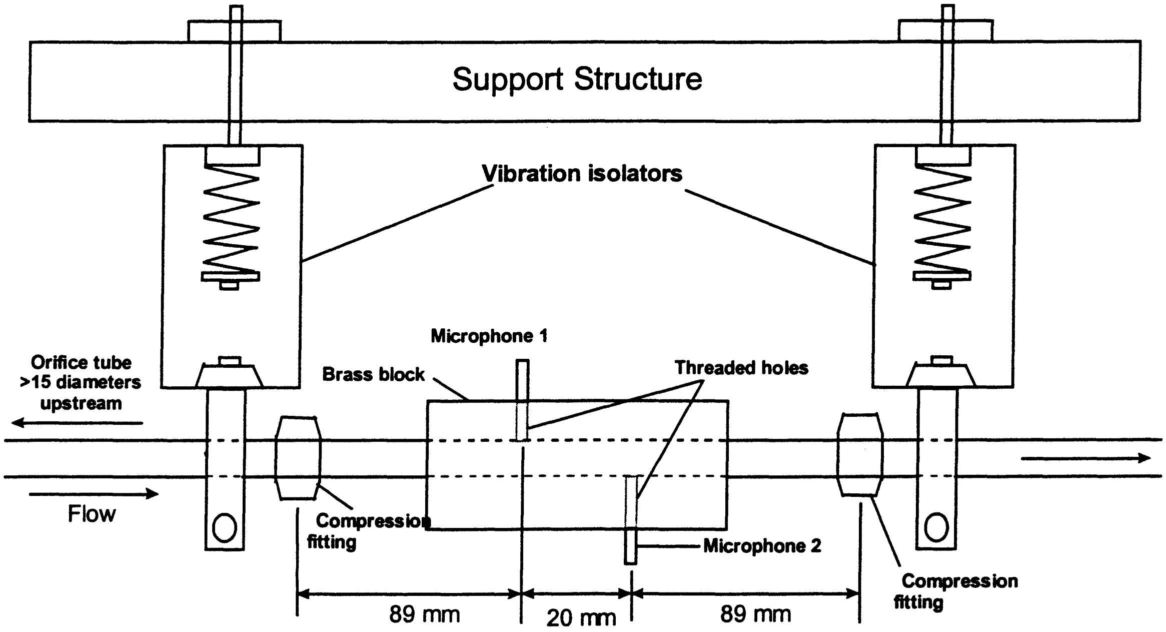

Figure 2.3 - Close up of test section

The microphones are piezoelectric pressure transducers with a high pressure limit to withstand the high static pressure of most refrigerants while still being sensitive enough to measure the internal expansion noise generated during most tests. The microphones are threaded, to allow them to seal against refrigerant leakage, and have very small, circular diaphragms (1/10in diameter), small enough to mount virtually flush to the inside walls of the copper tubing in the test section (0.5in O.D./ 0.43in I.D.). Note that the microphones are mounted on opposite sides of the tube. This was done to help avoid any flow disturbances generated in the wake of the first microphone from affecting the measurements taken by the second microphone. Two microphones are used (rather than one) to check for flow disturbances using coherence measurements and to use the two-microphone technique (Chapter 3) to account for unattenuated reflections.

The microphone block is solid brass (its mass helping to further damp vibrations in the immediate vicinity of the microphones) with holes drilled in it to the specifications of the microphones such that when tightened, the microphones are flush to the inside tube wall. Holes the size of the microphone diaphragm are also drilled into the copper tubing which is then cleaned thoroughly such that the inside wall is smooth, clean, and free from burrs. A more detailed drawing of the block is given in Figure 2.4.

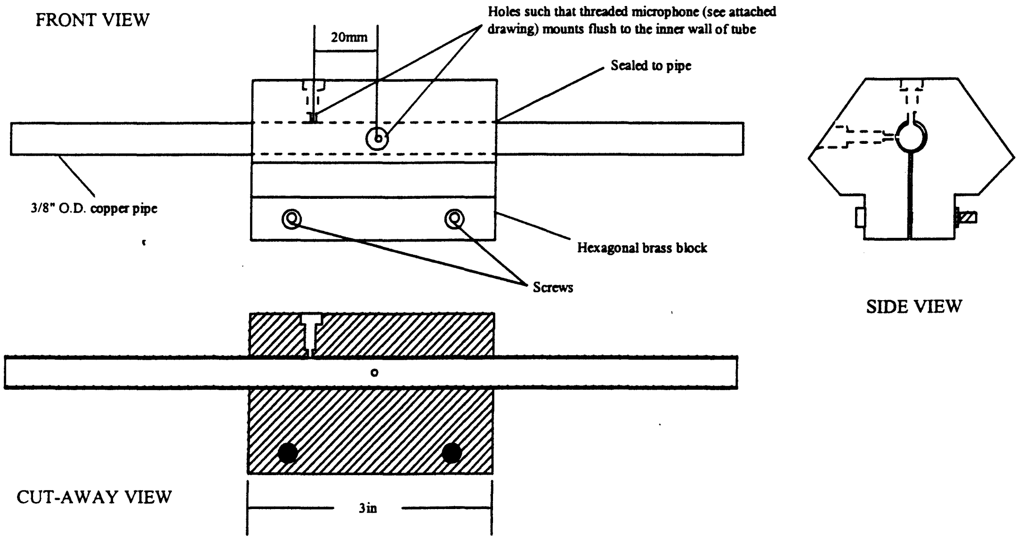

Figure 2.4 - Schematic of microphone block

Acceleration measurements are made on the tube walls about 22in. downstream of the microphone block. A hexagonal nut (about 0.25in diameter with threads to fit the accelerometer) is glued (with cyanoacrylate adhesive – i.e. "super glue") to the outside of the tube wall and the accelerometer is then screwed into the nut, as shown in Figure 2.5. When screwed in fully, the accelerometer surface is just shy of touching the pipe wall. It is assumed that the presence of the nut and glue will not affect the frequency content of the acceleration spectra. The same set-up was used for all acceleration measurements. A lightweight hexagonal nut is provided for mounting as such by the accelerometer manufacturer, although a standard hexagonal nut can also be used.

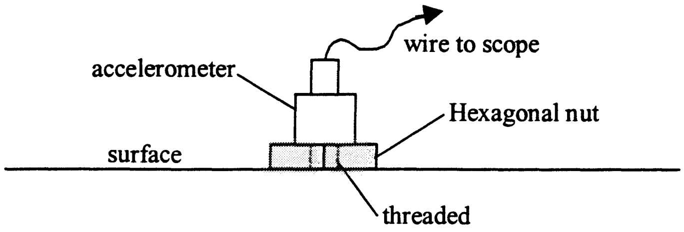

Figure 2.5 - Accelerometer mounting

After expansion (approximately isenthalpic) the refrigerant is in a low pressure two-phase condition (State 6) or a pure vapor condition (State 6'), depending on the inlet conditions and the expansion device. An insulated surface thermocouple 15cm downstream of the expansion device gives the outlet temperature from the device in steady state, assuming a negligible temperature gradient between the outer tube wall and the refrigerant. The thermocouple is attached to the tube wall with aluminum thermocouple epoxy and insulated >0.5in radially and 4in. axially around the tube. Experiments have confirmed the validity of this procedure (see Appendix J). A surface thermocouple is used here because an intrusive measurement at this point might generate flow disturbances which could interfere with the noise measurements.

Downstream of the expansion device there is a long section of coiled tubing (approx. 24m in length) to attenuate sound waves reflected from downstream components. The tubing is smooth and the radius of the coils is much greater (>24x) than the tube diameter, meaning the coils act as a long section of straight, smooth pipe, attenuating sound waves without generating reflections. The pressure loss in the tubing is assumed negligible (as confirmed by experiment – see Appendix C) and the outlet pressure from the expansion device is then taken to be the pressure measured downstream of the coils.

Following the coils is another flow meter, providing a measurement of mass flow rate on the low-pressure side. These measurements are only valid for single-phase vapor and are used only as a rough check on the upstream flow meters. The refrigerant is then condensed to a liquid at the system's low pressure (State 1) and returned to the pump. The condenser is also a co-axial heat exchanger cooled by a water-potassium formate mixture cooled by the same dual-chiller system as the subcooler.

The pump is mounted on a vibration isolator, as sketched in Figure 2.6. Since the pump and other parts of the system touch the floor, this action was intended to limit the transmission of vibrations from the pump to the rest of the system via the floor. Further, the inlet and outlet piping connections from the pump to the system are flexible and should naturally limit some of the transmission of vibration through piping connections. Additionally, the section of tubing following the pump but before the first heaters (see Figure 2.1), which originally rested on the structure and often vibrated in response to pump operation, was hung from the ceiling with flexible rubber supports so as to no longer rest on the structure at any point. All of these actions were taken to limit transmission of vibrations to the test section (See Appendix D).

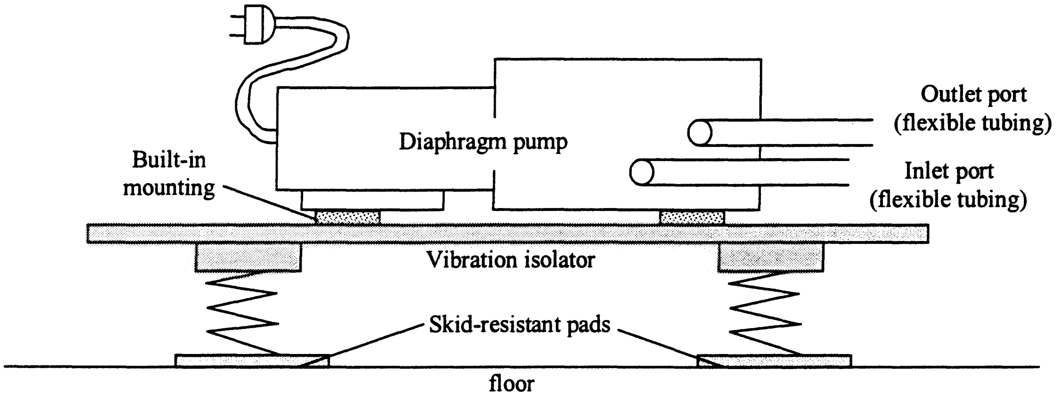

Figure 2.6 – Illustration of pump mounting

The thermodynamic cycle of the system and a more complete diagram of the loop is given in Figure 2.7. Figure 2.7 shows the additional bypasses and valves used to help control the flow and additional sight glasses between the pump and the condenser to see the level of refrigerant in the loop during charging and operation. Also shown is the pump subcooler (used to insure subcooled liquid refrigerant returns to the pump), the evaporator test section, and the atmospheric release. Although not shown, Shrader valves for charging are located at several places, both high and low and around components, but none on the test section for acoustic purposes. The exact effect of charge on the system is unknown, but a typical charge of R134a is 18lbs.

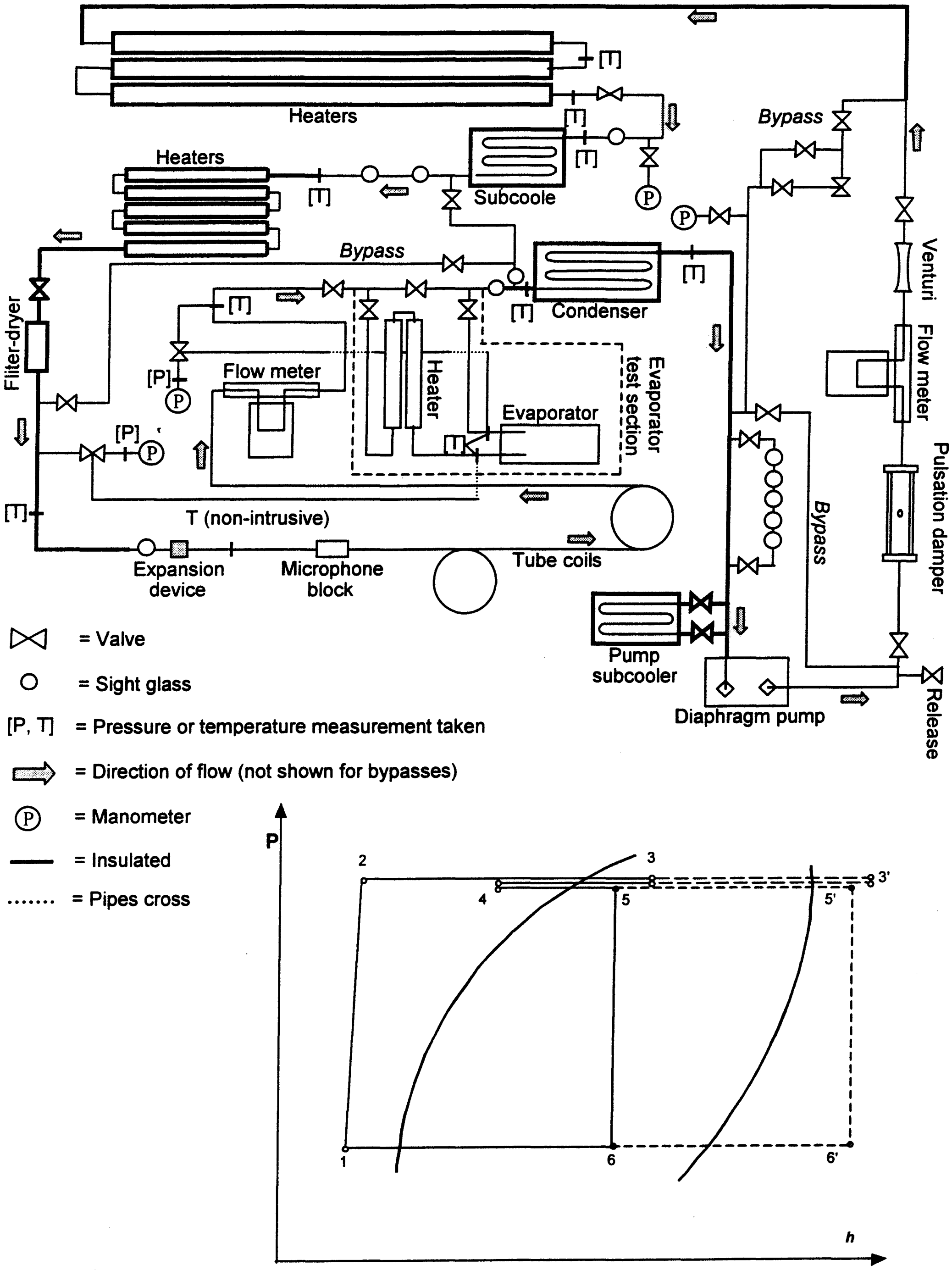

Figure 2.7 – More complete schematic and thermodynamic cycle of the experimental test facility

Chapter 3

Two-Microphone Technique

3.1 Introduction

The two-microphone technique is a mathematical procedure for separating a measured sound pressure into its incident and reflected components, for all frequencies below the first cut-off frequency. This method is completely theoretical, derived entirely from first principles and definitions (i.e. no empirical components), and works for any stationary signal. All that is required is the sound pressure measured at one of two calibrated microphones spaced a short distance apart (measuring the same travelling sound wave) and the measured transfer function between them.

3.2 Summary of the Two-Microphone Technique

Consider a tube filled with a fluid (mean flow or stationary) with some sound source at one end and some means of reflection at the other end as shown in Figure 3.1.

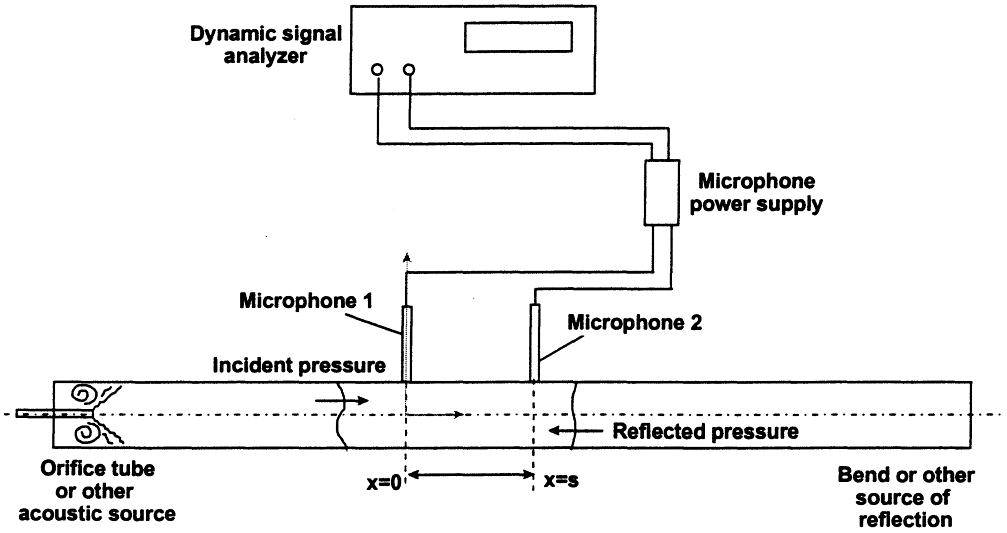

Figure 3.1 - Two-microphone set-up

Because there are both incident and reflected waves at each point in the tube, a standing wave pattern is established in the tube (See Chapter 1). If the sound waves through the fluid are plane waves and conditions are lossless and one-dimensional down the axis of the tube, the pressures at x=0 (microphone 1) and x=s (microphone 2) are given by:

$$P_1(f) = P_i(f) + P_r(f) \tag{3.1}$$
$$P_2(f) = P_i(f)e^{-jk_i s} + P_r(f)e^{jk_r s} \tag{3.2}$$

where

$$k_i = k/(1+M) = 2\pi f/c(1+M) \text{ and } k_r = 2\pi f/c(1-M) \tag{3.3}$$

P_1 = Fourier transform of acoustic pressure at x=0
P_2 = Fourier transform of acoustic pressure at x=s
P_i = Fourier transform of incident component of standing wave
P_r = Fourier transform of reflected component of standing wave
k = Wave number
k_i = Wave number in incident direction (+x)
k_r = Wave number in reflected direction (-x)
M = Mach number averaged over the cross-sectional area (assumed constant along axis)
c = Speed of sound in fluid (assumed constant throughout fluid)
f = Frequency
s = Microphone spacing

Without mean flow, these equations reduce to:

$$P_1(f) = P_i(f) + P_r(f) \tag{3.1}$$
$$P_2(f) = P_i(f)e^{-jks} + P_r(f)e^{jks} \tag{3.2b}$$

where

$$k = 2\pi f/c \tag{3.3b}$$

Thus if s and M are known, a signal analyzer can measure the Fourier transforms of the acoustic pressures at both microphones and Equations (3.1)-(3.3) can be solved for the Fourier transforms of the incident and reflected pressures. The Fourier transform of an acoustic pressure is simply the measured sound pressure spectrum in the frequency domain.

Measurement of the acoustic pressures at both microphones, however, requires a gain and phase calibration of the two microphones. To avoid this calibration, Blaser and Chung [15,16,17] looked at the acoustic pressures at both microphones in terms of the transfer functions between them:

$$H_{12} = P_2/P_1 \tag{3.4}$$

$$H_{12i} = P_{2i}/P_{1i} \tag{3.5}$$

$$H_{12r} = P_{2r}/P_{1r} \tag{3.6}$$

$$R_1 = P_{1r}/P_{1i} \tag{3.7}$$

$$R_2 = P_{2r}/P_{2i} \tag{3.8}$$

H_{12} = Transfer function between both microphones
H_{12i} = Transfer function between incident component at each microphone
H_{12r} = Transfer function between reflected component at each microphone
R_1 = Complex reflection coefficient at first microphone
R_2= Complex reflection coefficient at second microphone

Blaser and Chung show (from *definitions,* i.e. no assumptions or simplifications made) that

$$R_1 = (H_{12} - H_{12r})/(H_{12i} - H_{12}) \tag{3.9}$$

and for plane waves and no loss between the microphones

$$H_{12i} = e^{-jk_i s} \text{ and } H_{12r} = e^{jk_r s} \qquad (3.10)$$

Thus if s and M are known, H_{12i} and H_{12r} can be solved for by Equation (3.10). H_{12} can be measured with a signal analyzer, thus R_1 can be found from Equation (3.9) and Equations (3.5)-(3.8) can be solved for the incident and reflected components of the standing wave. Note this procedure is valid for any source of sound (e.g. random, pulsed, transient, broadband, or discrete).

To avoid calibration of the microphones, a "sensor-switching" technique is employed. H_{12} is measured, the microphones are switched (all other conditions kept constant), and H_{12} is measured again. A correction factor accounting for the differences in gain and phase measured by the two microphones is then simply the geometric mean of the two measurements:

$$H_c = (H^o_{12} \bullet H^s_{12})^{1/2} \qquad (3.11)$$

H_c = Gain and phase correction factor between the two microphones
H^o_{12} = H_{12} measured with microphones in original positions
H^s_{12} = H_{12} measured with microphones in switched positions

The microphones should now be returned to their original positions. For all subsequent measurements then,

$$H_{12,\,\text{corrected}} = H_{12,\,\text{measured}}/H_c \qquad (3.12)$$

It must be reiterated that this technique for decomposition of the standing wave in the tube is only valid for plane waves. At a high enough frequency (above the first cut-off frequency), higher modes (i.e. not plane waves) will propagate in the tube. For a tube of circular cross-section, this frequency is given by

$$f_{cutoff} = 0.586c/d \qquad (3.13)$$

where d = Inner diameter of the tube

For frequencies less than this cut-off frequency, any higher modes propagating in the tube will decay exponentially into a plane wave within a propagation distance of one tube diameter [10]. Thus the microphones should not be closer than one diameter to the sound source or the reflecting source.

Equation (3.9) becomes indeterminate when $ks = n\pi(1-M)$, $n = 1,2,3\ldots.$ Thus to avoid all of these cases, the microphone spacing should be chosen such that

$$s < c(1-M)/2f_m \qquad (3.14)$$

where f_m is the frequency below which you wish to solve for the reflected and incident components of the standing wave (provided that frequency is less than the first cut-off frequency). However, the closer the spacing, the more likely near-field interference effects between the microphones will occur and the greater the relative error introduced in the measurement of s. Since the actual acoustic centers of the microphones are not exactly known - the smaller the diameter of the microphone, the smaller this uncertainty becomes.

3.3 Implementation of the Two-Microphone Technique in Refrigerant

Implementation of the two-microphone technique in any duct flow (including refrigerant) can be summarized as follows:

Assumptions

- Negligible attenuation between the microphones (this implies clean, smooth tube walls, a low-loss fluid, and a short distance between the microphones)
- Constant speed of sound in fluid (no spatial gradients)
- Constant mean velocity (no axial gradients)
- Microphones flush to tube inner wall

Initial Set-Up

- Set up the system as shown in Figure 3.1 with microphones flush to inner wall of tube
- Measure s. Make sure s is in accordance with Equation (3.14).
- Determine H_c as described by Equation (3.11)

For all subsequent measurements

- Allow system to come to steady state at desired operating conditions
- Measure H_{12}
- Correct H_{12} using H_c and Equation (3.12)
- Measure M
- Solve Equation (3.10) for H_{12i} and H_{12r}
- Solve Equation (3.9) for R_l
- Solve Equations (3.5)-(3.8) for the Fourier transforms of the incident and reflected components of the standing wave in the tube

In general, the two-microphone technique works best when the reflections are known to be small [18,19]. Finally, the ASTM standard [10] notes the signal-to-noise ratio must be greater than 10dB.

Details of the microphone calibration are given in Appendix F and experimental results of the two –microphone technique used in the measurement of expansion noise in refrigerant are given in Appendix C.

Chapter 4

Control valve aerodynamic noise prediction model

4.1 Control valve aerodynamic noise prediction model

The control valve aerodynamic noise prediction model of IEC standard 534-8-3:1995 [20], is a standard model developed to predict far-field (downstream) expansion noise for ideal gas flow (usually air, presumably) through large-capacity control valves used as expansion devices in industrial applications. The model is based on isentropic flow relations for ideal gases and an empirically determined "acoustical efficiency factor". The model predicts both the total (incident) internal sound pressure level inside the downstream tubing 1m from the exit of the expansion device and the sound (in dB) transmitted to the air 1m downstream of the valve exit and 1m away from the tube wall. A sketch of the setup the model describes for noise prediction is shown in Figure 4.1. Note that this set-up is identical to the test section of the experimental test facility (Chapter 2).

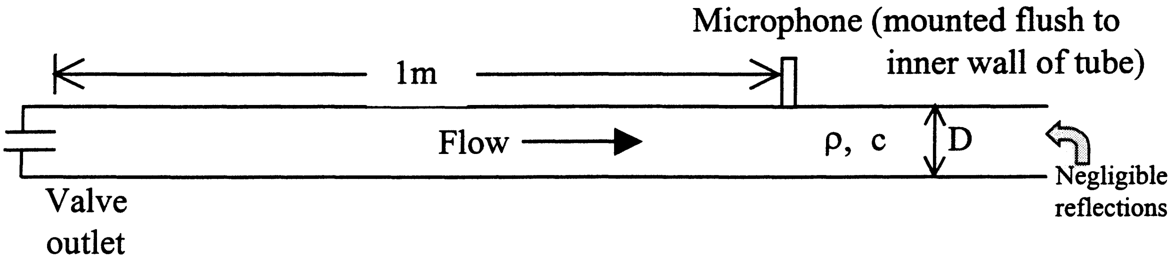

Figure 4.1 – Experimental set-up described for use of the valve noise model

The model also identifies five "regimes" of expansion noise, as shown qualitatively in Figure 4.2. Each regime has a different set of physical mechanisms of expansion noise generation and the boundaries of each regime are determined, for a given valve, by the pressure ratio across the valve. Details of the five expansion noise regimes are given in the figure and in more detail in the standard [20].

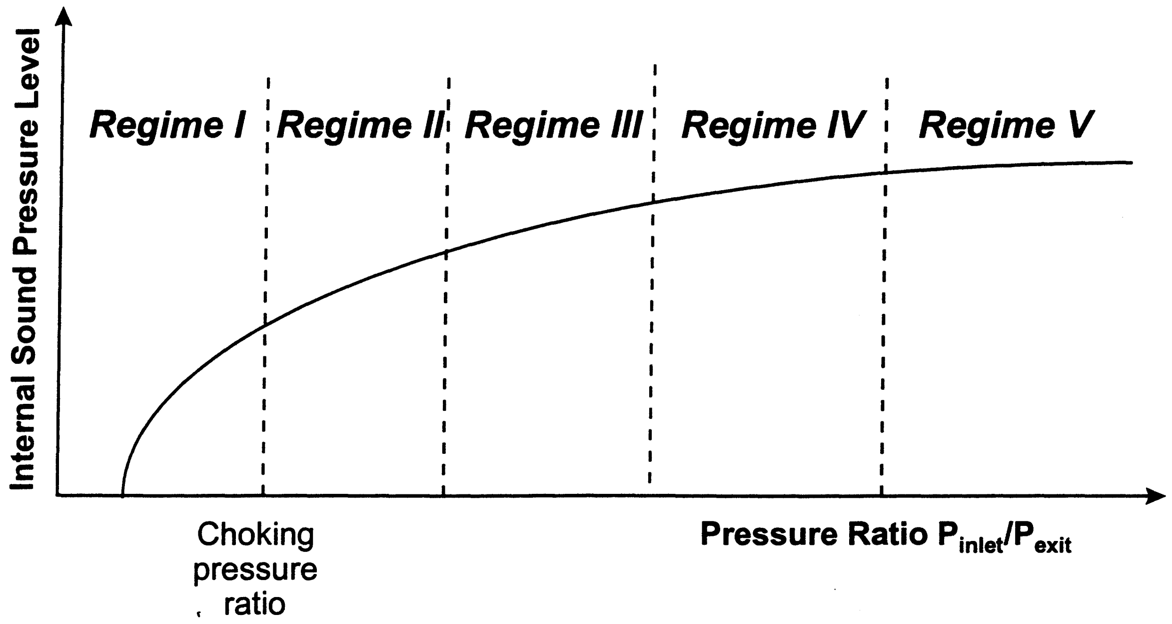

Figure 4.2 – The five regimes of downstream expansion noise

Regime I: (Unchoked flow) Isentropic recompression. *Dipole noise due to turbulent mixing.*
Regime II: (Choked flow) Isentropic recompression. *Interaction between shock cells and turbulent choked flow mixing.*
Regime III: (Choked flow) No isentropic recompression. *Turbulent flow-shear noise mechanisms.*
Regime IV: (Choked flow) Mach disc forms. *Noise mechanism is shock cell-turbulent flow interaction.*
Regime V: (Choked flow) Constant acoustical efficiency. *Decrease in* P_{exit} *will no longer increase noise*

Qualitative reproduction from [18]

The inputs to the model, as given in the standard, are: Inlet pressure to the valve, inlet density, mass flow rate, outlet pressure, the pressure recovery factor for the valve (F_L), and the valve flow coefficient (C_v). The pressure recovery factor is an experimentally determined factor which accounts for pressure recovery within the valve (see Figure 4.3). This pressure recovery, and hence F_L, are functions of the valve flow-passage geometry, including exit fittings. Many valve manufacturers provide this factor for each valve, but it can be determined experimentally by the valve owner using standard methods [21,22]. The pressure recovery factor is unity (one) for a simple orifice, orifice tube, or capillary tube in vapor flow. More details on F_L are given in the standard and its references. The valve flow coefficient is an experimentally determined factor to account for deviations of the actual valve flow rate from the theoretical maximum (isentropic) flow rate. This coefficient is itself a function of flow rate. Many valve manufacturers provide this factor for each valve at a given percentage of its maximum rated flow, but it can be determined experimentally by the valve owner using standard methods [21,22]. Correllations for the flow coefficient for an orifice, orifice tube, or capillary tube can be found in some fluid books, such as [3].

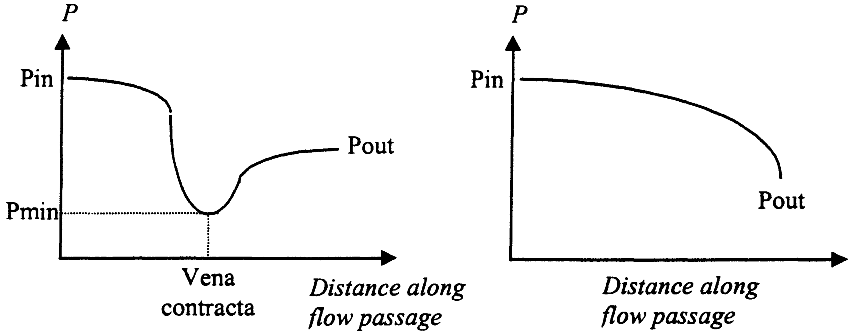

Figure 4.3 – Pressure recovery in an expansion device

Given these inputs to the model, the model uses ideal gas isentropic flow relations to calculate the outlet density, outlet speed of sound, and the velocity at the vena contracta. The vena contracta is the point of minimum area through the valve and will be the choking point in the valve if the pressure ratio across the valve is great enough. Once the velocity at the vena contracta is determined, the mechanical stream power at the vena contracta is calculated as:

$$W_{stream} = \frac{\dot{m} V^2{}_{VC}}{2} \tag{4.1}$$

If the valve is choked, the velocity at the vena contracta, V_{vc}, is the speed of sound in the fluid.

Since the vena contracta is the choking point in the flow, the mechanical stream power at that point represents all the energy generated (within the flow) by the valve available to travel downstream and/or to the surrounding environment. Some fraction of this energy is available at any point along the flow path to be converted into sound. The fraction of the mechanical stream power at the vena-contracta that goes into the internal sound power 1m downstream of the valve exit is called, by the standard, the "acoustical efficiency factor", and is a function of valve geometry (specified by F_L) and noise regime (specified by pressure ratio). Thus, the internal sound power 1m downstream of the valve exit is given as:

$$W_{sound} = \eta W_{stream} \tag{4.2}$$

where η is the acoustical efficiency factor. The equations for η in each noise regime are given below. The total internal sound pressure level at that point is then given by:

$$SPL = 10Log\left(\frac{8x10^8 \cdot W_{sound} \cdot \rho_{1m} \cdot c_{1m}}{D_{pipe}^2}\right) \tag{4.3}$$

where ρ_{1m} and c_{1m} are density and speed of sound in the fluid 1m downstream of the valve exit.

The factor $8x10^8$ in Equation (4.3) is a numerical constant which contains a factor of 0.25. This 0.25 factor is included to account for the fact that in a globe valve (see [33]), the specific valve type for which this standard was nominally written, the exit stream shoots out of the valve at an angle, toward the tube wall. As a result, as little as 25% of the sound power predicted by Equation (4.2) actually makes it 1m downstream of the valve exit, the rest being transmitted or dissipated closer to the valve exit [20,23]. It is important to note, however, that the standard can be applied to other valve types, provided that the factor of 0.25 is replaced by a more representative factor, based on the angle of the jet exiting the valve into the downstream tubing. For an expansion device whose jet exits parallel to the axis of the downstream tubing, such as an orifice, orifice tube, or capillary tube, the factor of 0.25 is replaced by 1, since 100% of the stream power can travel downstream from the valve exit [24].

4.2 Acoustical efficiency factors

Below are the "acoustical efficiency factors" for each of the five noise regimes as given by the control valve aerodynamic noise prediction model (IEC Standard 534-8-3:1995 - see above). The regimes are determined by pressure ratio across the valve as illustrated in Figure 4.2.

In Regime I:

$$\eta = 0.0001\ Ma^{3.6} F_L^2 \tag{4.4a}$$

In Regime II:

$$\eta = 0.0001\ M_j^{6.6 F_L^2} \left(\frac{P_{inlet} - P_{exit}}{P_{inlet} - P_{VC}} \right) \tag{4.4b}$$

In Regime III:

$$\eta = 0.0001\ M_j^{6.6 F_L^2} \tag{4.4c}$$

In Regime IV:

$$\eta = 0.0001\ \frac{M_j^2}{2} \sqrt{2}^{6.6 F_L^2} \tag{4.4d}$$

In Regime V:

$$\eta = 0.0001\ \frac{M_j^2}{2} \sqrt{2}^{6.6 F_L^2} \tag{4.4e}$$

Where Ma is the Mach number for unchoked flow

$$Ma = \frac{V_{\max}}{c} \tag{4.5}$$

and Mj is the freely expanded jet Mach number for choked flow

$$M_j = \sqrt{\left(\frac{2}{\gamma - 1} \right) \left[\left(\frac{P_{inlet}}{\alpha P_{exit}} \right)^{\left(\frac{\gamma - 1}{\gamma} \right)} - 1 \right]} \qquad \text{(Regimes 2-4)}$$

(4.6a,b)

$$M_j = \sqrt{\left(\frac{2}{\gamma - 1} \right) \left[(22)^{\left(\frac{\gamma - 1}{\gamma} \right)} - 1 \right]} \qquad \text{(Regime 5)}$$

4.3 Peak frequency

The control valve aerodynamic noise prediction model also predicts a "haystack"-like peak or maximum in the measured downstream internal sound pressure spectra, which rolls off exponentially on both sides. The formulas for the peak frequency inside a tube are:

$$f_p = \frac{0.2 * V_{vc}}{D_j} \qquad \text{(Regime I)} \qquad (4.7a)$$

$$f_p = \frac{0.2 * M_j * c}{D_j} \qquad \text{(Regime II)} \qquad (4.7b)$$

$$f_p = \frac{0.35 * c'}{1.25 D_j \sqrt{M_j^2 - 1}} \qquad \text{(Regimes III-V)} \qquad (4.7c)$$

where c is the speed of sound at the vena contracta, D_j is the jet diameter, and M_j is the jet Mach number (Equation (4.6a,b)). The jet diameter is a function of the valve flow coefficient C_v and pressure recovery factor F_L and is presumably smaller than the exit section of the valve. As seen in Equation (4.7a-c), the smaller the effective diameter of the valve exit, the higher the peak frequency.

Chapter 5

Test Matrix and Experimental Procedure

5.1 Expansion devices tested

Figure 5.1 shows photographs of the expansion devices tested. Four different types of expansion devices were tested: orifice tubes, capillary tubes, thermostatic expansion valves, and an electronic expansion valve. A detailed illustration of the type of orifice tube tested is given in Figure 5.2. A detailed illustration of a thermostatic expansion valve (TXV) is given in Figure 5.3.

Orifice tubes of different diameters and lengths were tested with and without outlet screens, capillary tubes were tested of different diameters, materials and lengths, with and without outlet cones (see Chapter 6 and Appendix A), and thermostatic expansion valves of different capacities were tested. A detailed test matrix of expansion devices tested and the range of operating conditions is given in Table 5.1.

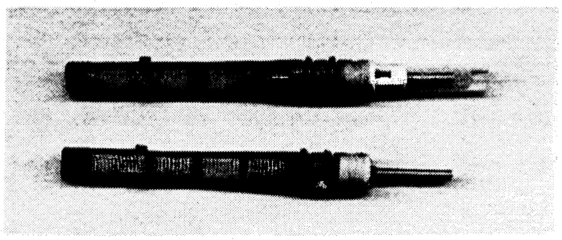

Orifice Tube

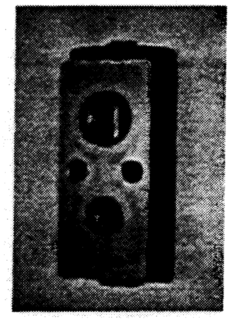

Thermostatic expansion valve

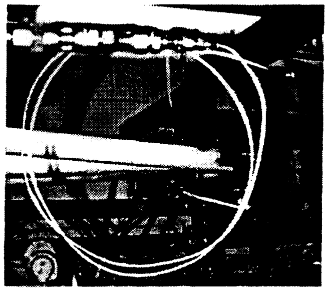

Capillary Tube

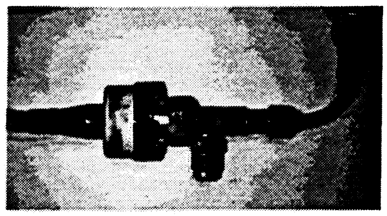

Electronic expansion valve

Figure 5.1 - Types of expansion devices tested

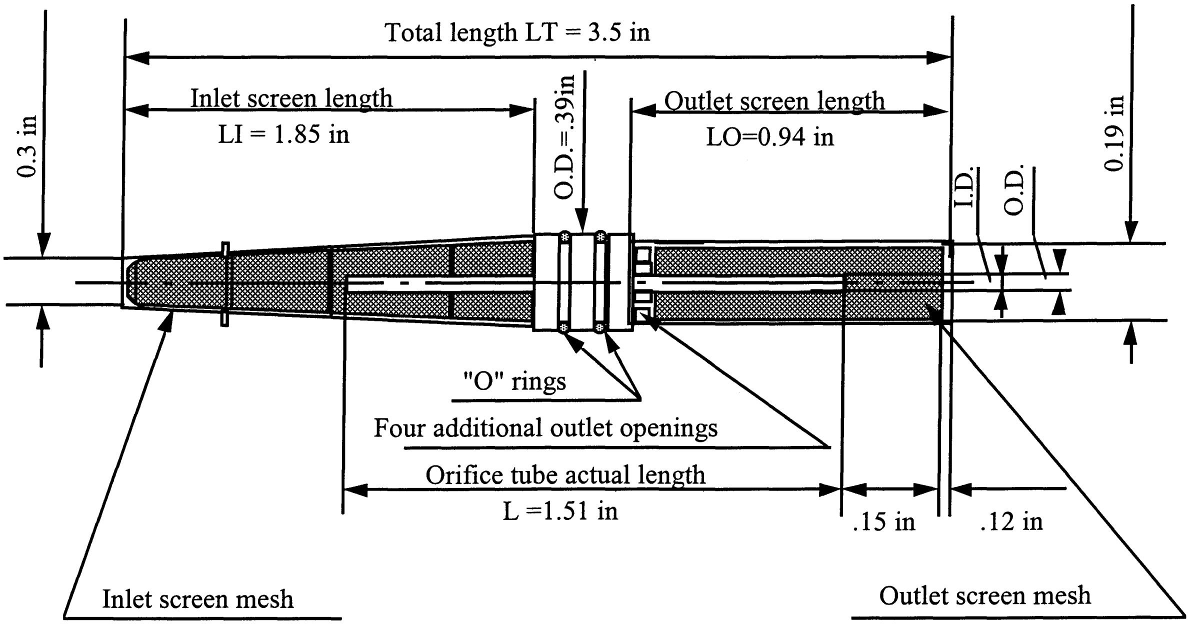

Figure 5.2 – Detailed illustration of tested orifice tubes

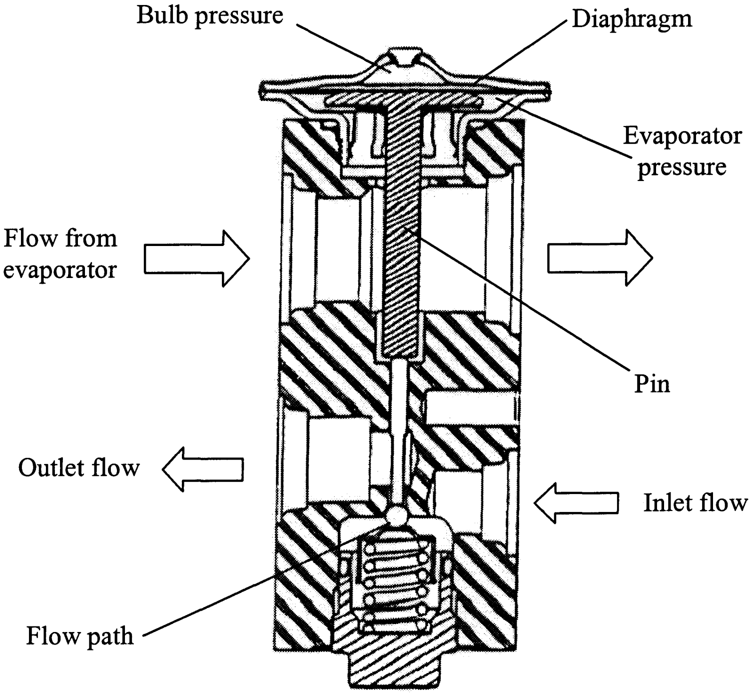

Figure 5.3 – Detailed illustration of TXV (from [34])

Table 5.1 - Experimental test matrix

I - Inlet, O - Outlet, OT - Orifice tube, CT - Capillary tube, CT* - Capillary tube with outlet cone (See Chapter 6 and Appendix A)

	Nominal Diameter	Length		Inlet Pressure [bars]	Outlet Pressure [bars]	Inlet Quality [-]	Outlet Quality [-]	Inlet Superheat [C]	Oulet Superheat [C]	Mass flow rate [lbm/hr]	TSPL re 20E-6 Pa [dB]
			Screens								
	1.22 mm	38.4 mm	I/O	8-29	3-6	0-1	0.1-1	(-)4.-41	0-70	75,100	126-146
OT	1.22 mm	38.4 mm	I only	7-31	3-9	0-1	0.2-1	(-)3-65	0-95	27-101	129-163
OT	1.45 mm	38.4 mm	I/O	9-24	4-9	1	1	5-76	18-92	35-110	144-157
OT	1.45 mm	38.4 mm	I only	9-20	5-6	1	1	9-84	30-108	35-97	147-165
OT	1.71 mm	38.4 mm	I/O	10-17	5-6	1	1	13-64	33-87	54-110	143-148
OT	1.71 mm	38.4 mm	I only	11-18	4-6	1	1	9-67	19-86	64-118	157-165
OT	1.71 mm	~13 mm	None	5-21	5-7	1	1	0-80	13-95	52-144	146-166
			Material								
CT	1.626 mm	127 in	Cu	7-30	4-7	0-1	0-1	(-)70-38	0-56	49-197	132-153
CT	1.626 mm	64 in	Cu	8-29	4-8	0-1	0.1-1	(-)13-33	0-57	75,100	115-147
CT	1.626 mm	32 in	Cu	10-31	4-5	0-1	0.3-1	0-23	0-51	75,100	134-162
CT	1.91 mm	75 in	Al	9-30	4	0-1	0.2-1	0-24	0-53	75,100	136-161
			Cone angle								
CT*	1.626 mm	32 in	5	13-26	4-5	0.1-1	0.3-1	0-20	0-50	75	129-155
CT*	1.626 mm	32 in	10	11-26	4-5	0-1	0.3-1	0-36	0-69	75	136-155
	No.		*Capacity*								
TXV	1		Smaller	8-23	4-8	0.9-1	1	0-60	2-79	41-129	146-158
TXV	2		Larger	8-18	4-8	0.3-1	0.6-1	0-37	0-43	75-363	149-159
EEV	3		Larger	6-12	4	0.2-1	0.2-1	0	0-6	100	139-152

5.2 Experimental procedure

All measurements were made using the experimental test facility as described in Chapter 2. All data points were taken at steady state using pure R134a and 0.5in O.D. tubing throughout the test section. For each data point, a measurement was made of the internal sound pressure (in psi) at microphone 1, the transfer function between microphones 1 and 2, and the coherence between microphones 1 and 2. For some data points, a measurement was also made of external pipe wall acceleration (in g's). All signal measurements were made with a frequency span of 0-20kHz, a resolution of 25Hz, and a Hanning window. All signal measurements were made with 50 averages and all monitored system variables were recorded at the start of a measurement.

For all data points, microphone 1 was located 1m. from the exit of the expansion device and the accelerometer was located 25in from the exit of the expansion device (unless otherwise noted). The microphones and accelerometer are sufficiently downstream of the expansion device (> 15 tube diameters) to ensure that all measurements are taken in the far-field of the generated noise.

For every data point, the sight glasses at the inlet and exit of the test section are monitored to ensure that the refrigerant phase (single or two-phase) is as displayed on the monitor screen. The manometers at the inlet and outlet of the test section were also monitored for agreement with the pressure transducer measurements displayed on the monitor screen. Coherence measurements were monitored during vapor flow to check for any disturbances to the flow below the first cut-off frequency.

The formula used to compute total internal sound pressure level (TSPL) for each data point is:

$$\text{TSPL (dB)} = 10Log_{10}\left(\frac{\sum_{20Hz}^{20kHz} (Sound\_pressure)^2}{(reference\_pressure)^2} \right) \quad (5.1)$$

where the sound pressure is the measured sound pressure at each frequency and the reference pressure used is the standard reference pressure [9] of 20E-6 Pa.

For all data points, the microphones are assumed to be perfectly calibrated (see Appendix F) and the measured sound pressures are assumed free from reflections at all frequencies (see Appendix C).

5.3 Method of keeping TXV fully open

The thermostatic expansion valves were tested with their orificial elements fully open. The assembly to keep the TXV fully open is illustrated in Figure 5.4. The top cavity of the bulb is pierced with a small copper tube which is brazed leak-tight to the bulb. The cavity is pressurized with Nitrogen which pushes the diaphragm down. Subsequently, the diaphragm pushes the pin down which pushes the valve opening fully open (See Figure 5.3). Th pressure in the lower bulb cavity is normally the evaporator outlet pressure. Since the top passage of the valve is blocked during testing of the valves in the experimental test facility (See Figure A.2), the lower bulb cavity pressure is unknown. The Nitrogen pressure necessary to keep the valve fully open is determined by increasing the pressure while the valve is operating in the test facility until further increases in pressure no longer affects the flow through the valve. This Nitrogen pressure may change slightly in response to the refrigerant conditions through the valve, but is normally around 200 psig as given by the pressure regulator.

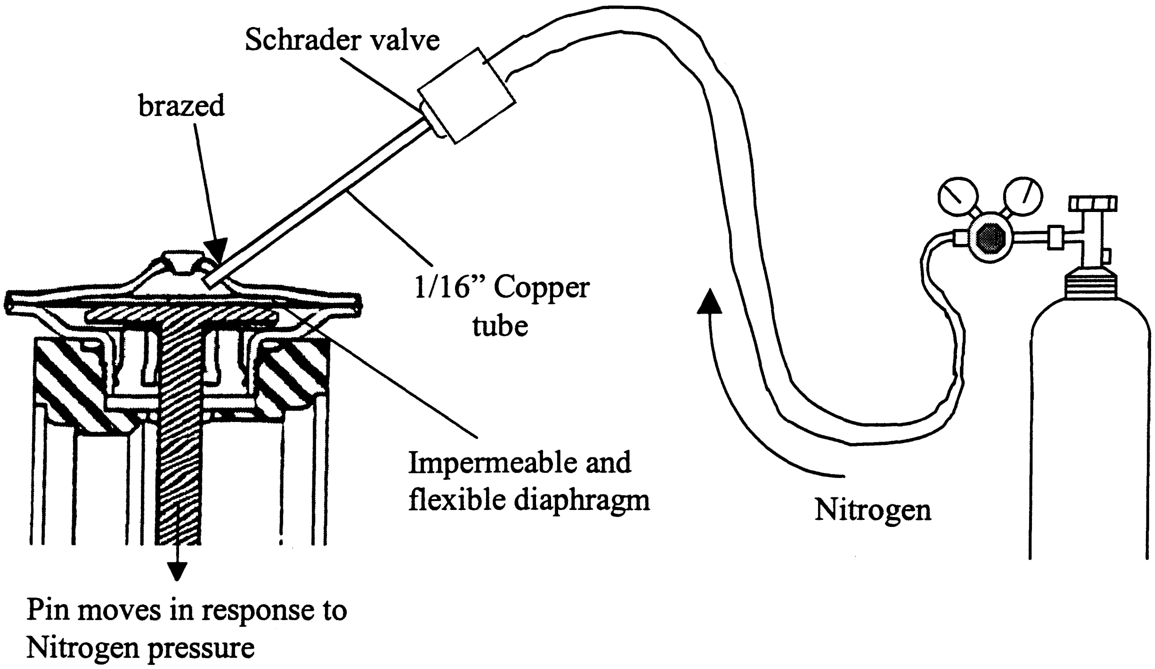

Figure 5.4 - Assembly to keep TXV fully open

Chapter 6

Experimental Results

6.1 Control valve aerodynamic noise model predictions

Model predictions for one orifice tube in vapor flow are shown in Figure 6.1. Note the excellent agreement between model predictions and experimental results. These predictions were made by following the model exactly, with F_L=1 (physically true for an orifice tube in vapor flow) and by calculating the experimental total internal sound pressure level by Equation (3.1). Thus it appears that the model is very well suited for predicting noise from orifice tubes with pure refrigerant vapor flow. Our original orifice tube vapor data is plotted versus model predictions in Figure 6.2. Note that all of the orifice tube vapor data agrees within +/- 5dB (+/- 3.5%).

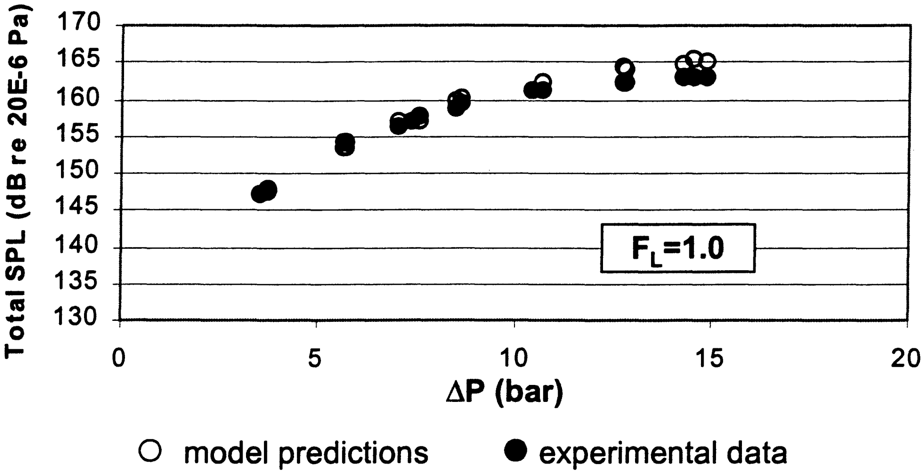

Figure 6.1 – Experimental noise data and model predictions for one orifice tube in vapor flow

Orifice tube: 1.45mm I.D., 38.4mm length, no downstream screen
Outlet pressure: 5.5 bar

Some capillary tube vapor data is also plotted in Figure 6.2. Note that the long capillary tube data (L=64in, 127in) is predicted much less well by the model than the orifice tube data. One possible explanation is related to the fact that the model assumes isentropic flow. Both orifice tubes and capillary tubes dissipate energy by friction along the length of the tube. Thus, the model's isentropic flow assumption would predict a higher-than-actual exit pressure for each data point. However, as described in Chapter 1, a larger percentage of a given pressure drop in capillary tubes is frictional pressure drop as compared to orifice tubes. As such, the isentropic exit pressures should be closer to the actual exit pressures in orifice tubes than in capillary tubes. This is the case for the data of Figure 6.2, as shown in Table 6.1. The capillary tubes are also shown to be less isentropic than the orifice tubes, as expected, since friction is an irreversibility related to pressure drop by the Maxwell relation *ds* = *-(v/T)dP* [25]. These calculations assume choked Fanno flow of an idea gas and the *EES* code used is given in Appendix L.

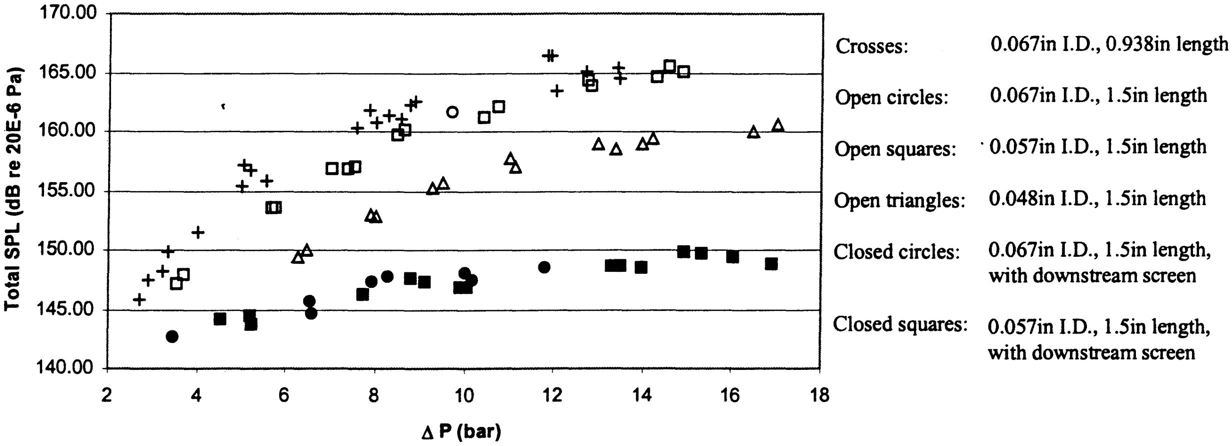

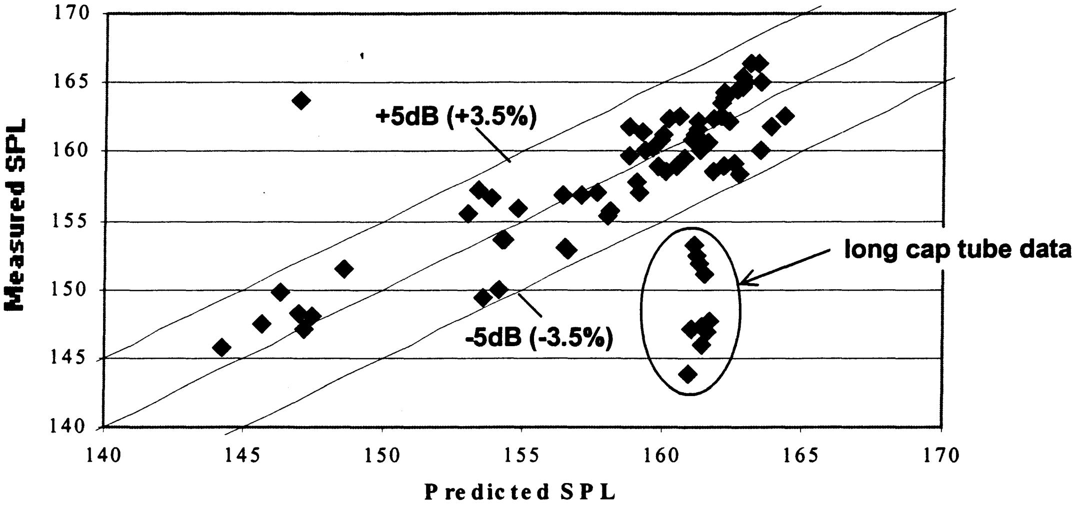

Figure 6.2 – Orifice tube and some capillary tube vapor flow data vs. model predictions with F_L=1.

As described in Chapter 1, as the pressure ratio across a choked expansion device increases, the exit flow changes from over-expanded, where recompression exists (Pexit<Poutlet), to under-expanded (Pexit>Poutlet). As seen in Chapter 4, as the pressure ratio across a valve increases, through the point where recompression ends, the acoustic efficiency factor increases, as well. This implies that for a given pressure difference, a device with recompression would be the quietest. All of the capillary tube data in Figure 6.2 is predicted by the model to be beyond the point of recompression (i.e. under expanded). However, in reality, all of the data are in fact over expanded. This fact may be related to the over prediction of the capillary tube points by the model. Thus for identical operating conditions, one would expect capillary tubes to be quieter than orifice tubes, at least when vapor flow is present.

Another possibility for the model over predictions of the capillary tube data is that since more entropy generation in a process represents more lost work, or dissipated energy, less energy may be available for sound at the exit from a capillary tube than would be predicted by the isentropic model. However, as seen in Table 6.1, the stream power at the exit of the capillary tube is virtually the same, whether or not isentropic flow is assumed, and makes a negligible difference in predicted noise.

Table 6.1 – Difference between isentropic and non-isentropic exit conditions for the data of Figure 6.2

Tube/ Length (in)	**No. points**	**Avg. |Predicted-measured TSPL| (dB)**	**Avg. entropy change along tube (%)**	**Avg. increase in exit pressure for isentropic flow (%)**	**Avg. absolute change in stream power for isentropic flow (%)**	**Avg. change in predicted TSPL for isentropic stream power (dB)**
		Standard deviation in ( )	*St. deviation in ( )*	*Standard deviation in ( )*	*Standard deviation in ( )*	
Orifice / 1.5	48	1.6 (0.7)	7.2 (3.1)	28.3 (6.3)	1.2 (3.7)	0.0
Capillary / 32	5	4.4 (0.4)	19.8 (3.7)	65.5 (1.3)	1.7 (0.5)	0.1
Capillary / 127	7	12.6 (2)	24.9 (3.9)	80.3 (1)	1.8 (0.4)	0.1

Model prediction results for the thermostatic expansion valves tested in vapor flow are shown in Figure 6.3. The agreement between model predictions and experimental results is again very good. However, F_L was not known for the valves tested a priori. The model was used to solve for F_L for one data point for each valve. That F_L was then assumed for each valve for the remainder of the model predictions.

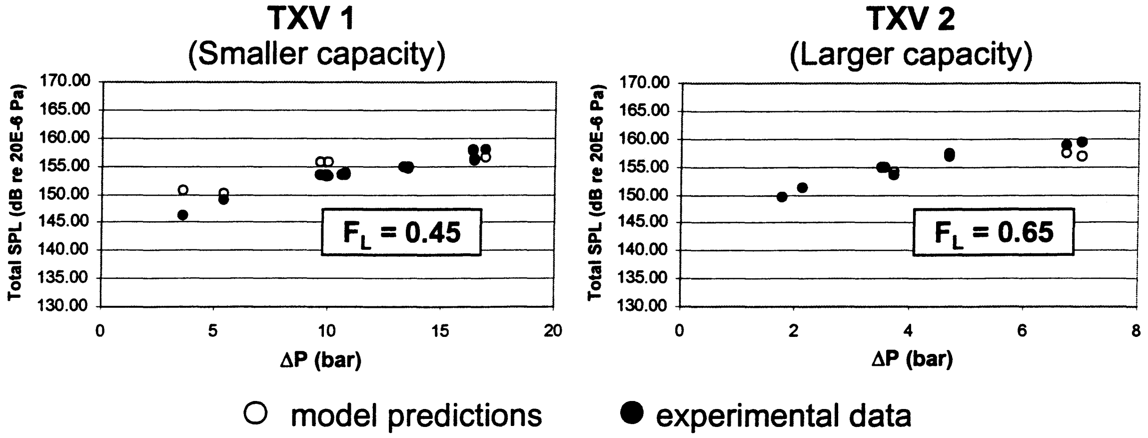

Figure 6.3 – Experimental noise data and model predictions for tested TXVs

6.2 Orifice tube results

A full set of results, including two-phase flow, for one orifice tube are shown in Figure 6.4. With mass flow rate and downstream pressure held approximately constant, the total internal sound pressure level downstream of the orifice tube increases with pressure difference across the tube, as long as the exit flow remains two-phase. Once the exit flow becomes pure superheated vapor, the TSPL seems to increase sharply and then level off, even as the inlet pressure is further increased. Thus the relationship between downstream noise and ΔP predicted by the valve noise model (as illustrated in Figure 4.2) for vapor flow seems to hold approximately for orifice tubes, even when two-phase flow is present.

The same data is also plotted as a function of exit conditions (quality or superheat) in Figure 6.5. As with inlet pressure, the total internal sound pressure level seems to increases (almost linearly) with exit quality, as long as the exit flow remains two-phase. The total internal sound pressure level then increases sharply and levels off as the outlet superheat is further increased. This makes sense in terms of the principles of the valve noise model. As the exit quality is increased and less liquid is present at the exit of the tube, the vena contracta (exit) velocity increases, so the stream power at the exit of the tube increases and more energy is then available for sound at the exit and downstream. Since ΔP is also increasing, the acoustic efficiency factor may also be increasing, further increasing the sound power downstream. Finally, the sharp jump in noise when vapor flow begins reflects the sharp increase in speed of sound between two-phase and pure vapor flow in refrigerant. Since the vena contracta velocity is the speed of sound for choked flow, the stream power at the tube exit, and hence the available energy for sound, increases sharply as the flow becomes single-phase.

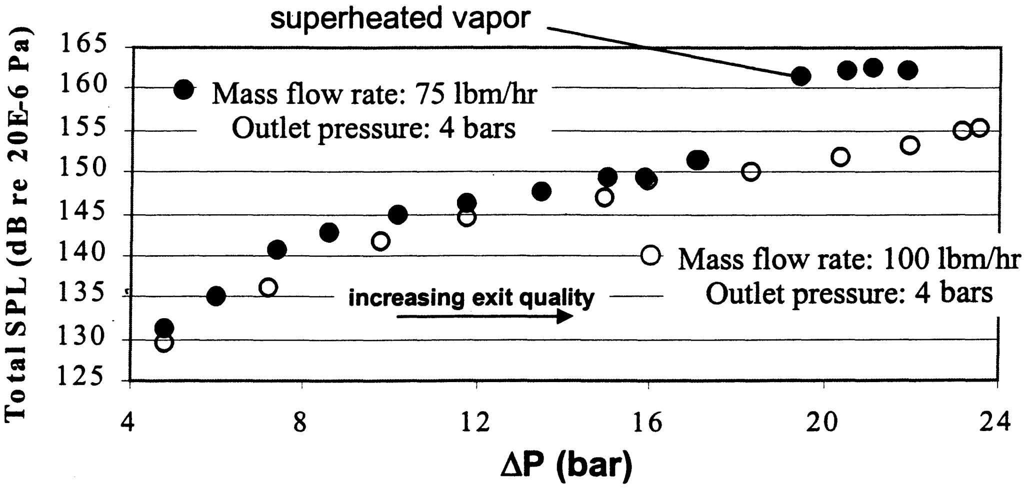

Figure 6.4 – Full set of results for one orifice tube: TSPL vs. ΔP
Orifice tube: 1.22mm I.D., 38.4mm length, no downstream screen

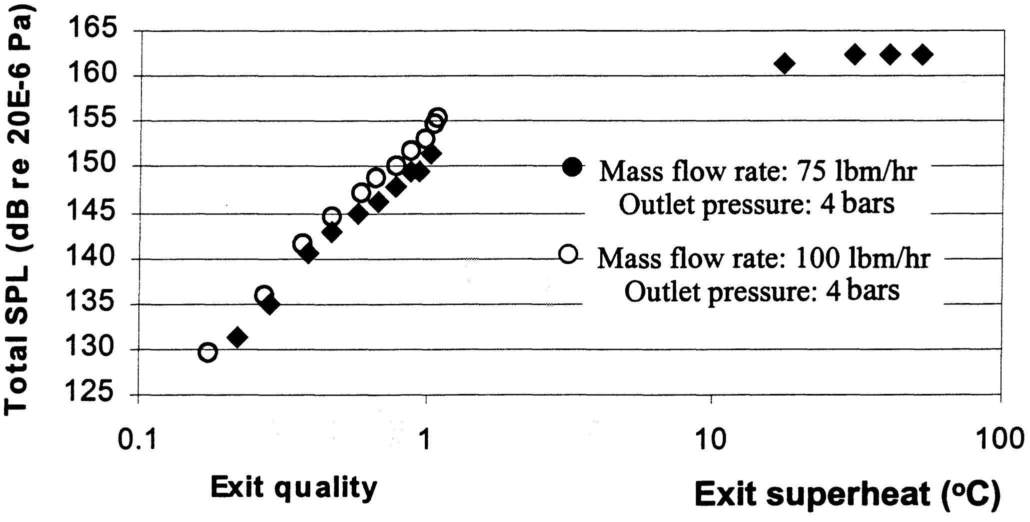

Figure 6.5 - Full set of results for one orifice tube: TSPL vs. Exit conditions
Orifice tube: 1.22mm I.D., 38.4mm length, no downstream screen

Note from the figures that for a given ΔP or exit condition, increasing the mass flow rate seems to slightly increase the noise. This also makes sense in terms of the principles of the valve noise model, as increasing the mass flow rate, all else being constant, will increase the stream power at the exit and hence increase the energy available for sound.

The internal sound pressure spectra over the audible frequency range for the 75lbm/hr case of Figure 6.4 and 6.5 are shown in Figure 6.6. The results show the nature of the internal sound pressure as the exit conditions change from a low-quality to a high-quality and eventually to a superheated vapor exit condition. As anticipated from preliminary results, the internal sound pressure for superheated vapor flow is basically white noise over the audible frequency range and significant, as compared to the instrument noise. As the exit quality decreases, the higher frequency sound waves are more sharply attenuated and the overall sound pressure decreases. Also, the very low frequency nature of the sound pressure spectra changes as the sharp and visible peak at around 400Hz in the vapor flow spectra disappears in the two-phase spectra. The internal sound pressure spectra for the 100lbm/hr case of Figure 6.6 are given in Appendix K.

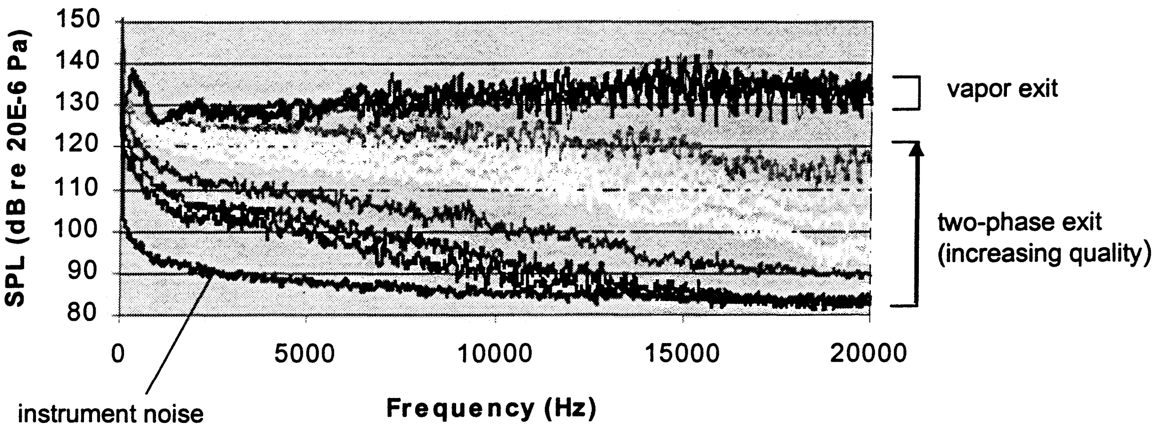

Figure 6.6 – Internal sound pressure spectra for 75lbm/hr case of Figures 6.4 & 6.5

The effect of downstream (outlet) pressure on expansion noise was investigated for one orifice tube. The results for one data set are shown in Figure 6.7. For the same mass flow rate, it appears that downstream pressure has little or no effect on the total internal sound pressure level when plotted against pressure difference or exit conditions. Since the orifice tube is assumed to be choked for all test conditions, downstream pressure should have little effect on mass flow rate. It was unclear before testing whether downstream pressure would have an effect on noise.

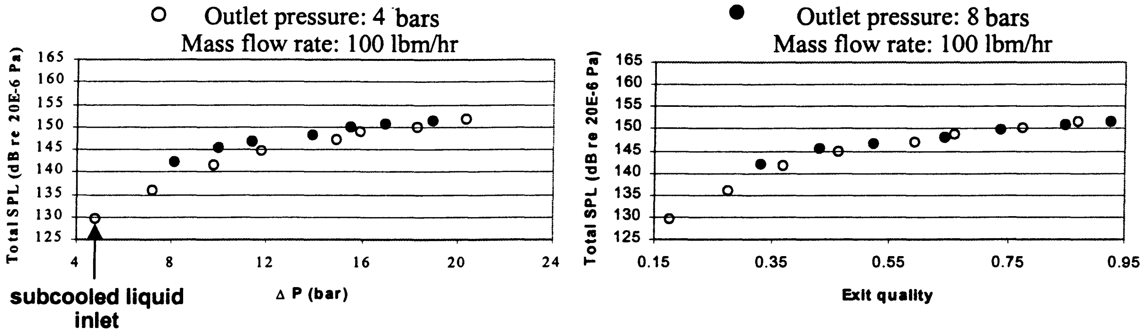

Figure 6.7 – Influence of downstream pressure on expansion noise from orifice tubes
Orifice tube: 1.22mm I.D., 38.4mm length, no downstream screen

These results also make sense in terms of the principles of the valve noise model. For a given orifice tube, the stream power at the tube exit and the sound power downstream are determined by the mass flow rate, pressure difference, and speed of sound at the exit of the tube. For a choked orifice tube, these variables are determined by the inlet conditions and are independent of the conditions downstream. And although downstream conditions do effect the total internal sound pressure level by Equation 4.3, for a given ΔP and exit quality/superheat, the exit speed of sound and density should only be moderately affected by pressure difference. The character of the noise appears unchanged by downstream pressure, as well. The internal sound pressure spectra are given in Appendix K.

Downstream (outlet) screens (screens attached to the outlet of the orifice tube) appear to have a significant effect on expansion noise, as shown in Figure 6.8. For the same orifice tube, mass flow rate, and operating conditions, the outlet screens decrease the total internal sound pressure by 15-20dB at most conditions. As shown in Figure 6.9, the character of the internal pressure spectra for the orifice tubes with screens is different, wavier and without the peak around 400Hz, than for the orifice tubes without screens (see Figure 6.6).

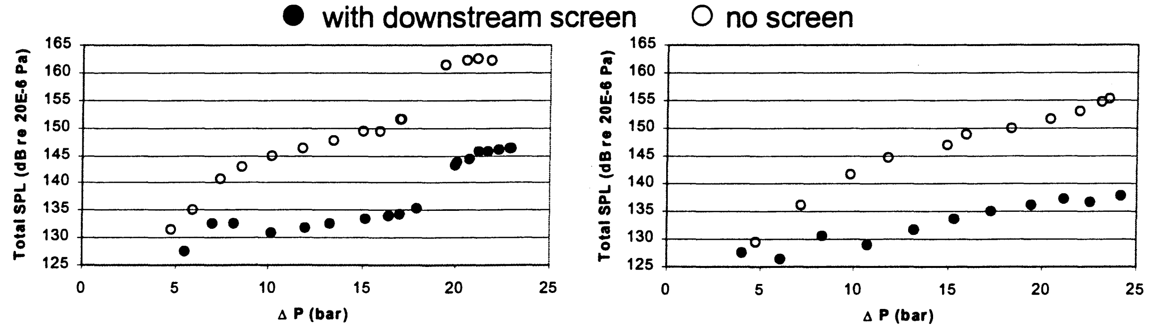

Mass flow rate: 75lbm/hr

Mass flow rate: 100lbm/hr

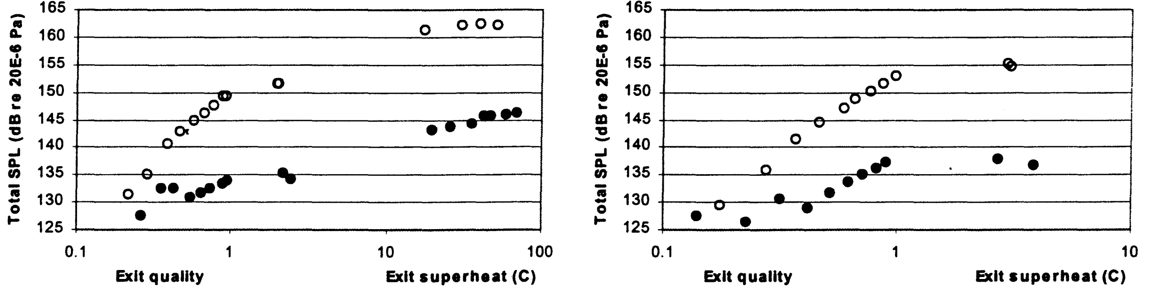

Figure 6.8 – Influence of downstream screens on expansion noise from orifice tubes

Orifice tube: 1.22mm I.D., 38.4mm length
Outlet pressure: 4 bars

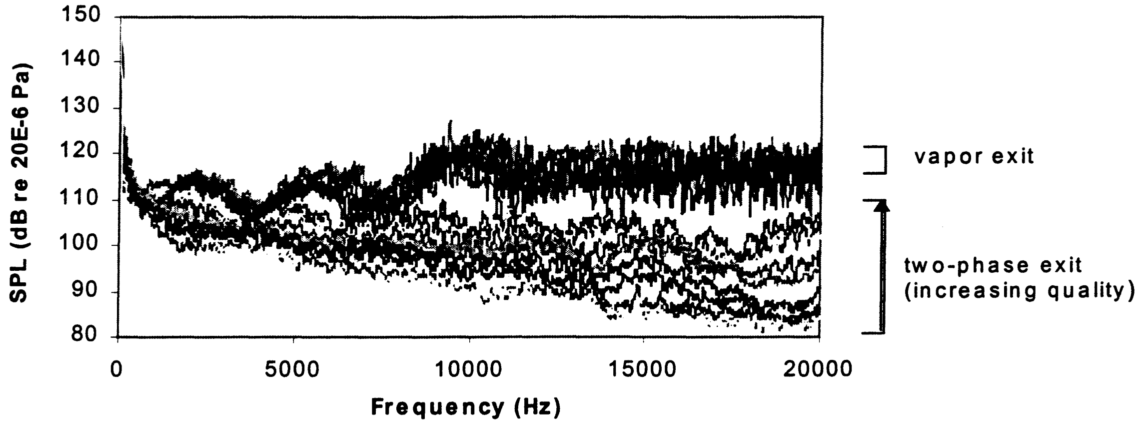

Figure 6.9 – Internal sound pressure spectra for the 75lbm/hr case of Figure 6.8

Orifice tube: 1.22mm I.D., 38.4mm length
Mass flow rate: 75lbm/hr Outlet pressure: 4 bars
(Spectra for 100lbm/hr case given in Appendix K)

6.3 Orifice tube vs. capillary tube

An experiment was performed which directly compared two different capillary tubes to the above orifice tube results. The three expansion devices were each of a different diameter. The length of each capillary tube was chosen to give nearly the same mass flow rate and outlet conditions as the orifice tube for each set of inlet conditions over a range of inlet conditions. An illustration of this given in Figure 6.10 along with the data plotted on a p-h diagram. Results for some of the data sets are also given in Figure 6.10.

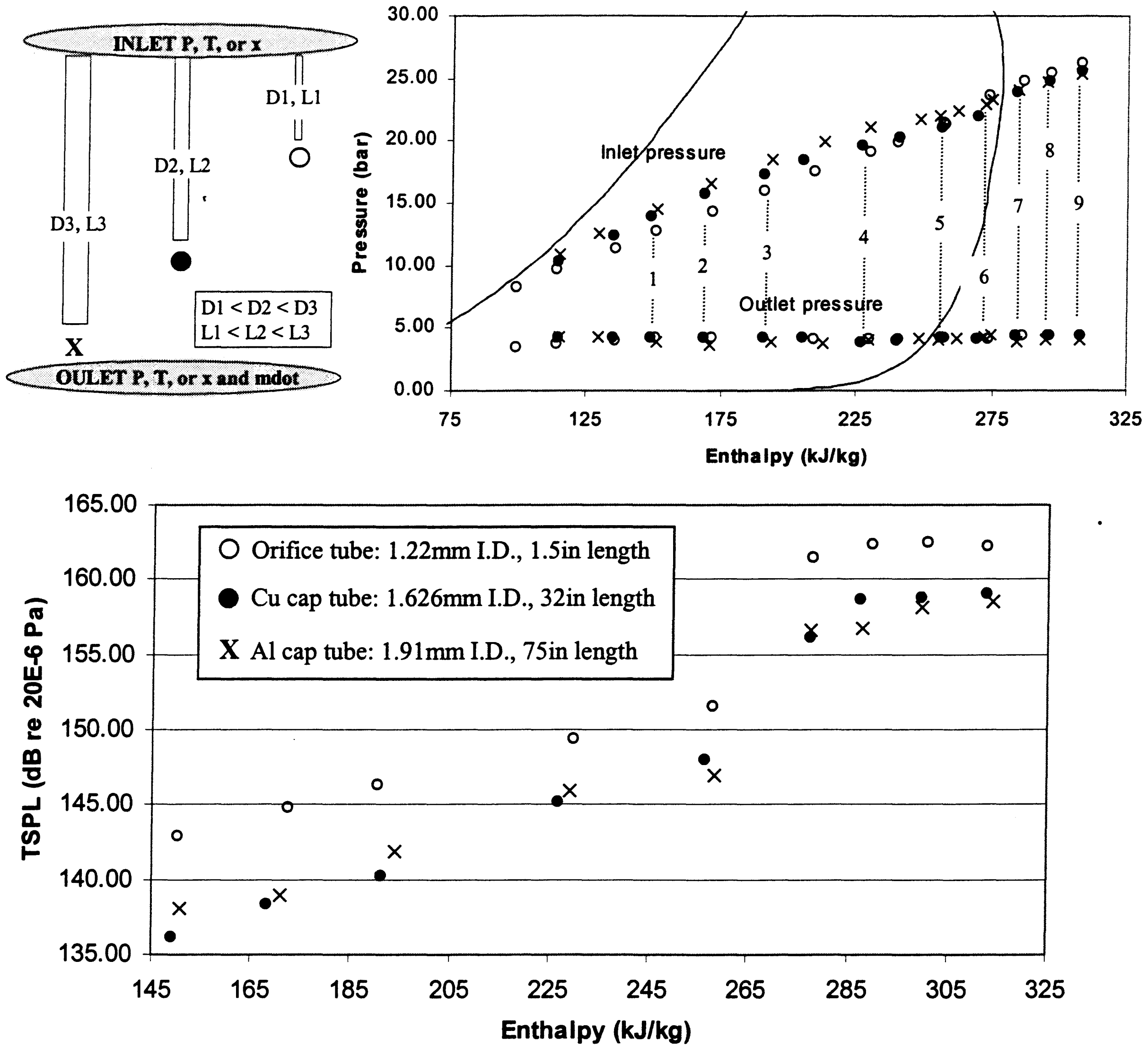

Figure 6.10 - Experimental data for two capillary tubes and an orifice tube at 75lbm/hr. The bottom plot shows data sets 1-9 marked on p-h diagram

This figure shows that for identical conditions upstream and downstream of the expansion device, a capillary tube has a lower total sound pressure level than an orifice tube. As described above, this is may be related to the increased frictional pressure drop along the length of a capillary tube as compared to an orifice tube. The relative pressure drops are plotted in Figure 6.11. The results of the all the data sets vs. ΔP are also given in Figure 6.11.

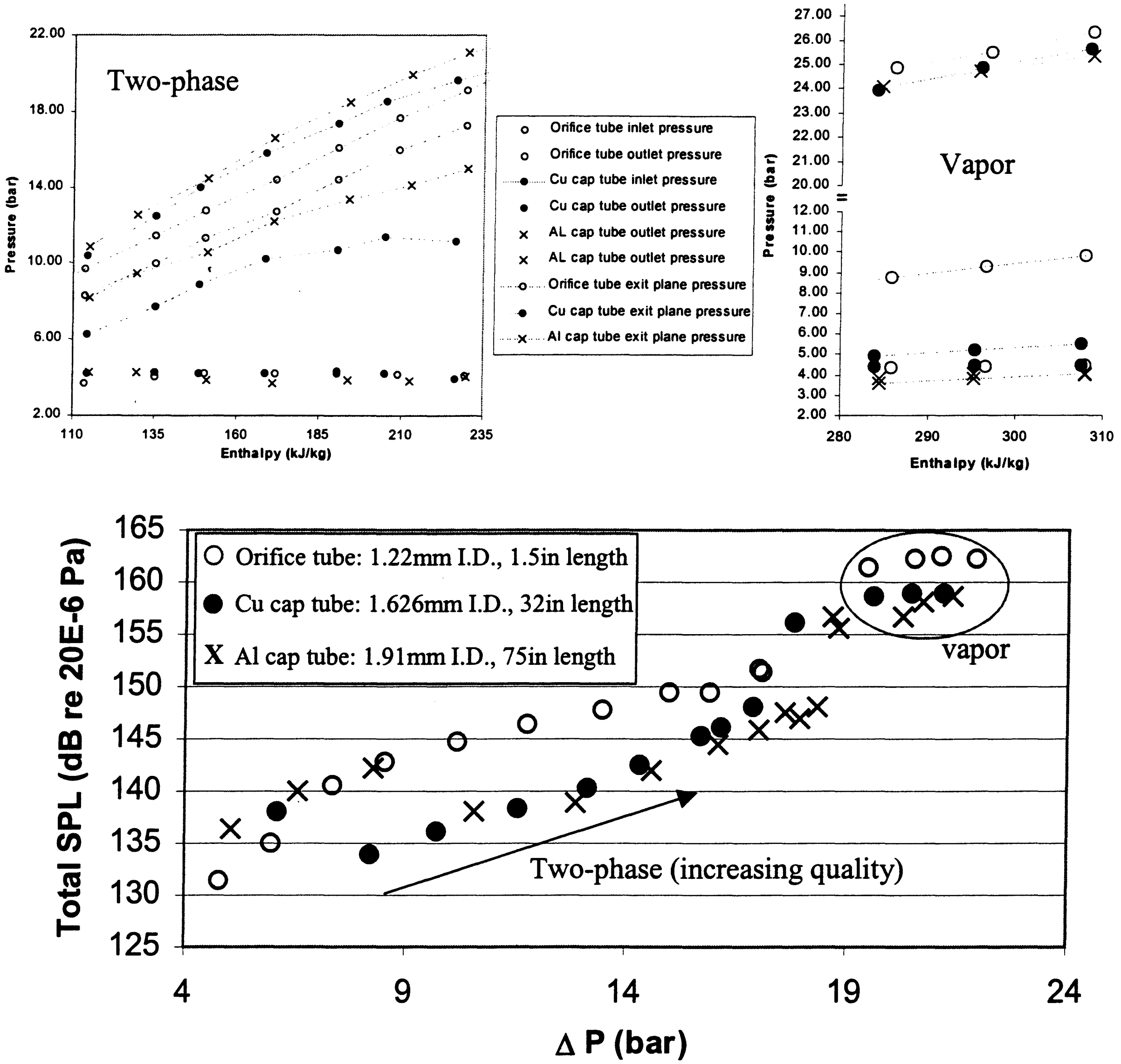

Figure 6.11 - Inlet, exit, and outlet pressures and noise measurement results for the data of Figure 6.10

Note that the capillary tube curves in the bottom plot of Figure 6.11 rise to intersect the orifice tube curve at low pressure differences. Given the same inlet and outlet conditions, the refrigerant quality must increase along the capillary tube length at a slower rate than along the shorter orifice tube length. Also, the frictional pressure drop in tubes is proportional to the velocity squared [3,5] and velocity must increase with quality for a given mass flow rate due to the decreasing density. Hence, for low pressure differences, when the quality is very low for much of the expansion, the frictional pressure drops along the two expansion devices may be similar. Since inlet and outlet contraction and expansion are related to diameter ratios [3,4] (which are similar for all three tubes), then for a given operating condition, at a low pressure difference, the two total sound pressure level curves intersect.

Additional results for the orifice tube vs. capillary tube experiments are included at the end of the Chapter and additional capillary tube results are included at the end of the Chapter and in Appendix K.

6.4 Orifice tube vs. expansion valves

For a given pressure difference or exit condition across the expansion device, the noise performance of thermostatic expansion valves and electronic expansion valves can be compared to orifice tubes, as well. The results for a TXV tested are shown in Figure 6.12 and the results for the EEV tested are shown in Figure 6.13.

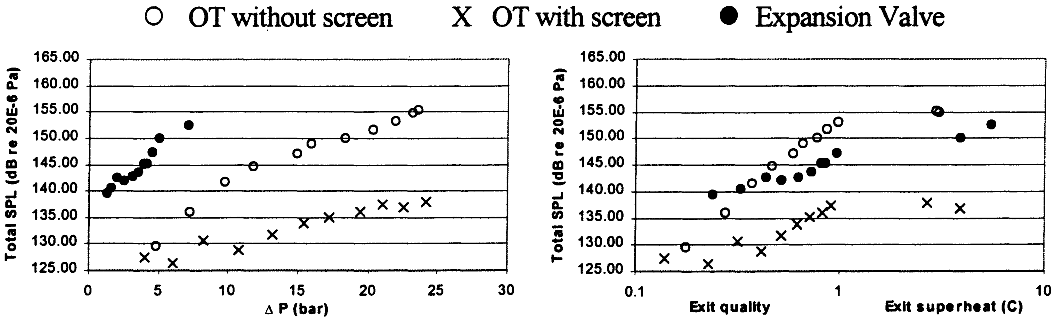

Figure 6.12 – TXV1 noise vs. orifice tube noise

Orifice tube: 1.22mm I.D., 38.4mm length

Mass flow rate: 75lbm/hr Outlet pressure: 4 bars

The results show a clear geometric dependence on expansion noise, as expected from the valve noise model. The model accounts for flow rating, pressure recovery, and exiting jet angle in its noise predictions, all factors based upon the geometry of the expansion device. These factors may significantly affect downstream noise, as indicated by the discussion of jet angle in Chapter 4.

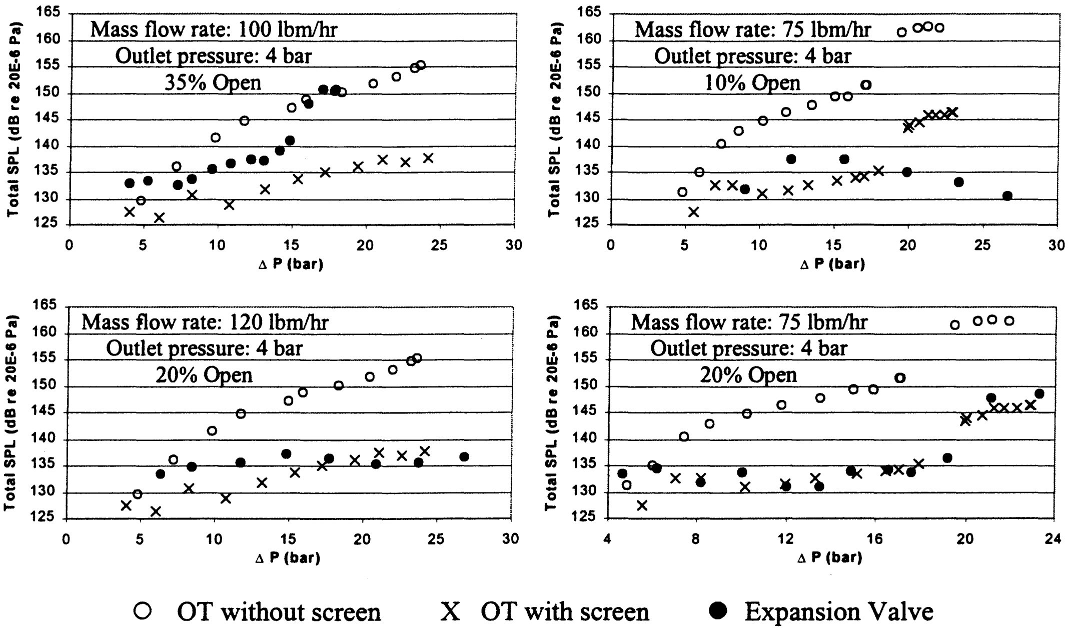

Figure 6.13 – EEV noise vs. orifice tube noise

Orifice tube: 1.22mm I.D., 38.4mm length

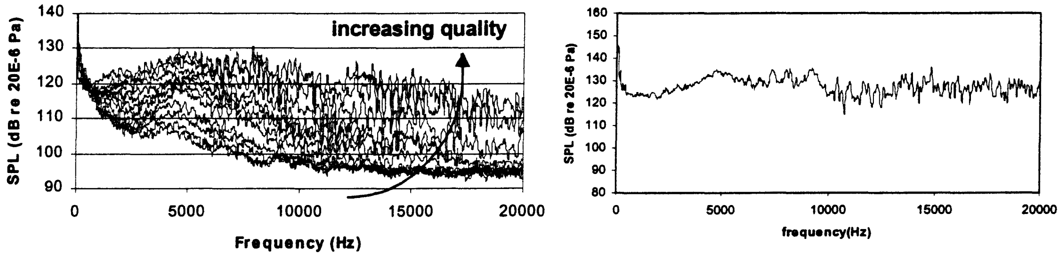

Figure 6.14 – TXV1 internal sound pressure spectrum

Mass flow rate: 75lbm/hr   Outlet pressure: 4 bars

Expansion device geometry may also affect the character of expansion noise. The internal sound pressure spectra for the TXV of Figure 6.12 is shown in Figure 6.14. The noise spectra are much "wavier" than orifice and capillary tube spectra and also without the peak around 400Hz, resembling the spectra of the orifice tube with downstream screens.

6.5 Coherence measurements

As discussed, coherence measurements were taken for every data point to monitor for disturbances to the measurement. Typical coherence measurements for one orifice tube are shown in Figure 6.15. Note that for pure vapor flow (x=1) the coherence between the two microphones is one for all frequencies below the first cutoff (approx. 7850 Hz), as expected. As the exit quality decreases a bit, the coherence becomes less than one at most frequencies. This may not seem a surprising result, as the presence of bubbles and inhomogeneous flow might lead to significantly different sound pressure readings at the two microphones. However, this "two-dip" shape of the coherence spectrum is exceptionally repeatable, appearing for every measurement of moderate quality for every expansion device tested, with the dips always occurring at roughly the same frequencies. The coherence measurements for all of the expansion devices tested can be found in Appendix K.

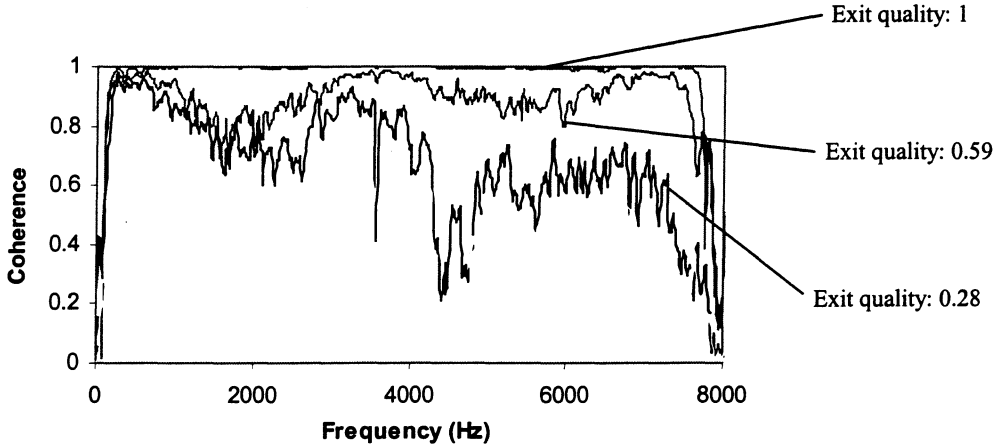

Figure 6. 15 – Orifice tube coherence measurements

Orifice tube: 1.22mm I.D., 38.4mm length
Mass flow rate: 75lbm/hr Outlet pressure: 4 bars

As the exit quality further decreases, the coherence continues to worsen at all frequencies. When the quality becomes low enough, the expansion noise approaches the noise level of the instrument (as shown in Figure 6.6) and the coherence between the microphones reflects the incoherent instrument noise.

6.6 Tube wall acceleration

An important step in understanding the transmission of internal sound pressure waves to the surrounding environment is investigating the vibration of the walls of the tube through which the sound is traveling. Downstream tube wall acceleration measurements have been made for many of the expansion devices tested at many of the tested operating conditions. Figure 6.16 shows some of the acceleration spectra for the one cap tube in vapor flow. All other acceleration measurements are included in Appendix K.

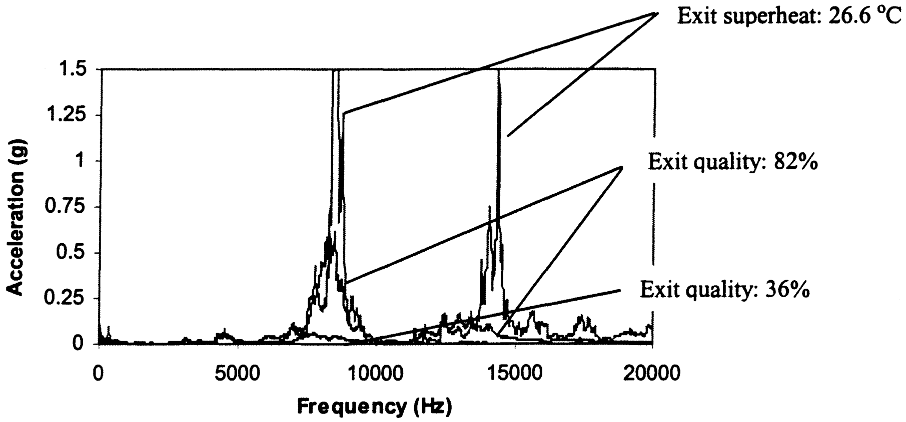

Figure 6.16 – External pipe-wall acceleration measurements for Al cap tube
Cap tube: 1.91mm I.D., 75in length
Mass flow rate: 75lbm/hr Outlet pressure: 4 bars

Two items are especially of note in Figure 6.16: The significant peaks in the acceleration spectra around 8kHz and 14kHz with a relatively flat spectra elsewhere; and the diminishing relative magnitude of those peaks as exit superheat/quality decrease. Recall the relatively smooth internal sound pressure spectra measured nearby and exciting the tube walls into vibration in vapor flow (see Figure 6.6). The tube wall seems to act as a band-pass filter in this case, preferentially transmitting only certain frequencies.

There exists in the literature a model for predicting tube wall acceleration given the corresponding internal sound pressure spectra and a damping factor, determined experimentally, for the given physical set-up of the test section [20, 26]. The tube wall acceleration model, much like the valve noise model, was originally developed for large industrial applications and ideal gas flow, and is comprised of fundamental theoretical equations and a single empirical factor. Also like the valve noise model, the tube wall acceleration model predicts our refrigerant vapor flow data very wall, once the damping factor has been determined.

6.7 Capillary tube outlet geometry

As discussed, geometry, both internal and outlet, can have a significant effect on expansion noise. The effect of outlet geometry was investigated for one capillary tube and the results are shown in Figure 6.17. As illustrated in the Figure, the outlet geometry was altered from a flat outlet section ("no-cone") to provide a smooth transition from the capillary tube inner diameter to the inner diameter of the downstream tubing. All previous capillary tube tests had the "no-cone" geometry (see Appendix A). Two different cone angles were tested.

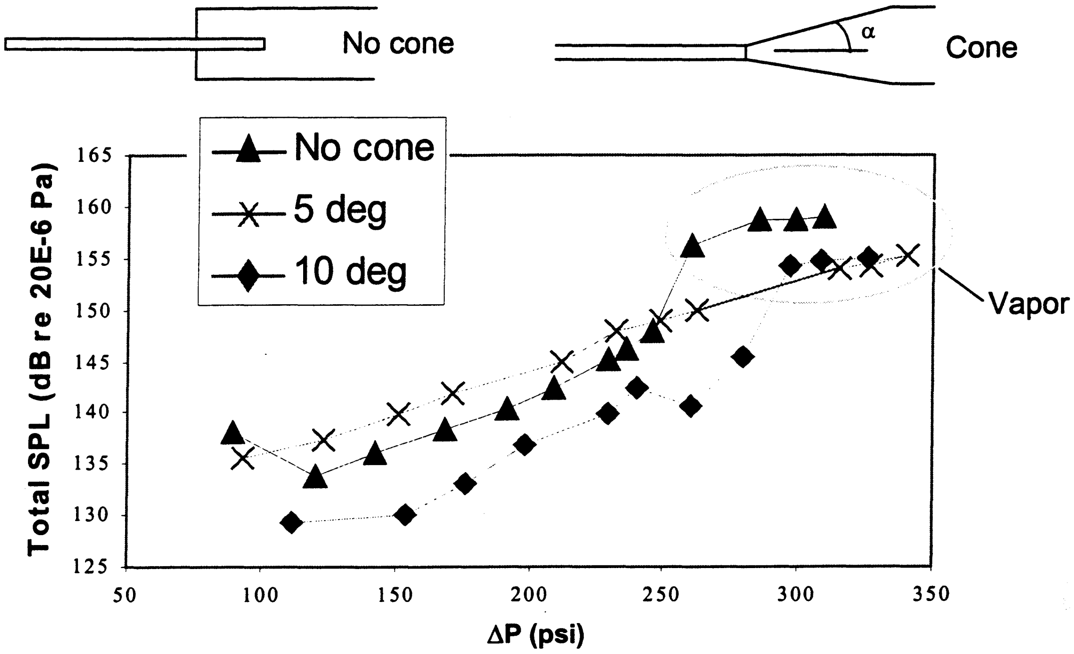

Figure 6.17 – Effect of outlet geometry on capillary tube noise

Capillary tube: 1.626mm I.D., 32in length
Mass flow rate: 75lbm/hr Outlet pressure: 4 bars

As seen in the Figure, the 10-deg cone seemed to uniformly attenuate the expansion noise for all operating conditions, much like outlet screens on an orifice tube (though much less severely). One might then expect the 5-deg cone to perform similarly. Surprisingly, the 5-deg cone actually increased the total internal sound pressure level for two-phase exit flow and flattened out the TSPL curve, demonstrating a much less significant jump in noise when vapor flow occurs.

The internal sound pressure spectra reflect this surprising behavior. As shown in Figure 6.18, for vapor flow conditions, the spectra are very close to each other at all frequencies and the sound is white noise. However, the peak at 400Hz is not present for the 10-deg cone spectrum and, in fact, a negative peak appears in the 5-deg cone spectrum. This might indicate that the cone may change 'the noise generation process to some degree.

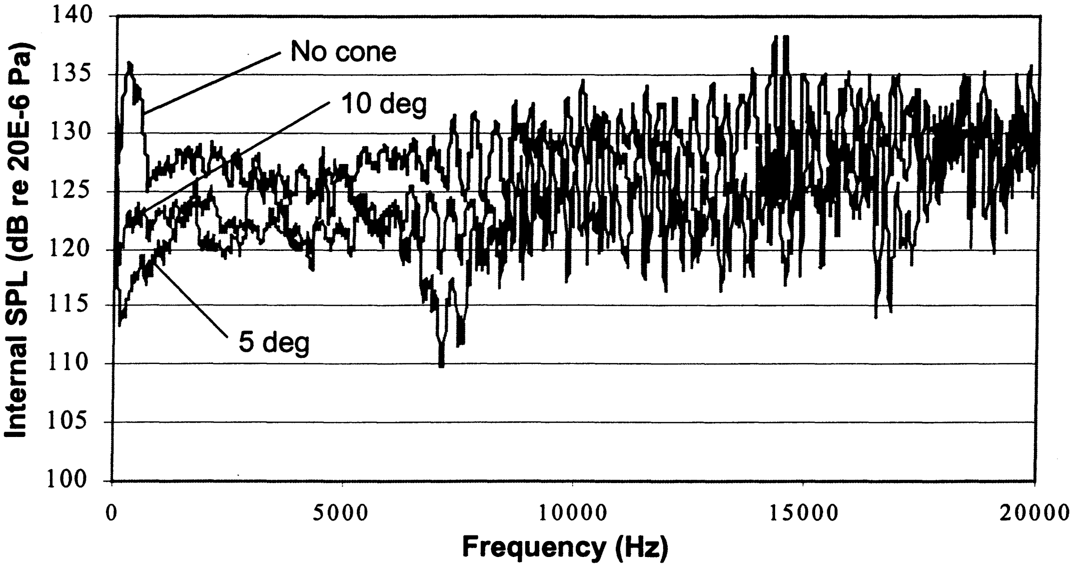

Figure 6.18 – Internal sound pressure spectra from capillary tube with outlet cones in vapor flow

Capillary tube: 1.626mm I.D., 32in length
Mass flow rate: 75lbm/hr Outlet pressure: 4 bars

For two-phase flow, the 5-deg cone spectrum is actually above the no-cone and 10-deg spectra over most of the audible frequency range, as shown in Figure 6.19. This result predicts the total sound pressure data of Figure 6.17 and may also indicate some change in the noise generation process caused by the presence of the cone. The acceleration spectra for vapor flow are shown in Figure 6.20

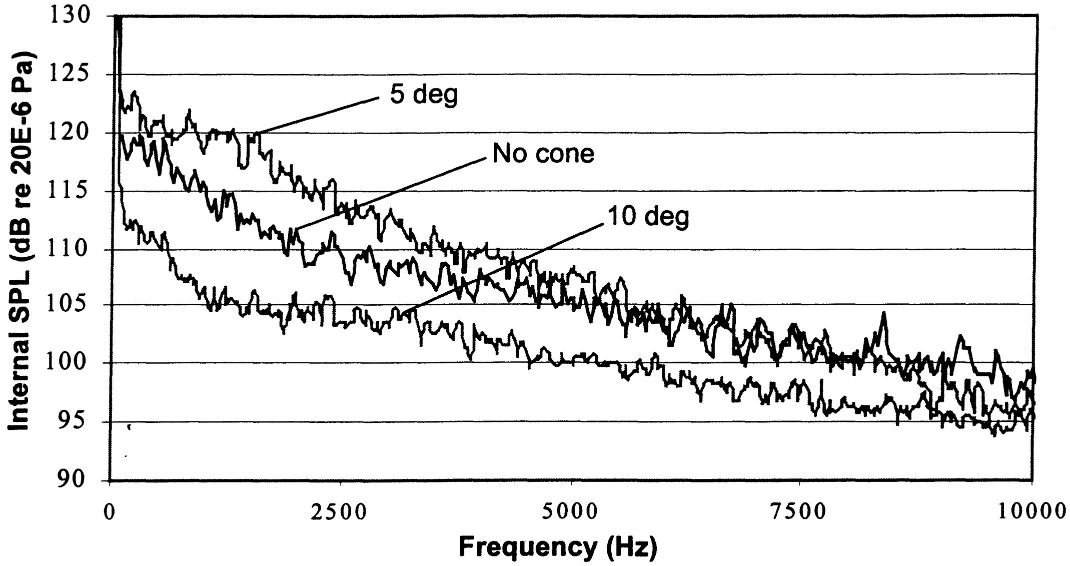

Figure 6.19 – Internal sound pressure spectra from capillary tube with outlet cones in two-phase flow

Capillary tube: 1.626mm I.D., 32in length
Mass flow rate: 75lbm/hr Outlet pressure: 4 bars

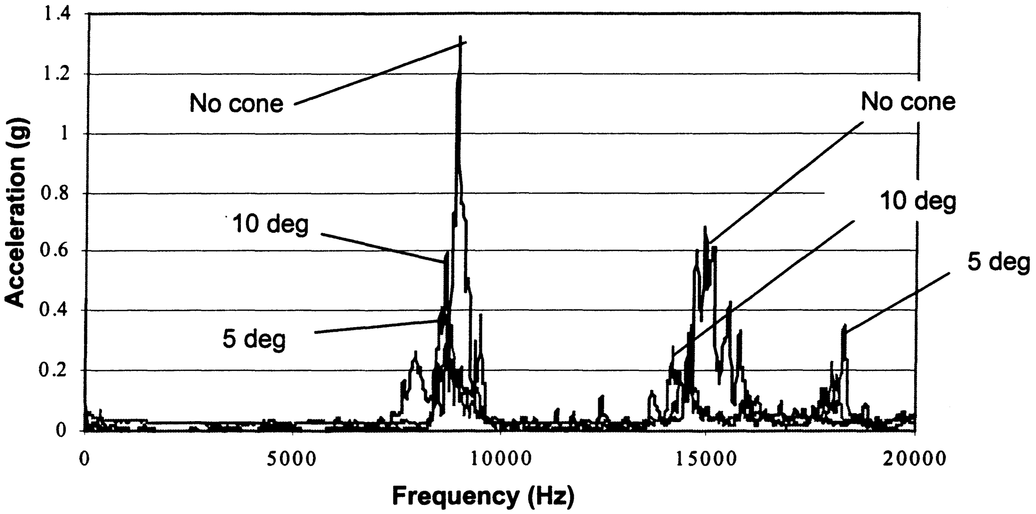

Figure 6.20 – Acceleration spectra from capillary tube with outlet cones in vapor flow

Capillary tube: 1.626mm I.D., 32in length
Mass flow rate: 75lbm/hr Outlet pressure: 4 bars

6.8 Peak frequency

As discussed in Chapter 4, the control valve aerodynamic noise prediction model [20] also predicts the shape of the downstream internal sound pressure spectrum for gas flow through the expansion device. The model predicts a "haystack"-like peak in the spectrum. A discussion of this as it applies to our data follows.

Below is the internal sound pressure spectrum for a capillary tube data point, taken from 0-100kHz. There is superheated R134a vapor flow throughout the tube. Note there is a peak frequency at about 16 or 17 kHz.

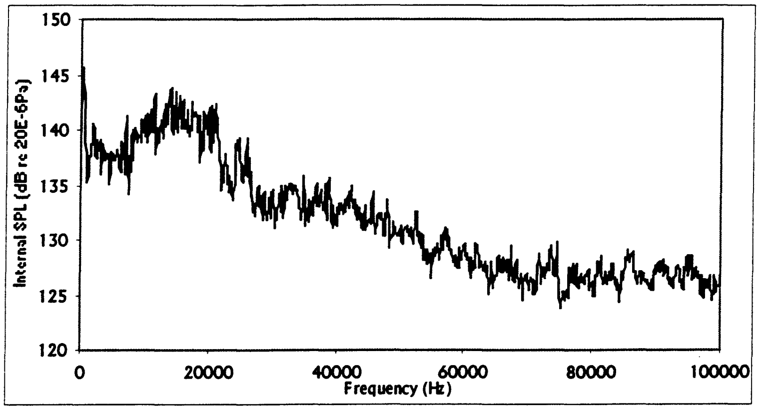

Figure 6.21 – Capillary tube vapor flow spectra from 0-100kHz

Capillary tube: 1.626mm I.D., 32in length

Inlet pressure: 30.2 bars	Outlet pressure: 4.4 bars
Inlet superheat: 6.2 C	Outlet superheat: 27.4 C

Mass flow rate: 99.5 lbm/hr

The valve noise model gives the formula for the shock-associated peak frequency inside a tube as

$$f_p = \frac{0.35 * c}{1.25 D_j \sqrt{M_j^2 - 1}} \qquad (4.7c)$$

where c is the speed of sound at the exit of the cap tube, D_j is the jet diameter, and M_j is the jet Mach number.

Although the pressure and temperature at the exit plane of the cap tube are not measured directly, c for R134a vapor is relatively constant in the temperature and pressure ranges of interest (approx. 168 m/s – see Appendix D).

The jet diameter is a function of the valve "flow coefficient", which is unknown presently for our capillary tube. However, a reasonable first guess would be the actual exit diameter of the cap tube, 0.001626m. Also, the model predicts the jet Mach number to be about 2 for these operating conditions. Although this is based on isentropic flow relations, this capillary tube is relatively short, so irreversibilities due to friction along the length of the tube may be small, as seen in Table 6.1. As such, a rough estimate of the peak frequency would be:

0.35168/(1.250.001626sqrt(4-1)) = 16.7kHz

Recall that the internal sound pressure spectra for orifice and capillary tubes in vapor flow is relatively flat over the audible frequency range, 0-20kHz. Why is this peak then normally not seen when we examine the data? Well, below is the same plot as above, plotted 0-20kHz:

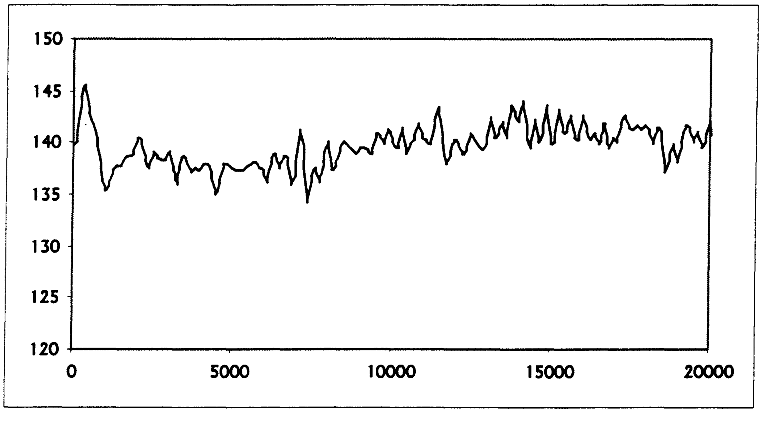

Figure 6.21 – Spectra of Figure 6.21 plotted 0-20kHz

It seems the spectra in this range are still *in* the peak, so we cannot normally *see* the peak in our data. These results lend further optimism to the use of the valve noise model to the prediction of noise from expansion devices in refrigeration systems.

6.9 EEV Coherence and acceleration spectra

Finally, the EEV coherence and acceleration spectra, although behaving in general as discussed in sections 6.6 and 6.7, showed an extra dip and peak, respectively. Results for one vapor flow data point are shown in Figure 6.23.

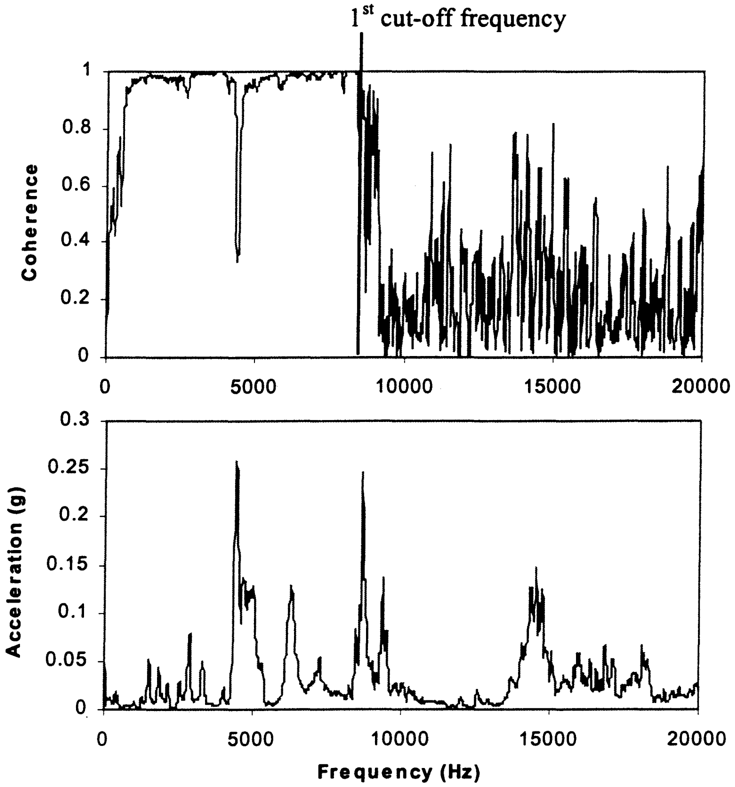

Figure 6.23 – Typical EEV coherence and acceleration spectra for vapor flow

Further investigation of this phenomenon revealed that the valve itself was apparently vibrating significantly at this frequency. A full discussion of this investigation and the experimental results are given in Appendix I.

6.10 Additional figures

This section contains some additional figures referred to in the body of the chapter which supplement the data presented.

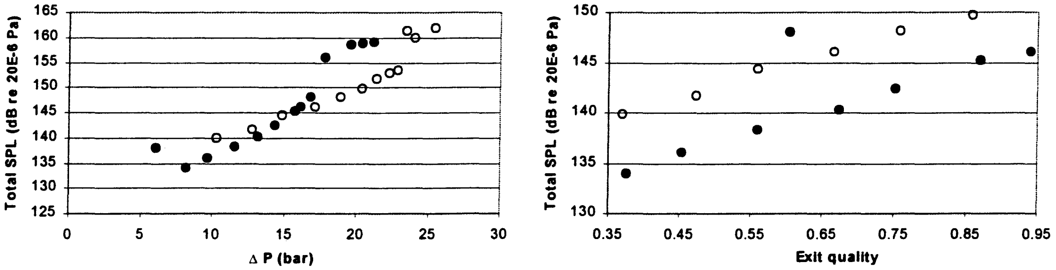

Figure 6.24 – Capillary tube results

Capillary tube: 1.626mm I.D., 32in. length
Dark circles: Mass flow rate = 75 lbm/hr
Open circles: Mass flow rate = 100 lbm/hr
Outlet pressure: 4 bars

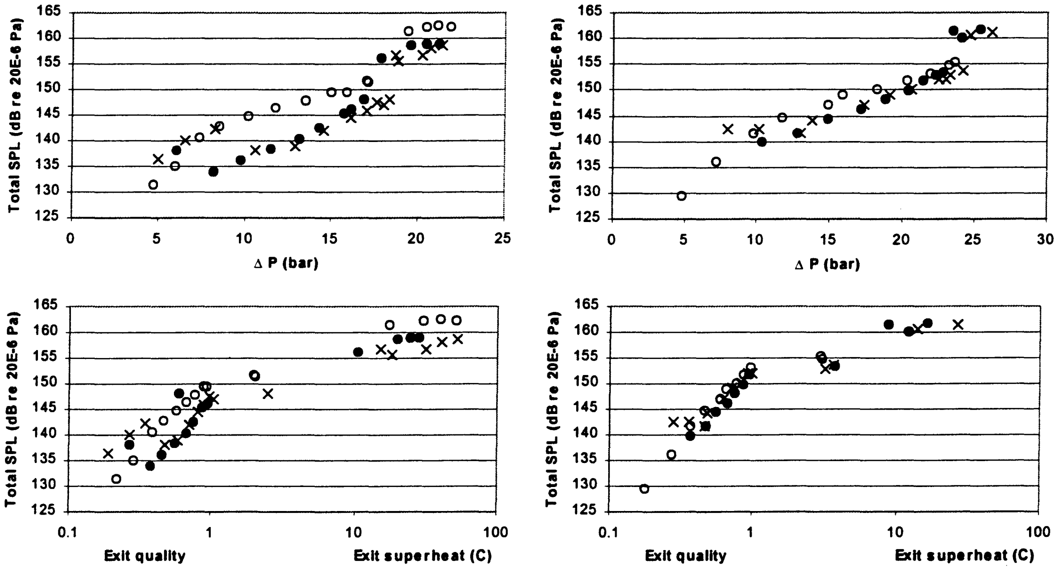

Figure 6.25 – 2 Capillary tubes and one orifice tube of Figure 6.10

Left column: Mass flow rate = 75 lbm/hr
Right column: Mass flow rate = 100 lbm/hr
Outlet pressure: 4 bars

Chapter 7

Conclusions and Recommendations

Experimental testing and investigation on expansion devices has shown:

- For a given expansion device, far-field expansion noise appears to be primarily a function of mass flow rate through the expansion device, pressure difference (ΔP) across the device, and the quality at the exit of the device. The expansion noise increases with increases in each of these variables.
- For pure vapor flow at the exit of the expansion device, far-field expansion noise is approximately white noise (noise of equal sound pressure level at all frequencies) over the audible frequency range (20Hz - 20kHz).
- As the quality at the exit of the expansion device decreases the higher frequency sound waves of the far-field expansion noise are more sharply attenuated than the lower frequency waves and the far-field expansion noise becomes pink noise over the audible frequency range.
- Downstream screens at the outlet of an orifice tube significantly reduces the far-field expansion noise from an orifice tube at all operating conditions.
- For vapor flow in refrigerant tubes, high frequency sound waves are more sharply attenuated with distance along the tube, and internal sound pressure attenuation with distance agrees closely with theoretical predictions for visco-thermal attenuation in tubes (See [11] and Appendix C).
- The downstream tube wall acts as a band-pass filter, preferentially transmitting only certain frequencies and can be well predicted from correllations in the literature (see [28]).
- The IEC standard model [20] for predicting aerodynamic noise from ideal gas flow through large industrial control valves shows expansion noise to primarily be functions of, and to increase with, pressure difference (ΔP) across the device, mass flow through the device, and speed of sound at the exit of the device. When applied to orifice tubes, expansion valves, and short capillary tubes in refrigerant vapor flow, the model predicts our noise data well.

List of References

1. Reethof, G., "Control Valve Regulator Noise Generation, Propagation, and Reduction", *Noise Control Engineering*, September-October 1977, pp.74-85.

2. Lighthill, M.J., "Jet Noise", *AIAA Journal*, 1, July 1963.

3. Fox, Robert W. and Alan T. McDonald, Introduction to Fluid Mechanics, 4th ed., John Wiley and Sons, Inc., New York, 1992.

4. Idel'chik, I. E., (Tanslated by Greta Malyaskaya), Handbook of Hydraulic Resistance, 3rd ed., CRC Press, Boca Raton, FL., 1994.

5. Stoecker, W.F. and J.W. Jones, Refrigeration and Air Conditioning, 2nd ed., McGraw-Hill, Inc., New York, 1986.

6. Hodge, B.K. and Keith Koenig, Compressible Fluid Dynamics, Prentice Hall, New Jersey, 1995.

7. Hrnjak, P.S., and G. Singh, *Experimental Study on Orifice Tube Performance*, paper in progress.

8. Woodall, R.J., and C.W. Bullard, "Development, Validation, and Application of a Refrigerator Simulation Model", ACRC TR-99, Air Conditioning and Refrigeration Center, University of Illinois at Urbana-Champaign, 1996.

9. Kinsler, Lawrence E., Austin R. Frey, Alan B. Coppens, and James V. Sanders, Fundamentals of Acoustics, 3rd ed., John Wiley and Sons, inc., New York, 1982.

10. ASTM Standard E 1050-90 – “Standard Test Method for Impedance and Absorption of Acoustical Materials Using a Tube, Two Microphones, and a Digital Frequency Analysis System”

11. Rodarte E., Singh G., Miller N. R. and Hrnjak P. "Sound Attenuation in Tubes due to Visco-Thermal Effects", submitted for publication.

12. Pierce, Alan D., Acoustics, 2nd ed., Acoustical Society of America, New York, 1989.

13. Tipler, Paul A., Physics for Scientists and Engineers, 3rd.ed, Vol. 1, Worth Publishers, Inc., New York, 1990.

14. HP 3562A Digital Signal Analyzer Operating Manual - Hewlett Packard.

15. Blaser, D.A. and J.Y. Chung – "A Transfer Function Technique for Determining the Acoustic Characteristics of Duct Systems with Flow", *Inter-noise*, 1978, p. 902-908.

16. Blaser, D.A. and J.Y. Chung – "Transfer function method of measuring in-duct acoustic properties. I. Theory", *J. Acoust. Soc. Am* (68), 1980, p. 907-913.

17. Blaser, D.A. and J.Y. Chung - "Transfer function method of measuring in-duct acoustic properties. II. Experiment", *J. Acoust. Soc. Am* (68), 1980, p. 914-921.

18. Boden, Hans and Mats Aborn - "Influence of errors on the two-microphone method for measuring acoustic properties in ducts", J. *Acoust. Soc. Am* (79), 1986, p. 541-549.

19. Boden, Hans and Mats Aborn - "Error analysis of two-microphone measurements in ducts with flow", J. *Acoust. Soc. Am* (83), 1988, p. 2429-2438.

20. IEC Standard 534-8-3:1995, "Industrial -process control valves - Part 8: Noise considerations - Sections 3: Control valve aerodynamic noise prediction method", International Electrotechnical Commission.

21. ISA Standard S75.01, "Flow Equations for Sizing Control Valves", Instrument Society of America.

22. ISA Standard S75.02, "Control Valve Capacity Test Procedure", Instrument Society of America.

23. Baumann, H.D., "A Firm New Handle on Valve Noise", *Chemical Engineering,* December 1996.

24. Personal correspondence with Dr. Hans D. Baumann

25. Howell, John R. and Richard O. Buckius, Fundamentals of Engineering Thermodynamics, 2nd ed., McGraw-Hill, Inc., New York, 1992.

26. Norton, M.P. and Bull, M.K. "Mechanisms of the generation of external acoustic radiation from pipes due to internal flow disturbances". Journal of Sound and Vibration (1984) 94 (1), 105-146.

27. Catalogue - Peoria Valve and Fitting Co., Peoria, IL.

28. Miller, N. R., Hrnjak, P. S., Rodarte, E., and George Singh, "Refrigerant Expansion Noise Propagation Through Downstream Tube Walls." Paper no. 1999-01-1197 and presentation at the 1999 SAE International Congress and Exposition.

29. Stoecker, W.F., Design of Thermal Systems, 3rd ed., McGraw-Hill, Inc., New York, 1989.

30. Soave, Giorgio. "Equilibrium constants from a modified Redlich-Kwong equation of state", *Chemical Engineering Science* (27), 1972, pp. 1197-1203.

31. E-mail correspondence with Professor Mike Philpot, Dept. of Mechanical and Industrial Engineering, University of Illinois at Urbana-Champaign.

32. 1997 ASHRAE Fundamentals, SI Edition, American Society of Heating, Refrigeration, and Air-Conditioning Engineers, Inc., Atlanta, GA., 1997.

33. Althouse, Andrew D., Carl H. Turnquist, and Alfred F. Bracciano, Modern Refrigeration and Air Conditioning, The Goodheart-Willcox Company, Inc., Tinley Park, IL., 1996.

34. Eaton Corporation: Automotive Controls Div., "Thermostatic Expansion Valves for Automotive A/C Applications" – Prepared for University of Brighton Symposium, Developments in Air Conditioning Systems, 20-23 April, 1993.

Appendix A

Installation of the expansion devices into the experimental test facility

A.1 Orifice tube

As described in Chapter 2, specific installations had to be designed to install each of the expansion devices tested into the experimental test facility. The orifice tube installation is illustrated in Figure A.1. It is simply two copper pipes brazed together with a metal ring in between. The ring-hole diameter fits around the exit section of an inserted orifice tube up to the o-rings. Flow then pushes the orifice tube into place and the o-ring seals it against the metal ring. The entire section can then be installed in the system connected by compression fittings at each end. The compression fittings allow for easy removal/exchange of expansion devices and are also assumed to provide negligible flow disturbances or reflections.

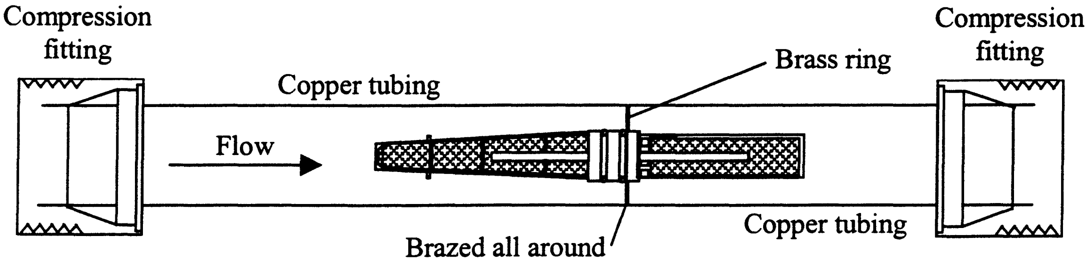

Figure A.1 – Orifice tube installation

A.2 Thermostatic expansion valve

As described in Chapter 5, the thermostatic expansion valve (TXV) was tested with its orificial element fully open and its evaporator inlet and exit ports blocked off. The TXV installation is illustrated in Figures A.2 and A.3. It is two blocks made of copper or brass that can seal to either side of the valve with threaded screws and O-rings. The blocks contain holes which align with the TXV inlet and outlet ports and have diameters equal to the O.D. of the copper tubing in the test section. Tubing of that size can then be brazed to the blocks and installed in the test section with compression fittings on the ends of the tubes.

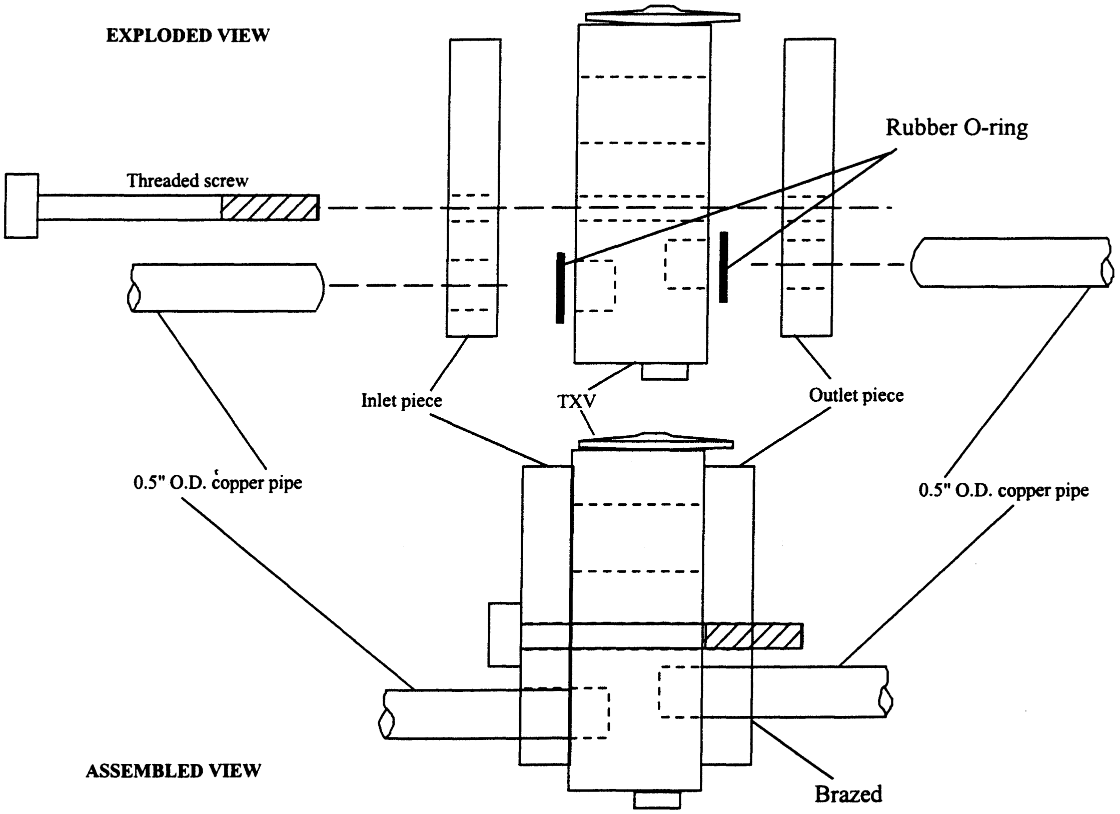

Figure A.2 – Thermostatic expansion valve installation

A.3 Electronic expansion valve

The electronic expansion valve inlet and outlet ports are designed to accommodate standard fittings and are easily installed in the experimental test facility as such.

A.4 Capillary tube

In order to accurately control the capillary tube outlet geometry and insertion depth, circular blocks were designed and installed as illustrated in Figure A.4. The blocks were designed with small holes in the center that could be drilled out to the exact O.D. of the capillary tube being used. The tubing brazed to the block could then be installed in the experimental test facility using compression fittings.

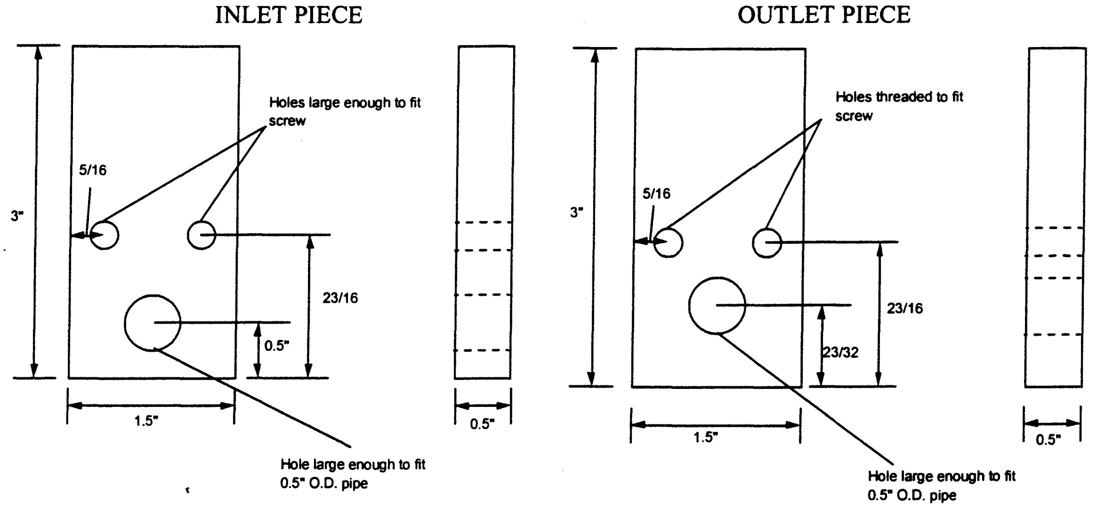

Figure A.3 – Block design for one of the tested thermostatic expansion valves
All dimensions in inches. 0.5in O.D. tubing in test section. Block thickness was arbitary.

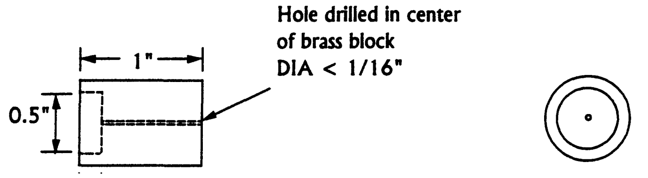

Side View **End View**

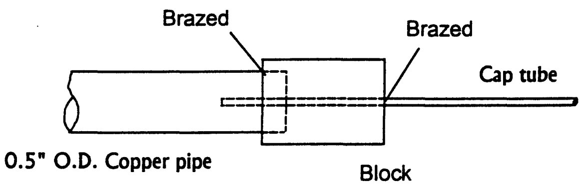

Assembled View

Figure A.4 – Capillary tube installation (outlet)
Block may be brass or copper. 0.5in. O.D. tubing in test section

If the capillary tube O.D. is of standard size, the inlet can be installed using standard fittings. If not, a block, like that used at the outlet, can be used.

A.5 Capillary tube with outlet cone

As discussed in Chapter 6, the capillary tube outlet cones were designed to smoothly transition between the capillary tube inner diameter and the inner diameter of the downstream tubing. The cones were made by stereolithography with tolerances at least +/- 0.001in. An illustration of the cones is given in Figure A.5.

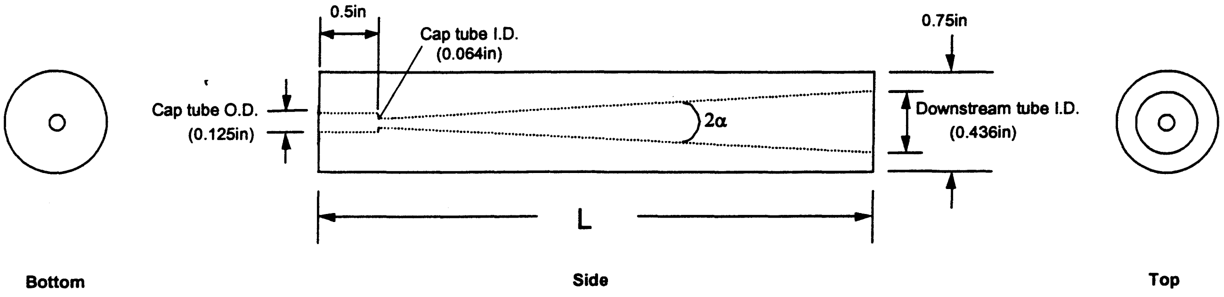

Figure A.5 - Illustration of capillary tube outlet cone
The length, L, determines the angle, 2α.

The outlet section had to secure the capillary tube, outlet cone, and downstream tubing in place in a leak-tight fashion. A successful design was developed which used a specially modified compression fitting, as shown in Figure A.6. Note from the Figure that the capillary tube is bent slightly just upstream of the outlet cone. The purpose of the bend is to allow the capillary tube to expand and contract there in response to temperature changes. Without a place to naturally bend, the capillary tube may be more likely to move in and out of its position in the cone, even when epoxy is applied.

After testing, both capillary tube outlet assemblies tested were observed to be intact as assembled. Charring and surface damage to the SLA nozzles should not occur until 265°C [31].

(A) Standard reducing union
T=0.75", Tx=0.5", E=0.41"

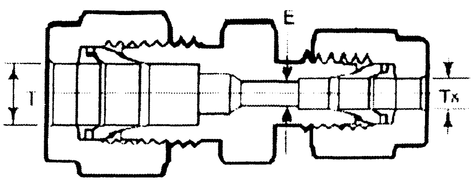

(B) Modified reducing union
T=0.75", Tx=0.5", E=0.43"

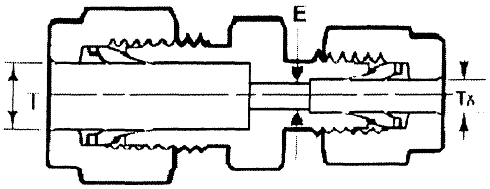

(C) Cone assembly

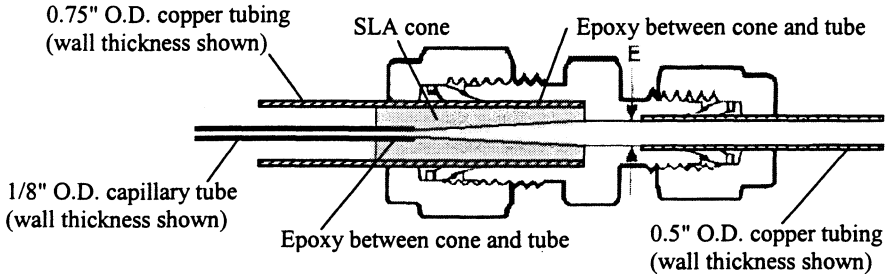

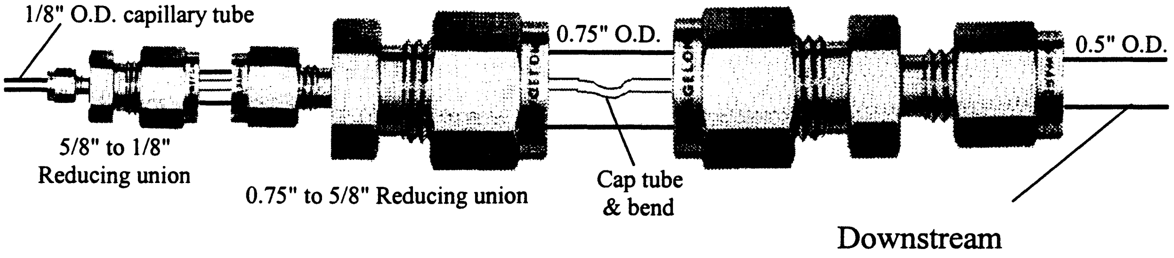

(D) Extended cone assembly

Figure A.6 - Capillary tube outlet cone assembly
Drawings of compression fittings from [25].

Appendix B

Data Acquisition

B.1 Set-up

All thermocouples, pressure transducers, and mass flow meters used for measurement in the experimental test facility (Chapter 2) are fed into a 16-channel HP 75000 Series B multiplexer which is connected by a GP-IB interface to a PC. An HP 3562A 2-channel Dynamic Signal Analyzer is also connected by GP-IB interface to the PC. The microphones and accelerometers are then connected by manufacturer-supplied cables to PCB ICP® 480C02 unity-gain signal conditioners and power supplies which are then connected by BNC-to-BNC cables to the signal analyzer. A schematic of the complete data acquisition system is shown in Figure B.1

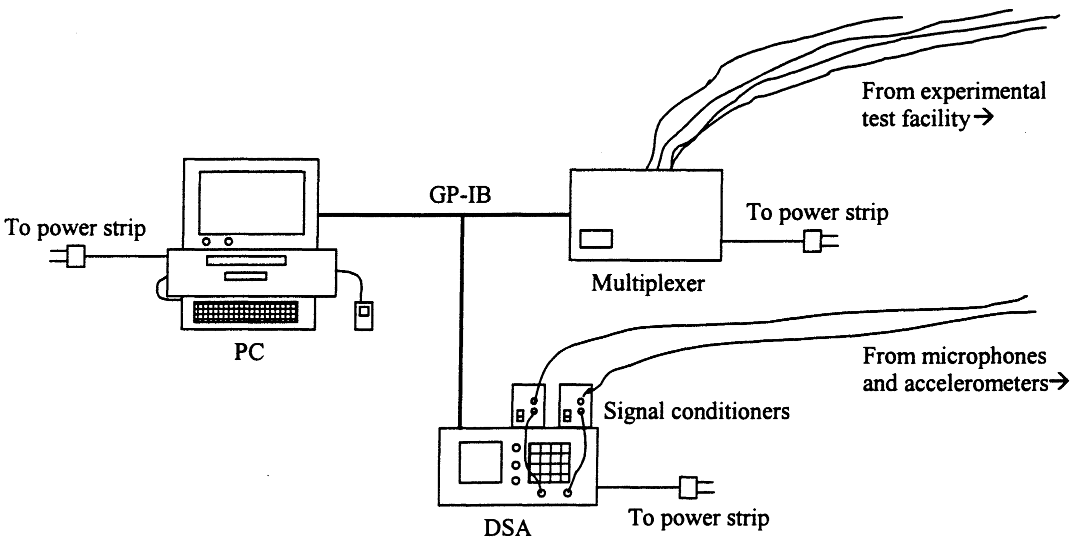

Figure B.1 – Data acquisition set-up

The inputs to the multiplexer must be voltage inputs and contain a lead to high and low voltage, and the low voltage lead must also be connected by wire to ground. If the input from a measurement device is a current input, a resister must be placed across the high and low voltage leads and soldered or tightly wound to the leads. There is a high voltage, a low voltage, and a ground port for each of the 16 channels in the multiplexer. An illustration is given in Figure B.1.

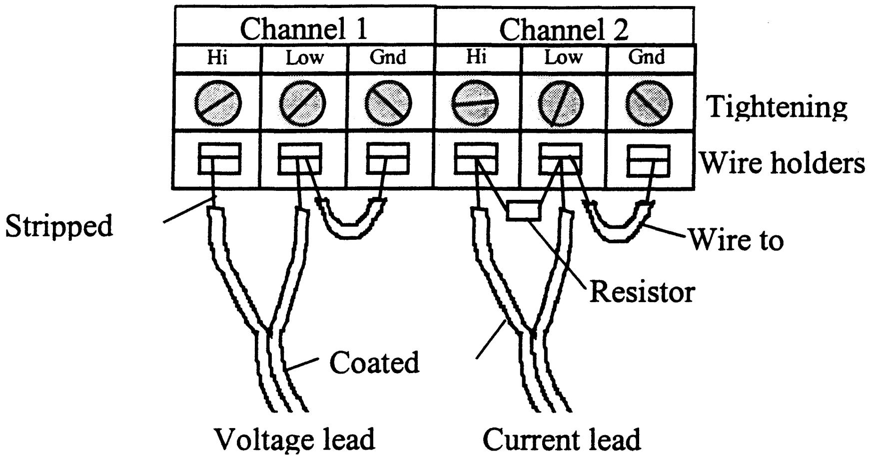

Figure B.2 - Illustration of connection of instrument leads to multiplexer channels

B.2 HPVee code

Data acquisition and monitoring of the experimental test facility while the system is running is done by an *HPVee* 3.0 code with graphical interface. The code, when running, updates all of the measured system variables (pressures, temperatures, and mass flow rates) and calculated quantities (qualities, enthalpies, superheats, densities, and speeds of sound) at a constant rate of approximately 1x/sec. Most of these values are then displayed numerically and some are displayed graphically versus time. A capture of the screen during operation is shown in Figure C.6. The code actually reads the measured voltage inputs from the multiplexer and converts them using calibrations. The standard type-T thermocouple calibrations are a built-in function of *HPVee*, whereas the pressure-transducer and mass flow meter calibrations must be programmed by the user into the code. More detail on these calibrations is given below. The calculated quantities are computed using curve fits of various thermophysical properties, as described in Appendix E.

While the code is running, a secondary loop within the code can be activated which configures the DSA to the proper settings to take internal sound pressure and external pipe-wall acceleration measurements, takes the measurements, and then writes the DSA data and the updated system variables to a data file. The user is then asked to name and save the data file. This data file is saved as a text file which can be opened with tab delineation in *EXCEL*.

The entire *HPVee* code, including calibrations and additional formulas are included at the end of this Appendix. Also included is a saved data file of one data point. It should be noted that this code has been modified many times to add or remove variables or measurements. However, the version of the code included here is the most robust and easily modified to accommodate any similarly configured system.

B.3 Calibrations

B.3.1 Micro Motion® mass flow calibration

The mass flow calibration for the Micro Motion® mass flow meters was done as follows:

1. A resistor, of nominal value approximately 220Ω, was placed across the current leads from the transmitter and soldered or tightly wound to the leads. The leads were then input to a one of the multiplexer channels, as described above.
2. With the flow sensor installed in the test facility and the system fully charged with refrigerant, the *no-flow* voltage from the transmitter was monitored and recorded for 10 updates (about 10 sec.) using a modified version of the attached *HPVee* code, and then averaged. Since all Micro Motions are known to have a current range of 4-20mA over their full mass flow range, the average no-flow voltage was divided by 4mA to "back-out" the effective resistance across the current leads, including resistances in the wires and within the mutliplexer. The effective resistance was usually within ± 2Ω of the nominal value. One data set is given for example in Table B.1.
3. The mass flow - current relationship is known to be linear for all Micro Motions. Hence, the following figure was drawn:

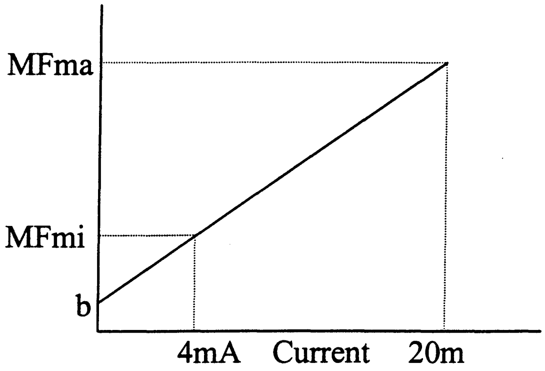

Figure B.3 - Figure for Micro Motion® calibration

4. The mass flow - voltage relationship can then be established as follows:

$$MF(V) = \{[MFmax\text{-}MFmin]/[(20\text{-}4mA)/R_{effective}]\}V + \{[MFmax\text{-}MFmin]/[(20\text{-}4mA)/R_{effective}]\}V_{noflow}$$

which is in the form of $y = mx + b$. MF stands for mass flow rate.

The mass flow rate range is different for each model flow meter and may be changed using a hand-held calibration unit.

Table B.1 – No-flow voltages recorded from *HPVee* for 10sec on 5-13-98

For high-pressure side mass flow meter

	No-flow voltage
	0.8843
	0.8784
	0.8682
	0.8696
	0.8647
	0.8677
	0.8706
	0.8706
	0.877
	0.8813
Average	***0.87324***
St. Dev.	***0.006198903***
Effective Resistance	***218.31***
Nominal Resistance	***220 Ohms***

B.3.2 Micro Motion temperature calibration

The micro motion temperature calibration is standard for each model (e.g. 5°C/V). The temperature output leads from a Micro Motion® is a voltage output and requires no resistor across the multiplexer channel.

B.3.3 Thermocouple calibrations

The thermocouples are all type-T thermocouples and have standard calibrations (voltage to temperature) which can be automatically accessed within *HPVee.*

B.3.4 Pressure transducer calibrations

The pressure transducer calibrations (voltage to pressure) were obtained by recording the voltage for a number of known pressures within the range of the transducer and fitting a straight line through the data. The R^2-value of the line should be nearly 1 (i.e. the data should be very linear). A sample calibration is given in Figure B.4.

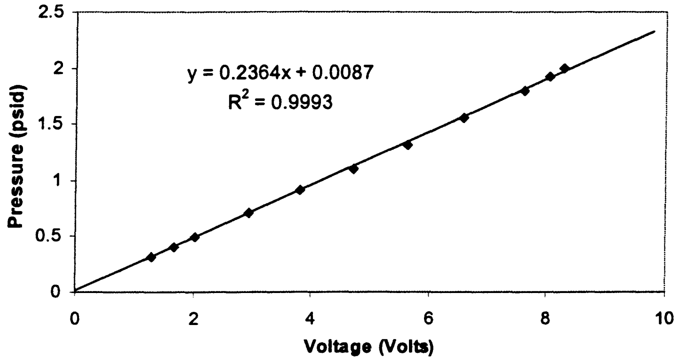

Figure B.4 – Pressure Transducer calibration 8-7-97
Validyne Model DP15-42/1542N1S4A - S/N 37064

B.3.5 Venturi calibration

Although not given in the attached *HPVee* code, a venturi flow meter was sometimes used in the experimental test facility as well as in the Nitrogen test facility (See Appendix F). The venturi equations are standard, with the empirical coefficient coming from comparisons of venturi readings to Micro Motion® readings. The *EES* code used for the venturi is given below. This code can also be implemented in the *HPVee* code using appropriate thermophysical property curve fits (see Appendix E).

```
{Input Data}
Pabs=101.325 {kPa}
Dt=0.1890.0254 {m}
Di=0.7250.0254 {m}
Ck=0.948

{Areas}
At_venturi=piDt^2/4   {m^2}
Ai_venturi=piDi^2/4   {m^2}

{Calculations}
Delta_P=DPpsiconvert(inH2O,Pa) {Pa}
rho_i=1217{DENSITY(R134a,T=Tf1,P=Pf1)} {kg/m^3}
{Pf1=Pabs+PventInRealconvert(psi,kPa) {kPa}
Pf2=Pf1-delta_Pconvert(Pa,kPa)}
E=sqrt(Beta^4/(1-Beta^4))
Beta=Dt/Di
mdot=(Ck/1.05)YAt_venturisqrt((2Delta_prho_i)/(1-
beta^4))Convert(kg/s,lbm/hr) {kg/s}
Y=(((1-(Dt/Di)^4)(k/(k-1))(pf2/pf1)^(2/k)(1-(pf2/pf1)^((k-
   1)/k)))/((1-(Dt/Di)^4(pf2/pf1)^(2/k))(1-pf2/pf1)))^(1/2)

Dppsi=.05685

{This section is to obtain the value of the isentropic
coefficient k}
Cv=Cp-R {kJ/kg-k}
Mm=MOLARMASS(R134a) {kg/kmol}
Ru=8.3144 {kJ/kmol-k}
R=Ru/Mm {kJ/kg-K}
Cp=SPECHEAT(R134a,T=Tf1,P=Pf1) {kJ/kg-K}
k=Cp/Cv

mdot2=mdotconvert(kg/s,lbm/hr) {lbm/hr}
c=sqrt(k(R1000)(Tf1+273.15)) {m/s}
```

HPVEE code

Figure B.5 shows the actual *HPVee* code network and the documentation of the code, including all curve fits and calibrations and a sample data file, follows.

```
Source file: "D:\\VEE
Programs\\Cap.Tube.Tests.vee"
File last revised: Thu Mar 25 15:47:10 1999
Date documented: Wed Jul 21 11:08:52 1999
VEE revision: 3.21
Convert Infinity on Binary Read: no
Title: "Untitled"
Delete globals at PreRun: no
Trig mode: Degrees

0: State Driver: "E1326 Multimeter ( @
70903)"
Function: Temperature -Deg C
Thermal Transducer: Thermocouple T
Reading mode: Scan Channel List
Channel list: 106 to 115
Trigger Options: Trigger Defaults
Instrument Options: Auto Zero: On
Instrument Options: Line Freq: 60 Hz

15: Until Break: "Until Break"

18: Constant: "Themocouple Type"
Constant Value: 8

20: State Driver: "E1326 Multimeter ( @
70903)"
Function: DC Voltage
Reading mode: Scan Channel List
Channel list: 100 to 105
Trigger Options: Trigger Defaults
Instrument Options: VoltRange: 8.000
Instrument Options: Aperture: 10 uSec
Instrument Options: Auto Zero: On
Instrument Options: Line Freq: 60 Hz
Instrument Options: Resolution: 490. uV

34: Formula: ""
Formula: a[1]

35: AlphaNumeric: "T Inlet TS (C)"

36: Formula: ""
Formula: a[3]

38: Formula: ""
Formula: a[4]

40: AlphaNumeric: "T Outlet TS (C)"

42: AlphaNumeric: "T Main Heater Outlet
surface (C)"

45: Formula: ""
Formula: a[5]

46: Formula: ""
Formula: a[6]

48: Formula: ""
Formula: a[7]

49: Formula: ""
Formula: a[9]
```

```
52: AlphaNumeric: "T Main Heater Middle
Pos. (C)"

53: AlphaNumeric: "Tsubcooler 1 (C)"

54: AlphaNumeric: "Tout surface (C)"

57: Formula: "Calibration Inlet Press "
Formula: -(-1.275+6.8937A[0]+1.01325)

58: AlphaNumeric: "P Inlet TS (bara)"

59: Formula: "Calibration Outlet Press. "
Formula: -(-1.5+1.3811A[1]+1.01325)

60: Formula: "Calibration Mass Flowmeter"
Formula: -150+169.37096A[2]

61: Formula: "Calibration Power to Heaters"
Formula: -4000A[3]/5

63: AlphaNumeric: "Mass Flow (lb/hr)"

64: AlphaNumeric: "Power (W)"

71: Y Plot: "Strip Chart"

78: File Selection: "File Name Selection"
Prompt: "Enter File Name:"
Initial Directory: "d:\George\"
Initial File: "."
Select File for: Writing

80: To File: "To File"
Transactions:
 1: WRITE TEXT "Pin (bara)" EOL
 2: WRITE TEXT Pinlet REAL STD EOL
 3: WRITE TEXT "Pout (bara)" EOL
 4: WRITE TEXT Pout REAL STD EOL
 5: WRITE TEXT "Mflow1 (lbm/hr)" EOL
 6: WRITE TEXT MFlow REAL STD EOL
 7: WRITE TEXT "Mflow2 (lbm/hr)" EOL
 8: WRITE TEXT Mflow2 EOL
 9: WRITE TEXT "Power (W)" EOL
 10: WRITE TEXT Power REAL STD EOL
 11: WRITE TEXT "Temps (C)" EOL
 12: WRITE TEXT Thmocpls REAL STD EOL
 13: WRITE TEXT DandT DATE:WDMY
TIME:HMS:H12 EOL
 14: WRITE TEXT "Header1" EOL
 15: WRITE TEXT HEADER1 REAL STD
EOL
 16: WRITE TEXT "Frequency (Hz)" EOL
 17: WRITE TEXT f EOL
 18: WRITE TEXT "Transfer function" EOL
 19: WRITE TEXT TF EOL
 20: WRITE TEXT "Coherence" EOL
 21: WRITE TEXT CO EOL
 22: WRITE TEXT "Power spectrum" EOL
 23: WRITE TEXT PS EOL
 24: WRITE TEXT "Acceleration1" EOL
 25: WRITE TEXT A1 EOL
 26: WRITE TEXT "Acceleration2" EOL
 27: WRITE TEXT A2 EOL
To: D:\George\10deg11.vee
```

```
89: Start: "Start"

97: Break: "Break"

104: If/Then/Else: "If/Then/Else"
 Expressions:
  1: A==1

105: Toggle Control: "ANALIZER"
 Constant Value: 0

106: If/Then/Else: "If/Then/Else"
 Expressions:
  1: A==1

107: Toggle Control: "STOP"
 Constant Value: 0

113: Formula: "DATE & TIME"
 Formula: now()

147: Direct I/O: "hp3562A ( @ 720)"
 Transactions:
  1: WRITE TEXT "STRT" EOL
  2: WAIT INTERVAL:60
  3: WRITE TEXT "DDAS" EOL
  4: READ TEXT x REAL
  5: READ TEXT HEADER1 REAL
ARRAY:66
  6: READ TEXT TF REAL ARRAY:X-66
  7: WRITE TEXT "COHR" EOL
  8: WRITE TEXT "DDAS" EOL
  9: READ TEXT y REAL
  10: READ TEXT HEADER2 REAL
ARRAY:66
  11: READ TEXT CO REAL ARRAY:Y-66
  12: WRITE TEXT "PSP1" EOL
  13: WRITE TEXT "DDAS" EOL
  14: READ TEXT z REAL
  15: READ TEXT HEADER3 REAL
ARRAY:66
  16: READ TEXT PS REAL ARRAY:Z-66

149: AlphaNumeric: "P Outlet TS (bara)"

165: ColorAlarm: "T Main Surface Alarm"
High text: ""
Mid text: ""
Low text: ""
High limit: 85
Low limit: 15

168: ColorAlarm: "T Main Mid  Alarm"
High text: ""
Mid text: ""
Low text: ""
High limit: 85
Low limit: 15

190: UserObject: "UserObject"
Trig mode: Degrees

190.10: Formula: "f"
Formula: ramp(num, fmin, fmax)

190.11: Formula: "num(int)"
```

```
 Formula: HEADER1[1]

 190.12: Formula: "fmin(Hz)"
 Formula: HEADER1[64]

 190.13: Formula: "fmax(Hz)"
 Formula: (HEADER1[1]-1)HEADER1[55]

 199: UserObject: "UserObject"
 Trig mode: Degrees

 199.0: Formula: "c(m/s)"
 Formula: 156.1-.2038pp-.0007738pp^2-2.783e-
7pp^3+.3115T-
.001571T^2+.00001209T^3+.002841ppT-
.00001943ppT^2+.00001139pp^2T-2.629e-
8pp^2T^2

 199.6: Formula: "a"
 Formula: 1.890651525

 199.7: Formula: "b"
 Formula: .000649616

 199.8: Formula: "rho(kg/m3)"
 Formula: z(.5(sqrt(Tk)(bpk+RTk)+sqrt(abs(-
4apksqrt(Tk)+Tk(bpk+RTk)^2)))/(pksqrt(Tk)))^
(-1)

 199.9: Formula: "R"
 Formula: 0.081489758

 199.10: Formula: "bar->psia"
 Formula: A/.06895

 199.14: Formula: "bar->kPa"
 Formula: 100A

 199.35: Formula: "T->Tk"
 Formula: A+273.15

 199.36: Formula: "z"
 Formula: 1.02+.00006632pk+6.124e-8pk^2-
6.001e-11pk^3-.001539T+.00002327T^2-
2.645e-8T^3-2.201e-7pkT-2.714e-
8pkT^2+2.783e-10pk^2T+1.173e-11pk^2T^2

200: AlphaNumeric: "c out (m/s)"

201: AlphaNumeric: "rho out (kg/m3)"

203: Formula: "Inlet Sup"
 Formula: B-(-24.5339+10.29703A-
0.5354664A^2+0.01667852A^3-
0.00020758A^4)

204: Formula: "Outlet Sup"
 Formula: B-(-24.5339+10.29703A-
0.5354664A^2+0.01667852A^3-
0.00020758A^4)

205: AlphaNumeric: "Inlet Sup (C)"

206: AlphaNumeric: "Outlet Sup (C)"

209: Formula: "Mflow2 Cal"
```

```
Formula: -150+172.32862a[5]

210: AlphaNumeric: "Mass Flow 2 (lb/hr)"

213: Direct I/O: "hp 3562A Start up"
 Transactions:
  1: WRITE TEXT "RST" EOL
  2: WRITE TEXT "LNRS" EOL
  3: WRITE TEXT "FRS;CF10kHZ" EOL
  4: WRITE TEXT "ICPL;C1AC;C2AC" EOL
  5: WRITE TEXT "AU1;AU2" EOL
  6: WRITE TEXT
 "EUV135.7mVEU;EUL1\'psi\'" EOL
  7: WRITE TEXT
 "EUV240.95mVEU;EUL2\'psi\'" EOL
  8: WRITE TEXT "AVG;STBL;NAVG50"
EOL
  9: WRITE TEXT "UNIT;LSUN;VLTS" EOL
  10: WRITE TEXT "UNIT;PSUN;VLTS" EOL
  11: WRITE TEXT "FRQR" EOL
  12: WRITE TEXT "CORD;MAG" EOL
  13: WRITE TEXT "UPLO" EOL
  14: WRITE TEXT "B" EOL
  15: WRITE TEXT "FRQR" EOL
  16: WRITE TEXT "CORD;PHSE" EOL
  17: WRITE TEXT "AB" EOL
  18: WAIT INTERVAL:2
  19: WRITE TEXT "SCAL;XSCL0,20000HZ"
EOL
  20: WRITE TEXT "A" EOL

214: AlphaNumeric: "T Condenser (C)"

215: Formula: ""
 Formula: a[8]

216: AlphaNumeric: "T subcooler outlet (C)"

217: OK : " OK "
 Assigned to Enter Key: yes
 Assigned to Escape Key: yes

219: Direct I/O: "hp3562A ( @ 720)"
 Transactions:
  1: WRITE TEXT
 "EUV1110.0mVEU;EUL1\'g\'" EOL
  2: WRITE TEXT
 "EUV29.75mVEU;EUL2\'g\'" EOL
  3: WRITE TEXT "B" EOL
  4: WRITE TEXT "PSP2" EOL
  5: WRITE TEXT "CORD;MAG" EOL
  6: WRITE TEXT "A" EOL
  7: WRITE TEXT "STRT" EOL
  8: WAIT INTERVAL:65
  9: WRITE TEXT "DDAS" EOL
  10: READ TEXT x REAL
  11: READ TEXT HEADER4 REAL
ARRAY:66
  12: READ TEXT A1 REAL ARRAY:X-66
  13: WRITE TEXT "PSP2" EOL
  14: WRITE TEXT "DDAS" EOL
  15: READ TEXT y REAL
  16: READ TEXT HEADER5 REAL
ARRAY:66
  17: READ TEXT A2 REAL ARRAY:X-66
```

```
227: Formula: "T Micro cal"
 Formula: a[4]/.005

228: AlphaNumeric: "T Micro (C)"

240: UserObject: "xin"
 Trig mode: Degrees

240.0: Formula: "x"
 Formula: (h+(Q/m)-hliq)/hlg

240.1: Formula: "h (kJ/kg)"
 Formula:
49.41009399+1.268025199T+.002512892T^2+.
062074564P+.000242824P^2+.000514016PT

240.2: Formula: "mdot (kg/s)"
 Formula: .000126mdot

240.3: Formula: "Q (kW)"
 Formula: Q/1000

240.4: Formula: "hliq (kJ/kg)"
 Formula:
49.30567+1.351244T+.00153503T^2-
.000032219T^3+.00000049110T^4

240.5: Formula: "hlg (kJ/kg)"
 Formula: 197.1772-.71352T-.0016744T^2-
.000090834T^3-
.00000059096T^4+.000000042306T^5-
.00000000034272T^6

241: AlphaNumeric: "xin"

242: UserObject: "xout"
 Trig mode: Degrees

242.0: Formula: "x"
 Formula: (h+(Q/m)-hliq)/hlg

242.1: Formula: "h (kJ/kg)"
 Formula:
49.41009399+1.268025199T+.002512892T^2+.
062074564P+.000242824P^2+.000514016PT

242.2: Formula: "mdot (kg/s)"
 Formula: .000126mdot

242.3: Formula: "Q (kW)"
 Formula: Q/1000

242.4: Formula: "hliq (kJ/kg)"
 Formula:
49.30567+1.351244T+.00153503T^2-
.000032219T^3+.00000049110T^4

242.5: Formula: "hlg (kJ/kg)"
 Formula: 197.1772-.71352T-.0016744T^2-
.000090834T^3-
.00000059096T^4+.000000042306T^5-
.00000000034272T^6

243: AlphaNumeric: "xout"

248: Formula: ""
```

Formula: a[0]

249: AlphaNumeric: "T Main Heater Outlet refrig (C)"

250: Sliding Collector: "Sliding Collector"
Array size: 50
Trigger every: 1

251: Formula: "mean(x)"
Formula: mean(x)

252: AlphaNumeric: "Avg. Mass Flow "

Sample data file:

Pin (bara)
17.64074077
Pout (bara)
4.162714893
Mflow1 (lbm/hr)
74.69935827
Mflow2 (lbm/hr)
75.00328607
Power (W)
1292.578125

Temps (C)
{in order of multiplexer output}
61.8203125
61.61523438
9.91E+37
10.08789063
41.77636719
3.341796875
12.27929688
20.05957031
16.07128906
12.22753906
Fri 17/Jul/1998 4:42:23 PM

Header1
{Following is the 66 line header file which contains information about the data collection as described in [12]}

The frequency range follows

The measured transfer function, power spectra, coherence spectra, and acceleration spectra follow. For the power, coherence, and acceleration spectra, each line is the data for each recorded frequency (0Hz, 25Hz, 50Hz,...) in the frequency range. For the transfer function, each set of two lines is the data (real, imaginary) for each recorded frequency.

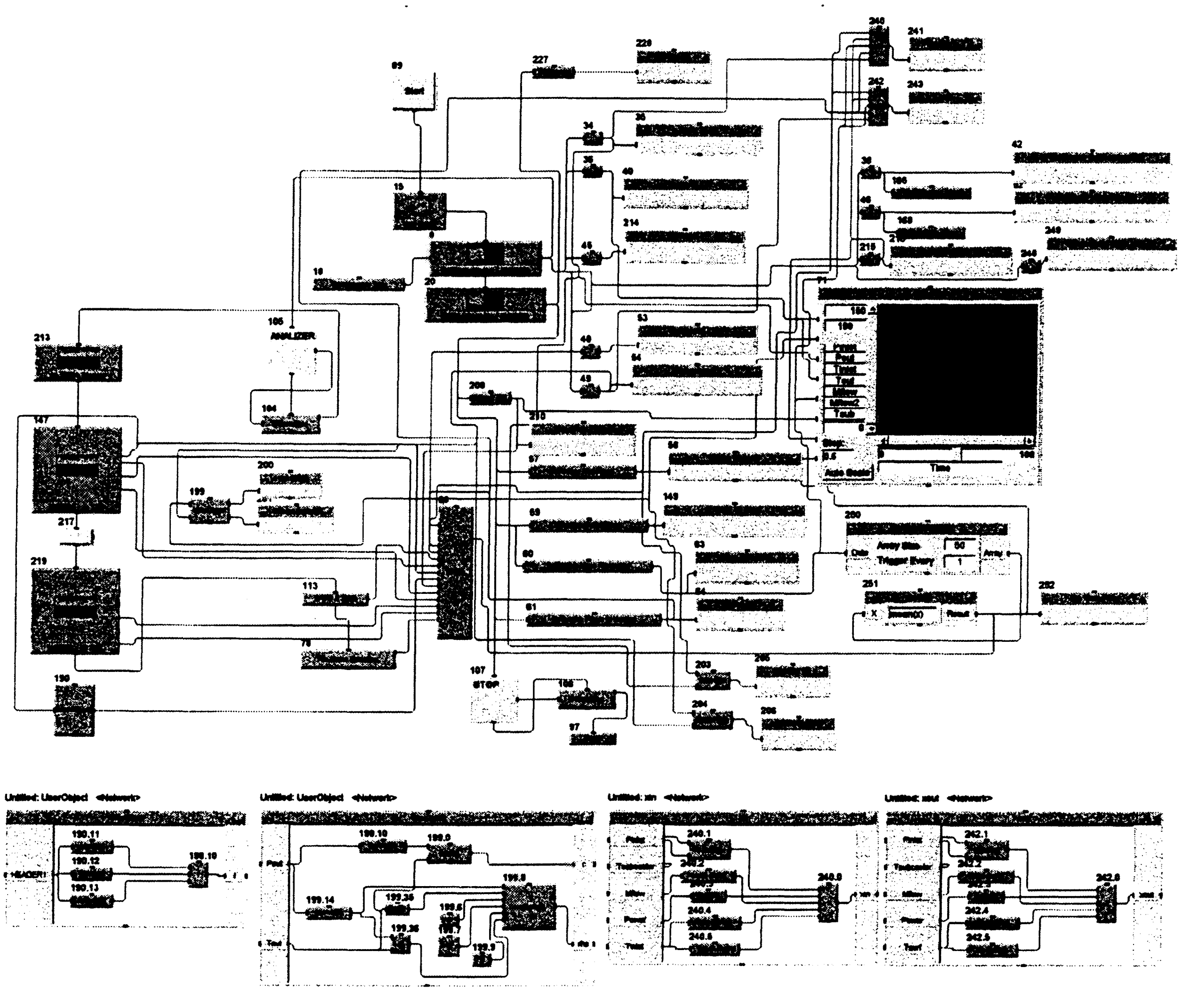

Figure B.5 – *HPVee* code network and user objects

Appendix C

Validation of the Experimental Test Facility

C.1 Attenuation of high frequency reflections

A measurement of internal sound pressure attenuation with distance along the test section shows that the tube coils downstream of the microphone block are very successful at attenuating high frequency sound waves in pure vapor flow. The result is shown in Figure C.1. Note that the measured attenuation is very well predicted by the theoretical visco-thermal attenuation in tubes of that diameter. It is expected that the higher frequency sound waves would be more easily attenuated as the wavelengths are shorter. Although these results are for vapor flow, it is believed that sound waves of all frequencies would be much more significantly attenuated when two-phase flow is present.

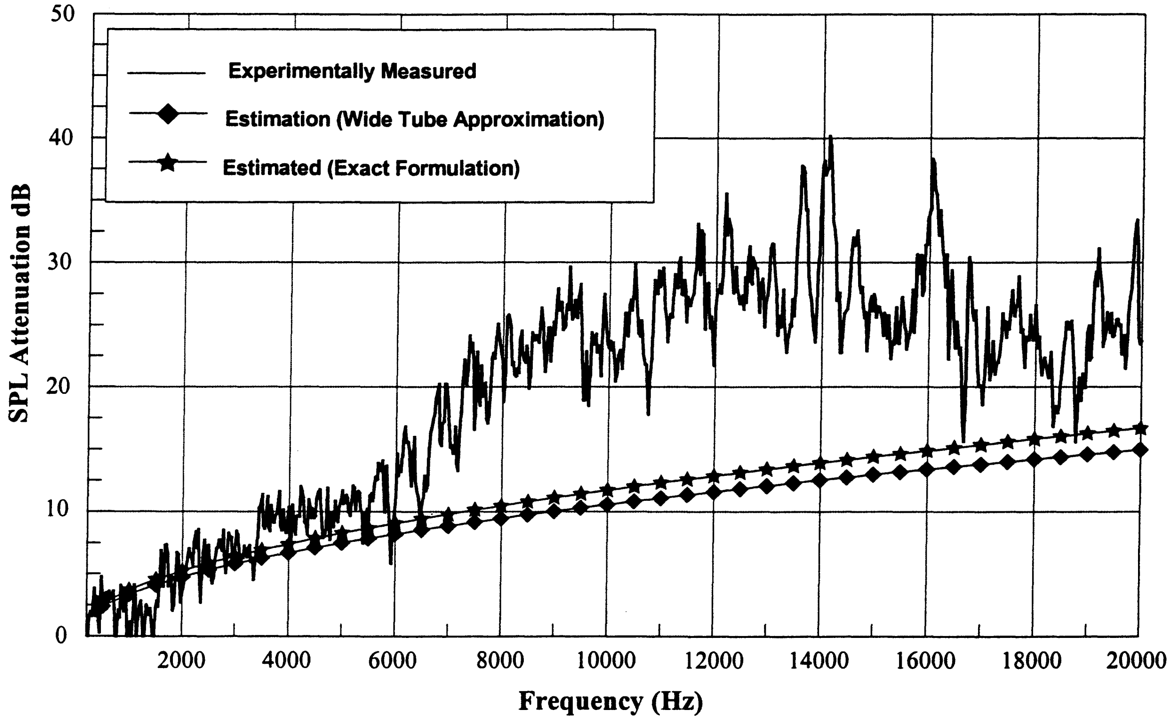

Figure C.1 – Measured and predicted internal sound pressure attenuation in the experimental test facility. From [26]
Orifice tube: 1.71mm I.D., no downstream screen, P=5.78bars, Superheat=13C
Measured between microphone 1 and a temporarily installed microphone after the first tube coil (7.24m)

C.2 Separation of low frequency reflections

Measurements of the reflection coefficient obtained using the two-microphone technique show that low frequency reflections in vapor flow can be mathematically accounted for in all sound pressure measurements. Typical results are shown in Figures C.2 and C.3. Note that the reflected sound waves are only significant below about 800Hz. This makes sense since high frequency reflections (above about 800Hz – see Figure C.1) are naturally attenuated in the system. Results for vapor flow out to the first cut-off frequency are shown in Figure C.4. Note the excellent coherence measurements below the first cut-off frequency. A coherence of one is expected for all frequencies below the first cut-off since only plane waves are present (see Chapter 1). The excellent coherence measurements indicate no burrs or other disturbances are present near the test section. All of the original orifice tube vapor data (see Figure 6.2) is plotted with and without reflections in Figure C.5. The noise data is virtually identical, whether or not reflections are taken into account. The average difference in total internal sound pressure level is only 0.49dB or 0.33%.

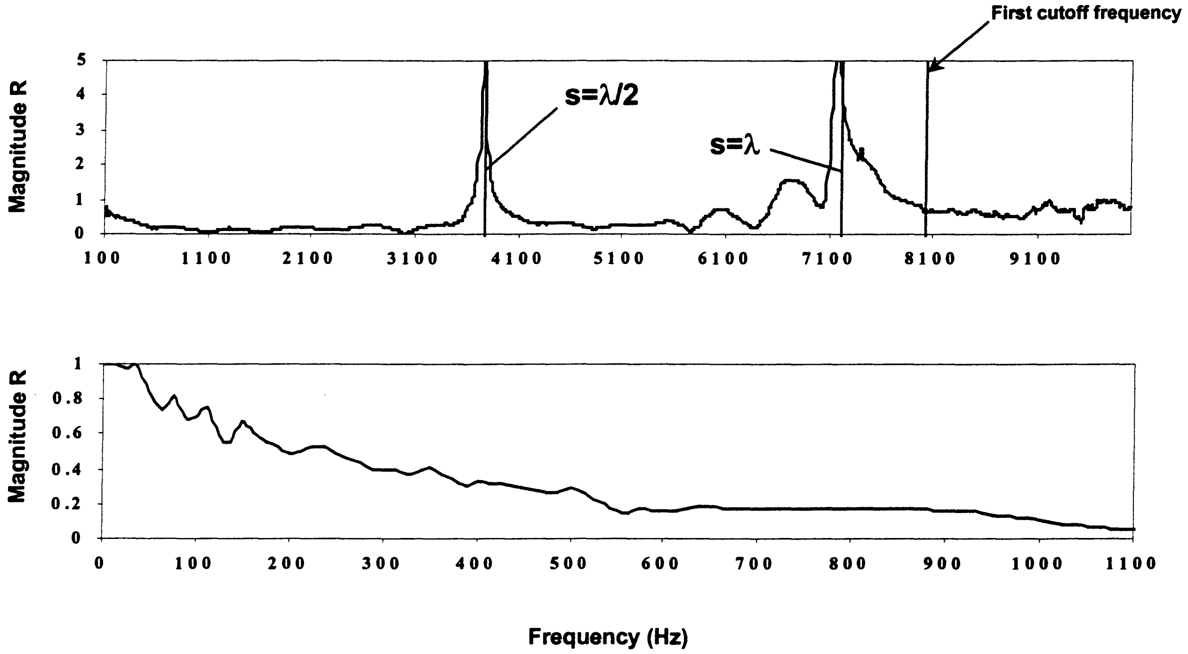

Figure C.2 - Typical reflection coefficient obtained using the two-microphone technique
Orifice tube: 1.71mm I.D. No downstream screen. Vapor flow
S is the microphone spacing and λ is the wavelength in R134a at that frequency

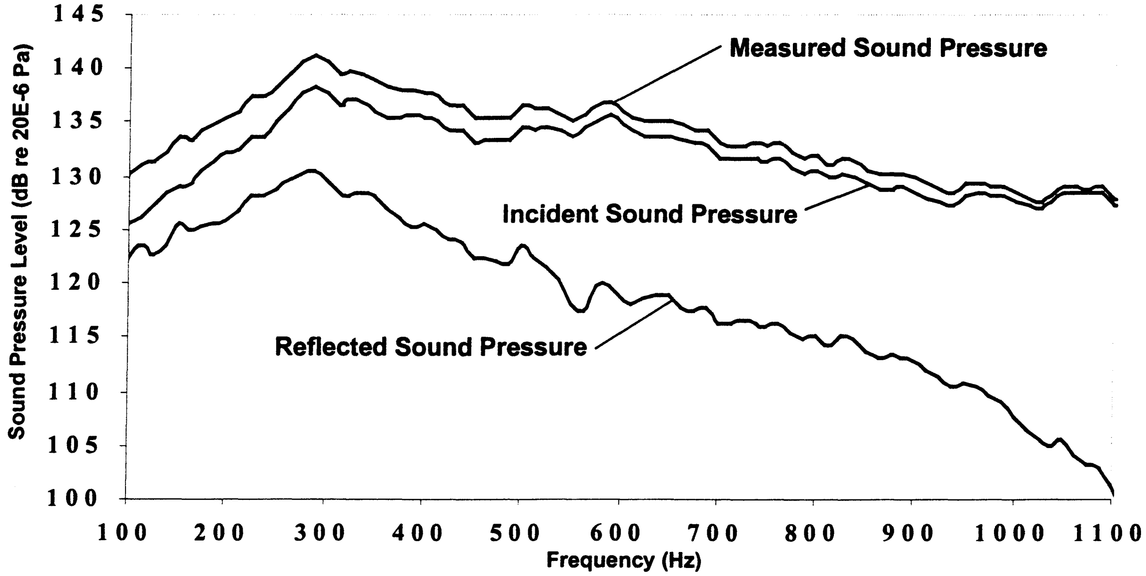

Figure C.3 – Separated sound pressures in the experimental test facility
Orifice tube: 1.71mm I.D., no downstream screen, vapor flow
Measured at microphone 1.

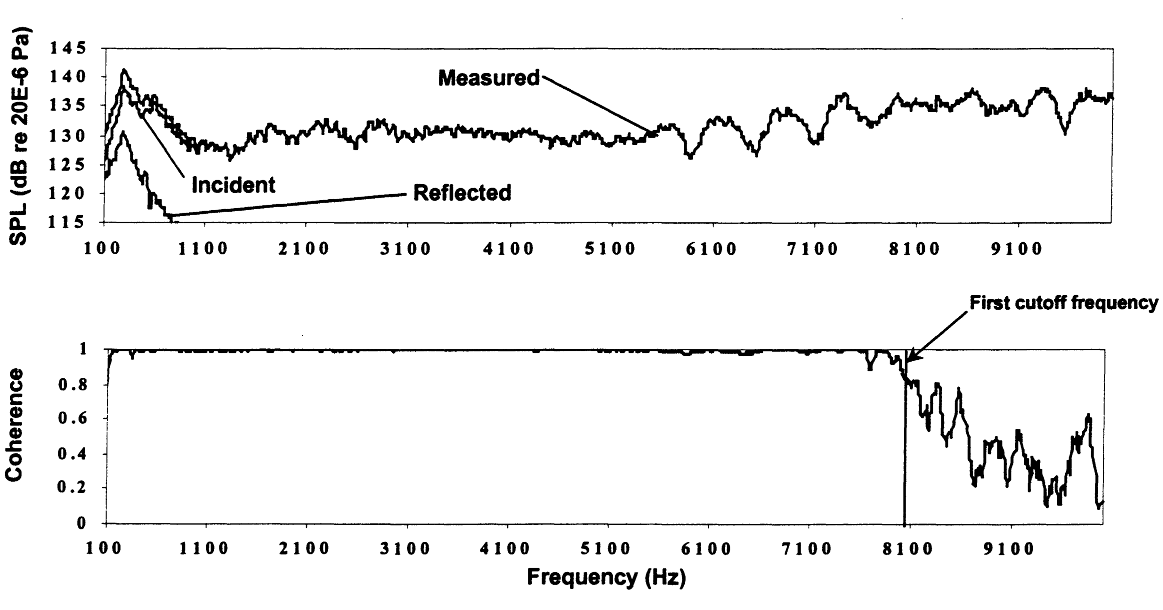

Figure C.4 – Separated sound pressures and coherence in the experimental test facility
Orifice tube: 1.71mm I.D., no downstream screen, vapor flow
Measured at microphone 1.

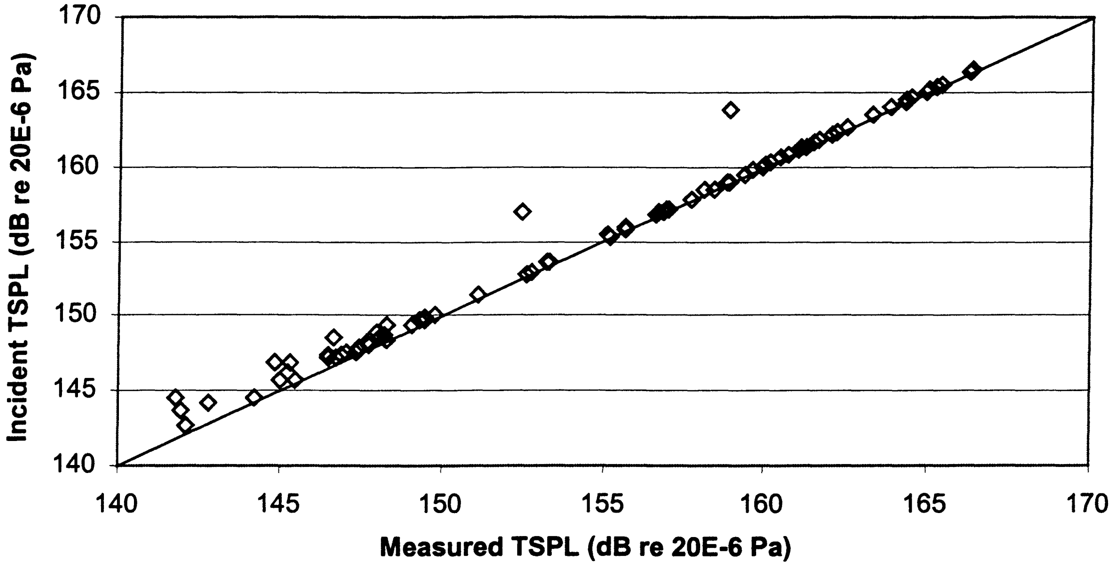

Figure C.5 – Measured vs. incident TSPL in experimental test facility
Orifice tube vapor flow data of Figure 6.2

C.3 Pressure drop along the test section

Measurements of the pressure drop over the entire test section (after expansion) were taken for a variety of vapor flow conditions. A differential pressure transducer was temporarily installed between about 1ft. downstream of the expansion device outlet and the end of the test section. The results are given in Table C.1. Since high mass flows were achieved (very little noise data was ever taken above 100lbm/hr) with vapor densities, the velocities achieved were high and the measured pressure drops are therefore assumed to be worst-case scenario. As these pressure drops are believed to be near the accuracy of the test section low pressure-side transducer, the assumption of negligible pressure drop across the test section (after expansion) is valid.

C.4 Pressure/mass-flow oscillations and steady state assumption

A typical screen capture taken during a capillary tube vapor test is shown in Figure C.6. The steadiness of the lines indicates the effectiveness of the "vapor cushion" and pulsation damper in quelling pressure/mass flow oscillations generated by the pump. Further, the high-pressure side

Table C.1 – Measured pressure drop across test section (after expansion)

Orifice tube: 1.71mm I.D., no downstream screen, vapor flow
Location 1 is upstream, Location 2 is downstream

P1	T1	T2	MF	DP	DP	DP
[bara]	[C]	[C]	[lbm/hr]	[psid]	[bar]	[%]
4.84	94.38	50.97	74.62	5.263	0.361607	7.471229
4.575	64.65	37.61	68.84	5.065	0.348003	7.606632
6.207	49.35	38.21	78.71	4.814	0.330758	5.328787
6.288	83.07	46.15	71.33	4.723	0.324505	5.16071
4.655	50.42	37.41	83.09	5.414	0.371982	7.991027
3.841	87.2	38.72	47.7	4.337	0.297984	7.757989
6.895	72.75	41.25	60.86	4.433	0.30458	4.417408
6.18	97.68	51.68	73.42	4.891	0.336048	5.437675
			Average	*4.8675*	*0.334434*	*6.396432*
			St. dev.	*0.351533*	*0.024153*	*1.347172*

and low-pressure side mass flow meter readings are nearly equal, as expected for steady state operation. For a small number of data points a venturi flow meter was used, as well, and generally gave steady mass flow readings in agreement with the other flow meters. Similar screen captures exist for most of the data points, confirming the assumption of steady state. It is assumed that for data points that may contain more noticeable pressure/mass flow oscillations, the averaging of signals (see Chapter 5) will still yield a valid measurement and the average mass flow can be used.

C.5 Vibration isolation

Measurements of acceleration were taken on the system for a variety of vapor flow conditions through the expansion device. The results show that the vibrations due to system components is small. Additionally, the microphones are very insensitive to acceleration and their measurements are unlikely to be disturbed by surface accelerations. The full description of the vibration isolation measurements and all the results are given in Appendix D for convenience.

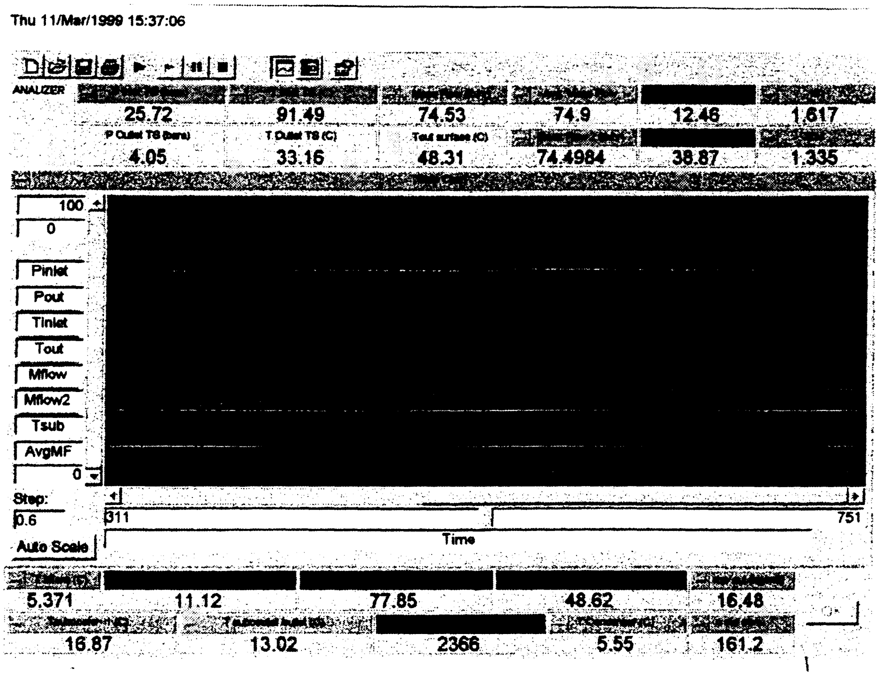

T inlet test section

High pressure mass flow meter,
Low pressure mass flow meter,
Average high pressure mass flow over previous ten seconds

T outlet test section
P inlet test section

T subcooler
P outlet test section

Figure C.5 – *HPVee* screen capture

Capillary tube: 1.626mm I.D., 32in length, 5deg outlet cone, vapor flow

Appendix D

Vibration Isolation Experiments

As mentioned in the description of the experimental test facility (Chapter 2), the system uses a pulsation damper and a "vapor cushion" to isolate the test section from pressure/mass flow pulsations generated by the pump *within the refrigerant flow*. Mechanical vibrations, however, resulting from the mechanical action of a system component and/or the pump-generated pulsations in the refrigerant, may still be transmitted to the test section through solid contact. These vibrations could potentially affect sound pressure and/or acceleration measurements in the test section. As such, these vibrations must be minimized or accounted for.

In an attempt to isolate the test section from vibrations generated anywhere else in the system, three separate actions were taken:

1. The pump, originally bolted to the floor, was instead mounted on a vibration isolator (see Figure 2.6).
2. Part of the section of tubing following the pump but before the first heater (see Figure 2.1) which originally rested on the structure and often vibrated in response to pump operation, was hung from the ceiling with flexible rubber supports so as to no longer rest on the structure at any point.
3. The rigid supports which supported the test section from the structure were replaced by vibration isolators (see Figure 2.3).

The pump, the liquid line, and the test section are still connected to the rest of the system through piping connections, so the steps taken cannot completely eliminate all transmitted vibrations.

Measurements were taken to try to evaluate the effectiveness of the various vibration isolation actions discussed above. The set-up was as follows: A pipe section was constructed with two attached solid brass blocks, each of the blocks with a threaded hole to mount an accelerometer, as shown in Figure D.1.

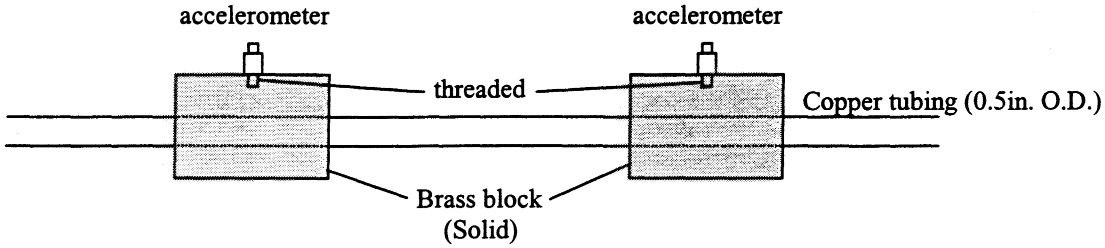

Figure D.1 - Accelerometer mounting for vibration isolation tests

The pipe section was inserted into the test facility immediately following the microphone block with compression fittings. Acceleration measurements were taken over a wide range of vapor flow conditions and at various locations around the experimental test facility. The test matrix is given in Table D.1 and the results are shown in Figure D.2.

Table D.1 – Test matrix for vibration isolation experiments
W/weight mean small weight was hung from block

Test	Block	Center Frequency	Pin [bara]	Pout [bara]	Mass flow [lbm/hr]	Tin [C]	Tout [C]	Condition
Geo111	block1	10kHz	10.7	7.92	250	42.1	30.5	After (1) only
Geo112	block2	10kHz	10.7	7.92	250	42.1	30.5	After (1) only
Geo121	block1	1kHz	10.7	7.92	250	42.1	30.5	After (1) only
Geo122	block2	1kHz	10.7	7.92	250	42.1	30.5	After (1) only
Geo211	pump	1kHz	10.7	7.92	250	42.1	30.5	After (1) only
Geo221	pump	1kHz	10.7	7.92	250	42.1	30.5	After (1) only
Geo131	block2	1kHz	9.1	6.4	54	36.6	27.9	After (1), (2), (3)
Geo132	block1	1kHz	9.1	6.4	54	36.6	27.9	After (1), (2), (3)
Geo141	block2	1kHz	9.1	6.4	54	36.6	27.9	After (1), (2), (3)
Geo142	block1	1kHz	9.1	6.4	54	36.6	27.9	After (1), (2), (3)
Geo151	block1	1kHz	10.7	6.3	128	41	22	After (1), (2), (3)
Geo251	block2	1kHz	10.7	6.3	128	41	22	After (1), (2), (3)
Geo152	block1w/weight	1kHz	10.7	6.3	128	41	22	After (1), (2), (3)
Geo252	block2w/weight	1kHz	10.7	6.3	128	41	22	After (1), (2), (3)
Geo16	block1	1kHz	13.5	6.8	90	52	35	After (1), (2), (3)
Geo26	block2	1kHz	13.5	6.8	90	52	35	After (1), (2), (3)
Geo17	block1	1kHz	13.6	6.6	85	101	70	After (1), (2), (3)
Geo27	block2	1kHz	13.6	6.6	85	101	70	After (1), (2), (3)

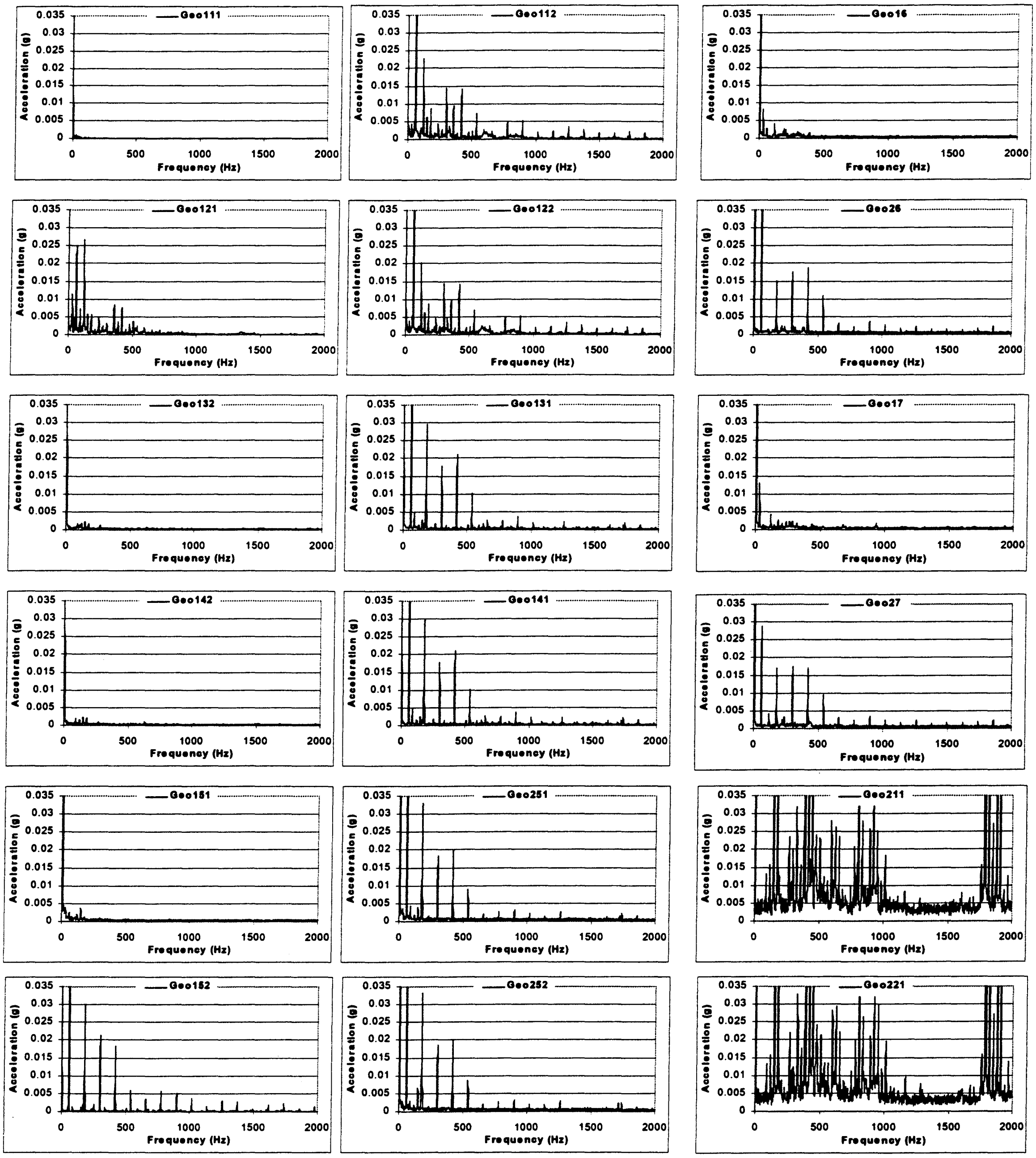

Figure D.3 – All vibration isolation test results

The results show that surface accelerations over the audible frequency range caused by system components are generally small everywhere, especially in the test section, compared to the surface acceleration generated by the expansion devices in vapor flow (see Chapter 6).

Appendix E

R134a Thermophysical Property Curve Fits

E.1 Purpose

In order to easily and quickly compute various thermophysical properties of R134a in *HPVee* codes, *EXCEL* worksheets, or various other programs without the use of a lookup table or complicated pre-existing curve-fits, it was desirable to construct polynomial curve-fits of some useful thermophysical properties over pressure and temperature ranges of interest. The properties selected were: Saturation temperature, liquid density, vapor density, vapor enthalpy, saturated liquid-vapor enthalpy (hlg), and vapor speed of sound.

E.2 Curve fits and methodologies

All curve fits were done using the *EES* plot-curve fit or linear regression functions and all fits were to either the *EES* generated property values or, in the case of speed of sound, to the definition of the property, and agree very closely with the 1997 *ASHRAE Fundamentals* [32] values in spot checks.

E.2.1 Saturation temperature

Saturation temperature is a function of pressure only. The saturation temperature curve fit was generated simply by fitting a polynomial in pressure to the *EES*-generated saturation temperatures over a range of pressures using the *EES* plot-curve fit function. The curve fit, range, and R-value are given in Table E.1. The *EES* code is given below and the property plot (with curve fit) are given in Figure E.1.

```
Tsat=Temperature(R134a,P=Pbar,x=0.5)  "C"
Pbar=PsatConvert(psia,bar)  "bara"
```

(Unit settings: bar,C)

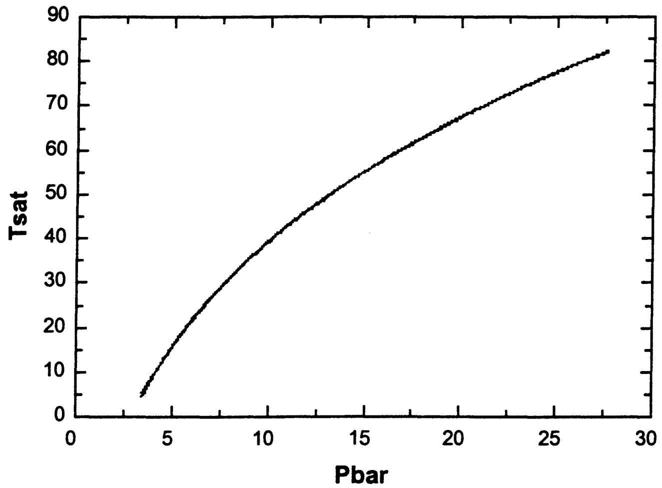

Figure E.1 – Tsat plot and curve fit.
The two curves lay indistinguishably on top each other.

E.2.2 Liquid density

Although the density of liquid refrigerant is a function of pressure and temperature, liquid R134a can be assumed incompressible and the liquid density can then be considered a function of temperature only. The liquid density curve fit was generated by fitting a polynomial in temperature to the *EES*-generated liquid density over a range of temperatures using the *EES* plot-curve fit function. Since *EES* requires a temperature and pressure to be specified to compute density, the pressure was given as 0.1% above the saturation pressure at each specified temperature. The *EES*-generated densities were also computed for a pressure 10 times the saturation pressure at each specified temperature and the curve was virtually identical (validating the incompressible assumption). The curve fit, range, and R-value are given in Table E.1. The EES code is given below and both property plots (with curve fit) are given in Figure E.2.

```
P=Pressure(R134a,T=T,x=0.5) "bara"
rho=Density(R134a,T=T,P=(P+.001P)) "kg/m3"
rho_10=Density(R134a, T=T, P=10P) "kg/m3"
```

(Unit settings: bar,C)

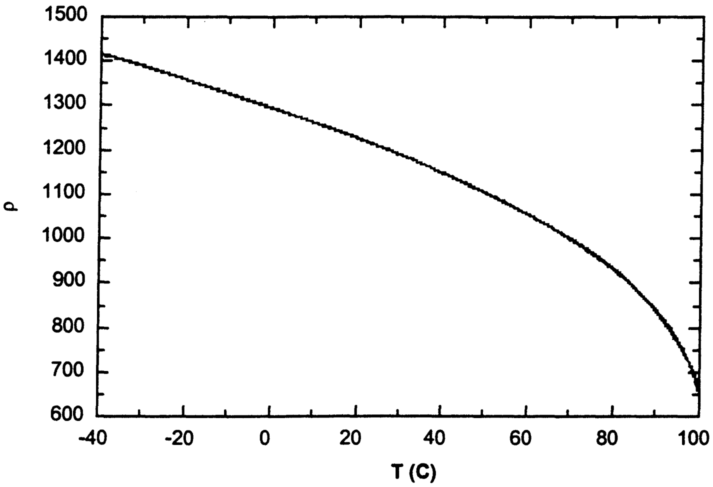

Figure E.2 – Liquid density plots and curve fit.
The three curves lay indistinguishably on top each other.

E.2.3 Vapor density

The vapor density curve fit was generated as follows: The Modified Redlich-Kwong equation of state for real gases [29,30] was solved explicitly for specific volume symbolically in *Mathematica*. The Modified Redlich-Kwong equation of state is:

$$P = \frac{RT}{v-b} - \frac{a/T^{0.5}}{v(v-b)} \tag{E.1}$$

where R is the specific ideal gas constant, P is the pressure, T is the absolute temperature, v is the specific volume, and a and b are empirical constants given as:

$$a = 0.42747\frac{R^2T_c^2}{P_c} \tag{E.2a}$$

$$b = 0.08664\frac{RT_c}{P_c} \tag{E.2b}$$

with P_c and T_c being the critical temperature and pressure of the gas.

The Mathematica code was as follows:

```
systemeq[v]=(RT)/(v-b)-a/(T^.5v(v-b))-P
Solve[systemeq[v]= =0,v]
```

The (2) solution(s) were:

$$v=\frac{0.5\left[\sqrt{T}(bP+RT)+\sqrt{-4aP\sqrt{T}+T(bP+RT)^2}\right]}{P\sqrt{T}} \tag{E.3a}$$

$$v=\frac{0.5\left[\sqrt{T}(bP+RT)-\sqrt{-4aP\sqrt{T}+T(bP+RT)^2}\right]}{P\sqrt{T}} \tag{E.3b}$$

where the positive root, Equation (E.3a), is taken as the desired solution.

The invert of that equation, which is density, was then entered into *EES* and used to compute density at every pressure and temperature with a specified range. An *EES*-generated density was also computed at each pressure and temperature and a polynomial curve fit of the ratio of the *EES* density over the Modified Redlich-Kwong density was generated using the *EES* linear regression function. The *EES* code was:

```
"Critical contants"
Tc=374.205 "K"
Pc=4067 "kPa"

"Specific ideal gas constant"
Ru=8.3144 "kJ/kg-K"
R=Ru/Mm
Mm=MOLARMASS(R134a) "kg/kmol"
```

```
"Redlich-Kwong density"
a=.42747R^2Tc^2.5/Pc
b=.08664RTc/Pc
rho_pred=((0.5(sqrt(T)(bP+RT)+sqrt(abs(4aPsqrt(T)+T(bP+RT)^2))))
         /(Psqrt(T)))^(-1) "kg/m3"

"EES density"
rho=Density(R134a,P=P,T=T) "kg/m3"

"Ratio"
z=rho/rho_pred
```
(Unit settings: kPa,K)

The curve-fit of z was:

z=1.020347+6.631567e-5Pk+6.123958e-8Pk^2-6.000715e-11Pk^3-1.538837e3T
+2.327045e-5T^2-2.645475e-8T^3-2.201042e-7PkT-2.714122e8PkT^2
+2.783377e-10Pk^2T+1.173178e-11Pk^2T^2 (E.4)

The actual density curve fit is then the invert of the Modified Redlich-Kwong equation solved for density (invert of Equation (E.3a)) multiplied by Equation (E.4). The density curve fit, range, and R-value are given in Table E.1 and the *EES*-generated density is plotted against the density predicted by the curve fit in Figure E.3.

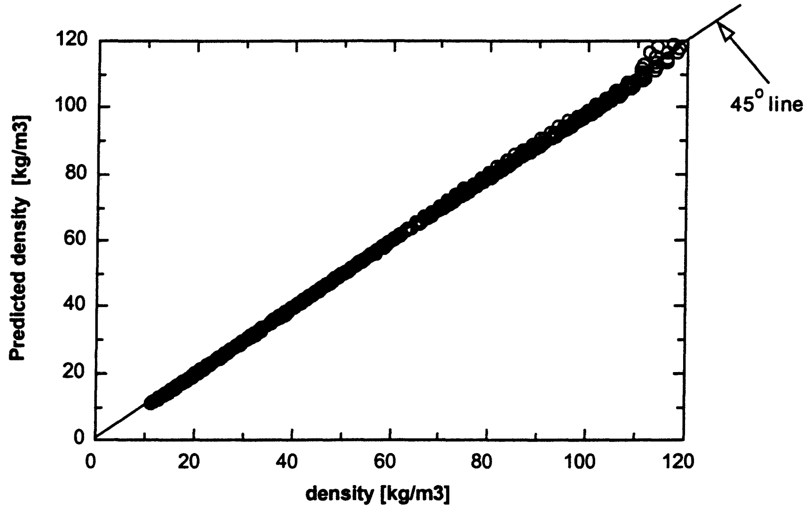

Figure E.3 – Vapor density predictions vs. *EES*-generated values

E.2.4 Vapor enthalpy and hlg

Vapor enthalpy in refrigerant is a function of pressure and temperature, while hlg, being a saturated property, in a function of pressure *or* temperature. Both were assumed to be functions of temperature only in constructing their curve fits. The curve fits were then generated by fitting polynomials in temperature to the *EES*-generated enthalpies over a range of temperatures using the *EES* plot-curve fit function. Since *EES* requires a temperature and pressure to be specified to compute vapor enthalpy for refrigerant, the pressure was given as 0.1% above the saturation pressure at each specified temperature. The *EES*-generated vapor enthalpies were also computed for a pressure 6 times the saturation pressure at each specified temperature and the curve was virtually identical. The curve fit, range, and R-value are given in Table E.1. The *EES* code is given below and both property plots (with curve fit) are given in Figure E.4.

```
P=Pressure(R134a,T=T,x=0.5) "bara"
h=Enthalpy(R134a,T=T,P=(P+.001P)) "kJ/kg"
h2=Enthalpy(R134a,T=T,P=(P+5P)) "kJ/kg"
hl=Enthalpy(R134a,T=T,x=0) "kJ/kg"
hg=Enthalpy(R134a,T=T,x=1) "kJ/kg"
hlg=hg-hl "kJ/kg"
```

(Unit settings: bar, C)

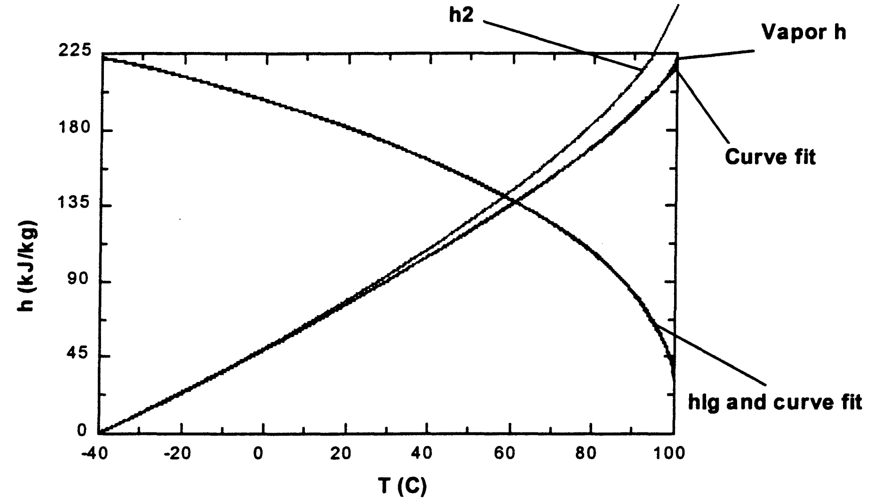

Figure E.4 – Enthalpy predictions vs. *EES*-generated values

E.2.5 Vapor speed of sound

The vapor speed of sound of a refrigerant is a function of temperature and pressure. The definition of speed of sound is:

$$c=\left.\frac{\partial P}{\partial \rho}\right)_s \tag{E.5}$$

where P is the pressure, ρ is the density, and s is the entropy of the substance.

The curve fit was generated by calculating speed of sound by a finite-difference approximation of Equation (E.5) in *EES* over a range of pressures and temperatures and fitting a polynomial to those values using the *EES* linear regression function. The curve fit, range, and R-value is given in Table E.1. The *EES* code is given below and a property plot (including curve fit) is given in Figure E.5.

```
s=Entropy(R134a,P=P1,T=T1) "kJ/kg-K"
rho_1=Density(R134a,P=P1,s=s) "kg/m3"
rho_2=Density(R134a,P=P2,s=s) "kg/m3"
d_P=0.000001P1 "kPa"
P2=P1+d_P "kPa"
d_rho=abs(rho_1-rho_2) "kg/m3"
c=sqrt(d_P1000/d_rho) "m/s"
```

(Unit settings: kPa,C)

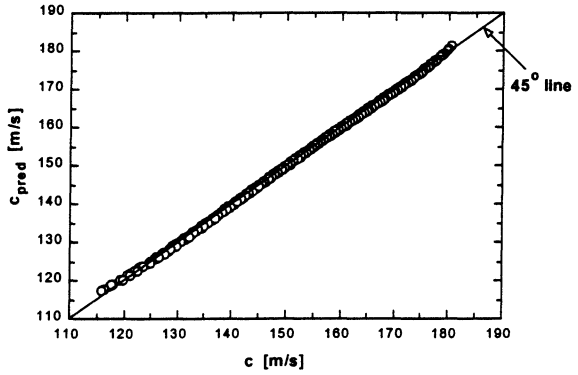

Figure E.6 – Vapor speed of sound predictions vs. definition-generated values

Table E.1 – Thermophysical property curve-fits for R-134a
The last column is the number of points used to make the curve fit

Property	Ind. variables	Curve fit	R^2 value	Range	No. points
Sat. temp.	P [bara]	$Tsat = -24.53390 + 10.29703P - 0.5354664P^2$ $+ 0.01667852P^3 - 0.00020758P^4$	99.99%	P: 50 - 400psia	1000
Liquid density	T [C]	$\rho_L = 1296.401 - 3.4179T - 0.011045T^2 + 0.000040823T^3 +$ $0.0000012345T^4 - 0.000000014386T^5 - 1.8081E\text{-}10T^6$	99.98%	T: (-40) - 100C	1000
Vapor density	P [kPa] T [K]	$\rho_v = Z\dfrac{2P\sqrt{T}}{(bP+RT)\sqrt{T}+\sqrt{\lvert -4aP\sqrt{T}+T(bP+RT)^2\rvert}}$ where Z is given by Equation (&.4) a,b are given by Equations (&.2a,b) R is the ideal gas constant	~97%	P: 50 - 400psia T: Sat. - 110C	921
Vapor enthalpy	T [C]	$h_v = 49.30567 + 1.351244T + 0.00153503T^2$ $- 0.000032219T^3 + 4.9110E\text{-}07T^4$	99.99%	T: (-40) - 100C	1000
hlg	T [C]	$hlg = 197.1772 - 0.71352T - 0.0016744T^2 - 0.000090834T^3 -$ $5.9096E\text{-}07T^4 + 4.2306E\text{-}08T^5 - 3.4272E\text{-}10T^6$	99.87%	T: (-40) - 100C	1000
Vapor speed of sound	P [psia] T [C]	$c = 156.0529 - 0.20382P - 0.00077382P^2$ $- 2.7831E\text{-}07P^3 + 0.3115039T - 0.0015711T^2$ $+ 0.000012091T^3 + 0.00284098PT$ $- 0.000019431PT^2 + 0.000011391P^2T - 2.6286E\text{-}08P^2T^2$	~98%	P: 50 - 400psia T: Sat. - 110C	921

E.3 Note on high order terms

Several of the polynomial curve fits contain high order terms with coefficients << 1. These terms could certainly be neglected with little loss in accuracy over the pressure and temperature ranges specified, greatly simplifying some of the curve fits. However, these terms were included when generating the curve fits in order to fully capture the property values over their entire ranges, with very high accuracy, including at the range edges. Since polynomials of any order are easily evaluated by any computer, the highest order terms were kept to ensure highest accuracy for all pressure and temperatures within the specified ranges.

Appendix F

Microphone Calibration

As discussed in Chapter 3, in order to implement the two-microphone technique, the "sensor-switching" technique must be employed to calibrate the gain and phase response of the microphones being used. Since the sensor-switching technique requires removing the microphone section from the system during operation, it becomes very difficult to accurately calibrate the microphones with refrigerant.

One possibility for calibrating the microphones for our measurements was to use Nitrogen in a special Nitrogen test facility (shown in Figure F.1). By using Nitrogen, the microphone section could be easily removed and switched without changing the inlet conditions to the expansion device. Note that a third microphone was installed in the microphone block when used in the Nitrogen loop.

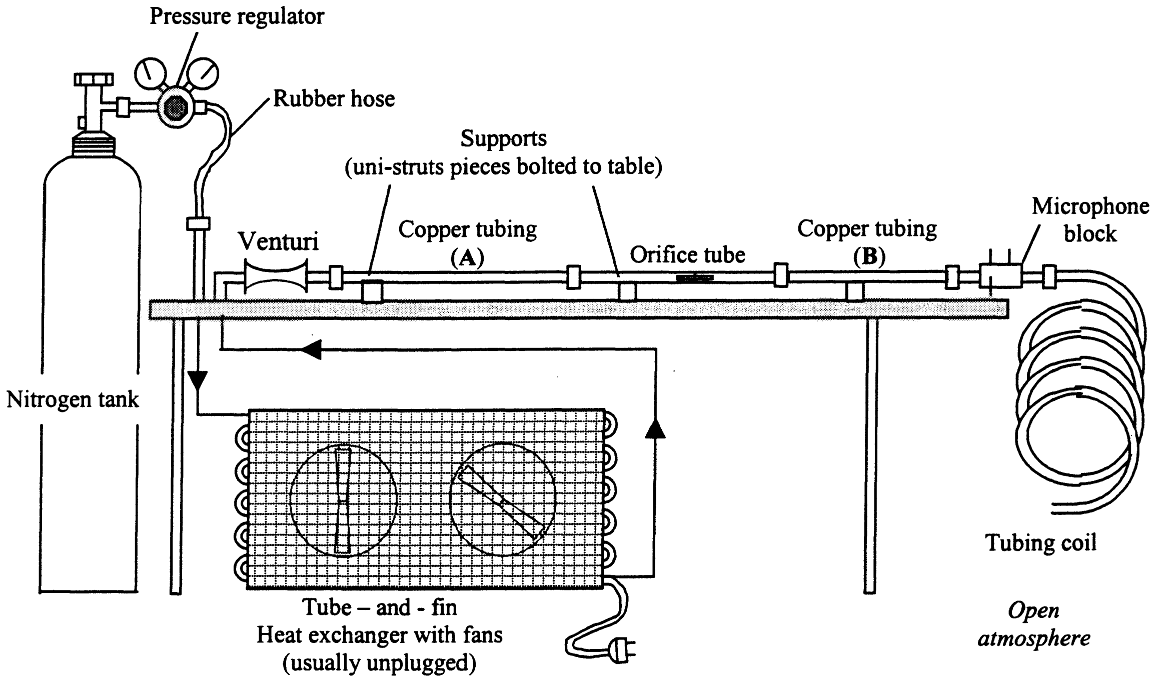

Figure F.1 - Nitrogen Test Facility

One preliminary and one final set of data were taken for the largest orifice tube (1.71mm nominal I.D.). Typical results from the final set are shown in Figure F.2.

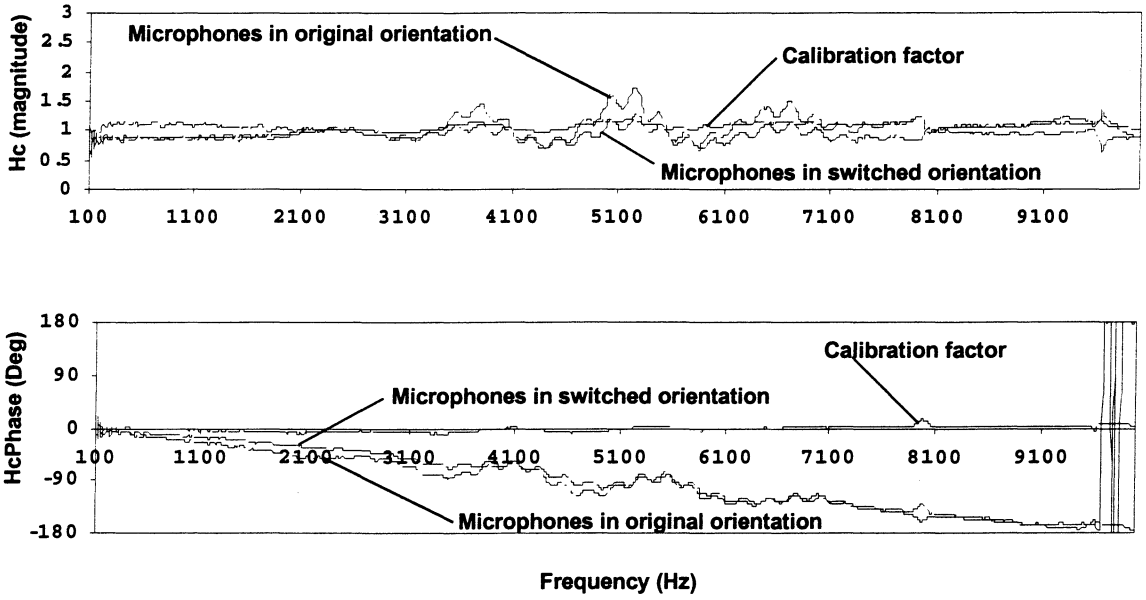

Figure F.2 - Typical results of the sensor-switching technique in Nitrogen.
Hc is the calibration factor as given by Equation (3.12)

Full results from the final data set are shown in Figure F.3. Note that the calibration factor (Hc) magnitude is nearly unity over the measured frequency range. This is expected since the microphones are assumed well made and well calibrated from the manufacturer. Note also that the phase of the calibration factor is 0 deg over the measured frequency range. This is also expected as, again, the microphones are assumed well calibrated from the manufacturer.

Finally, in order to check that the calibration in Nitrogen would be valid in refrigerant, it was necessary to check how the radiation mass might change the natural frequency of the microphone diaphragm in both fluids. Since the absolute natural frequency of the microphone diaphragm is so high (250 kHz), the natural frequency was virtually unchanged in either fluid and so the calibration in Nitrogen is presumed valid in refrigerant. A definition of radiation mass and the full equations and computations are given in Appendix G.

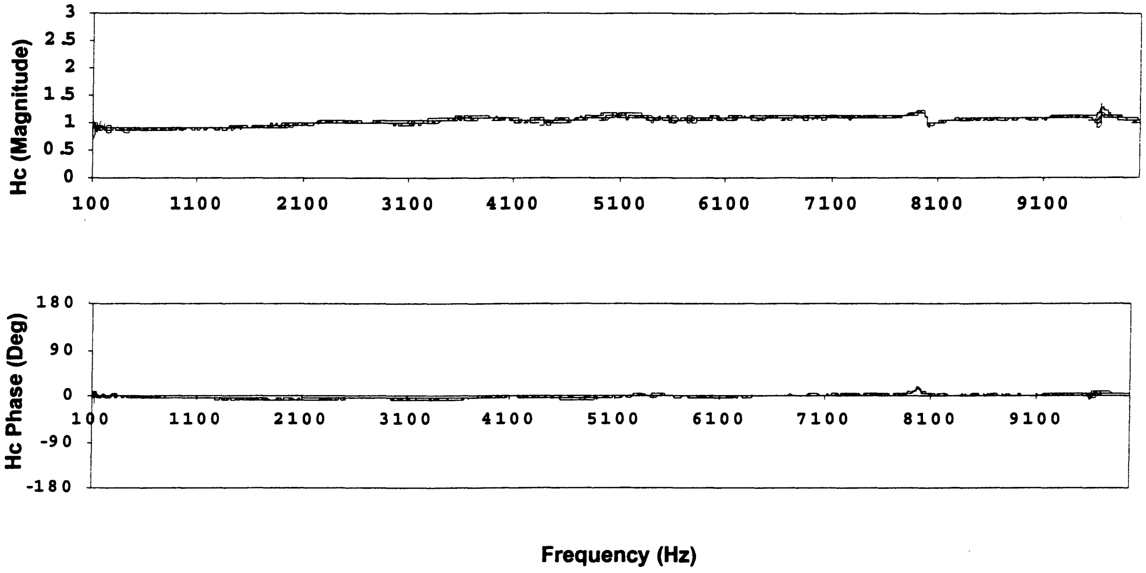

Figure F.3 - Full results of the microphone calibration in Nitrogen
Orifice tube: 1.71mm I.D. No downstream screen

A secondary and unexpected result from the calibration tests in Nitrogen came from the results of the coherence measurements. For each of the Nitrogen tests, coherence measurements were taken between each pair of microphones. Since attenuation between the microphones is assumed negligible (an assumption of the Two-microphone technique – see Chapter 3), one would expect near-perfect coherence between each pair of microphones at frequencies below the first cut-off. Typical results are shown in Figure F.4. Note that the coherence is excellent between microphones 2 and 3, but somewhat disturbed between microphones 1 and 2 and between microphones 1 and 3. It is believed that small flow disturbances in the wake of the first microphone may be locally interfering with sound pressure measurements between microphone 1 and the other two microphones.

Notes

Although not shown in Figure F.1, the Nitrogen loop also contains a type-T thermocouple installed just upstream of copper pipe (A). The Nitrogen loop data-acquisition set-up is as described for the refrigerant loop in Appendix B with a modified version of the *HPVee* code.

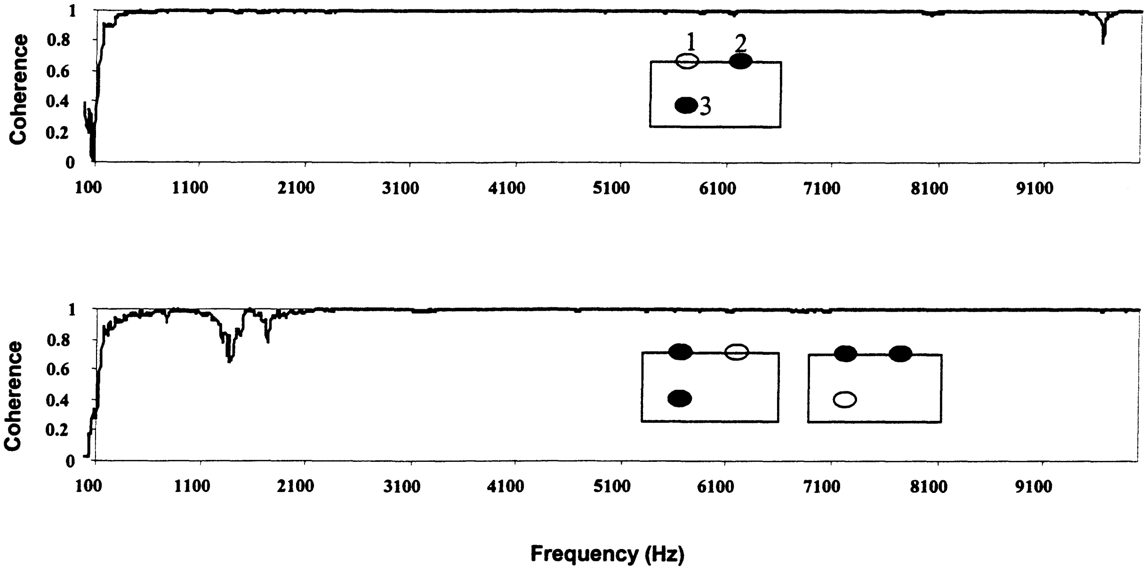

Figure F.4 - Typical results of coherence measurements in Nitrogen.
Orifice tube: 1.71mm, No downstream screen

Table F.1 – Preliminary test matrix for microphone calibration tests in Nitrogen
Orifice tube: 1.71mm I.D., No downstream screen

Test	Pin	Venturi Pin	Tinlet	mdot	M
	[inH20]	[psig]	[C]	[lbm/hr]	
1	1.33	163.30	24.03	49.49	0.1912
2	1.33	163.30	21.96	49.76	0.1916
3	1.08	149.36	21.66	43.12	0.1659
4	0.82	109.80	22.52	32.56	0.1253
5	0.54	71.76	22.35	22.05	0.08477
6	0.24	25.23	22.58	10.04	0.03858
7	1.50	166.12	21.94	53.21	0.2049
8	1.17	159.43	21.55	46.28	0.178
9	0.93	128.85	21.39	37.44	0.1439
10	0.68	90.68	22.28	27.37	0.1053
11	0.68	91.57	22.21	27.5	0.1058
12	0.29	34.68	22.34	12.26	0.04709

Table F.2 – Final test matrix for microphone calibration tests in Nitrogen

Orifice tube: 1.71mm I.D., No downstream screen

Test	Pin	Venturi Pin	Tinlet	mdot	M
	[inH20]	[psig]	[C]	[lbm/hr]	
1	1.46	165.80	21.81	52.55	0.2023
2	1.48	165.87	20.98	52.98	0.2037
3	0.73	99.64	21.34	29.55	0.1135
4	0.74	99.70	22.54	29.73	0.1144
5	0.23	25.56	22.15	9.841	0.03779
6	0.36	43.99	23.16	14.76	0.05679
7	0.36	44.05	22.88	14.79	0.05689
8	0.16	15.35	22.81	7.001	0.02691

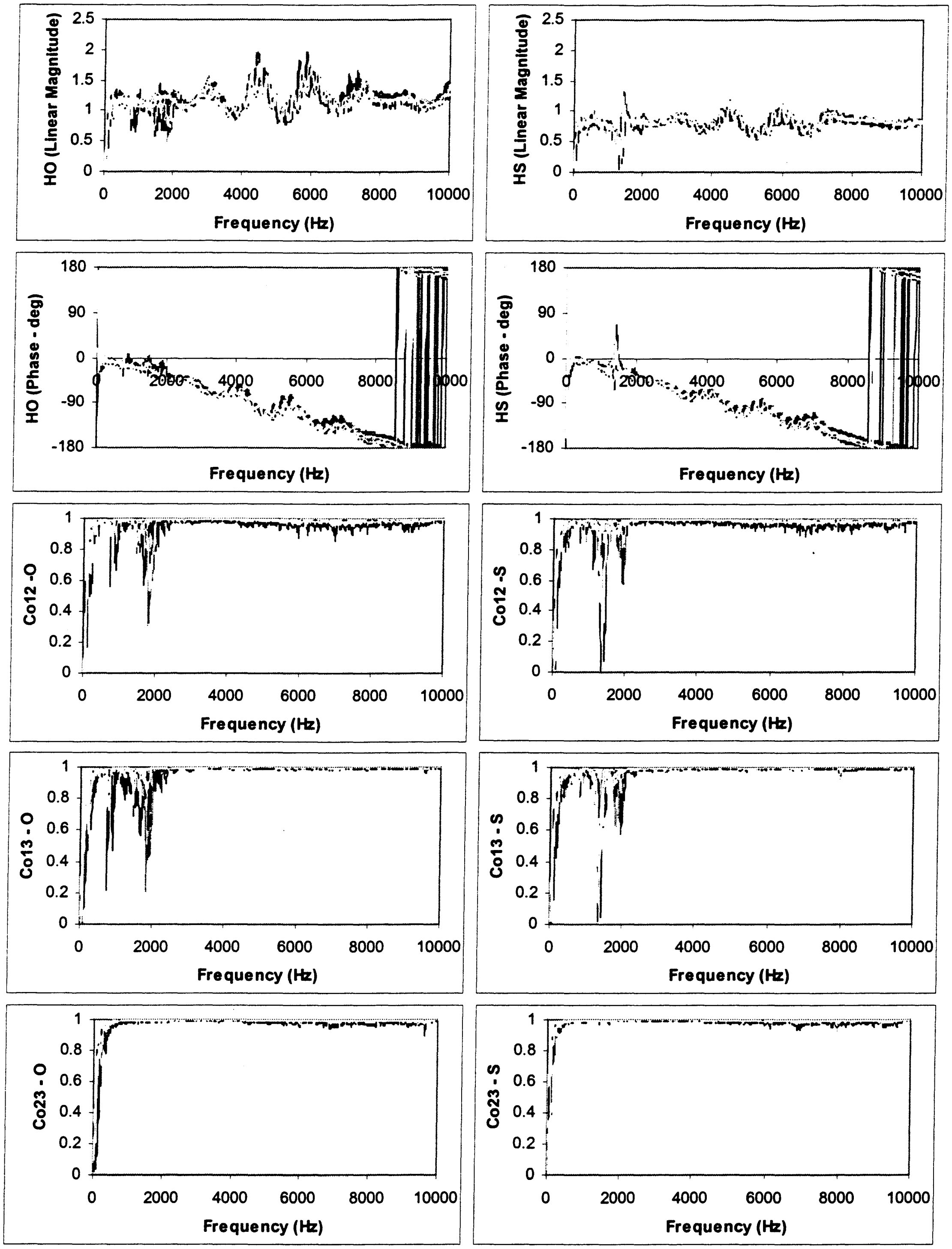

Figure F.5 – Preliminary test results for microphone calibration tests in Nitrogen

Orifice tube: 1.71mm I.D., No downstream screen

“O” means microphones in original orientation, “S” means after switching

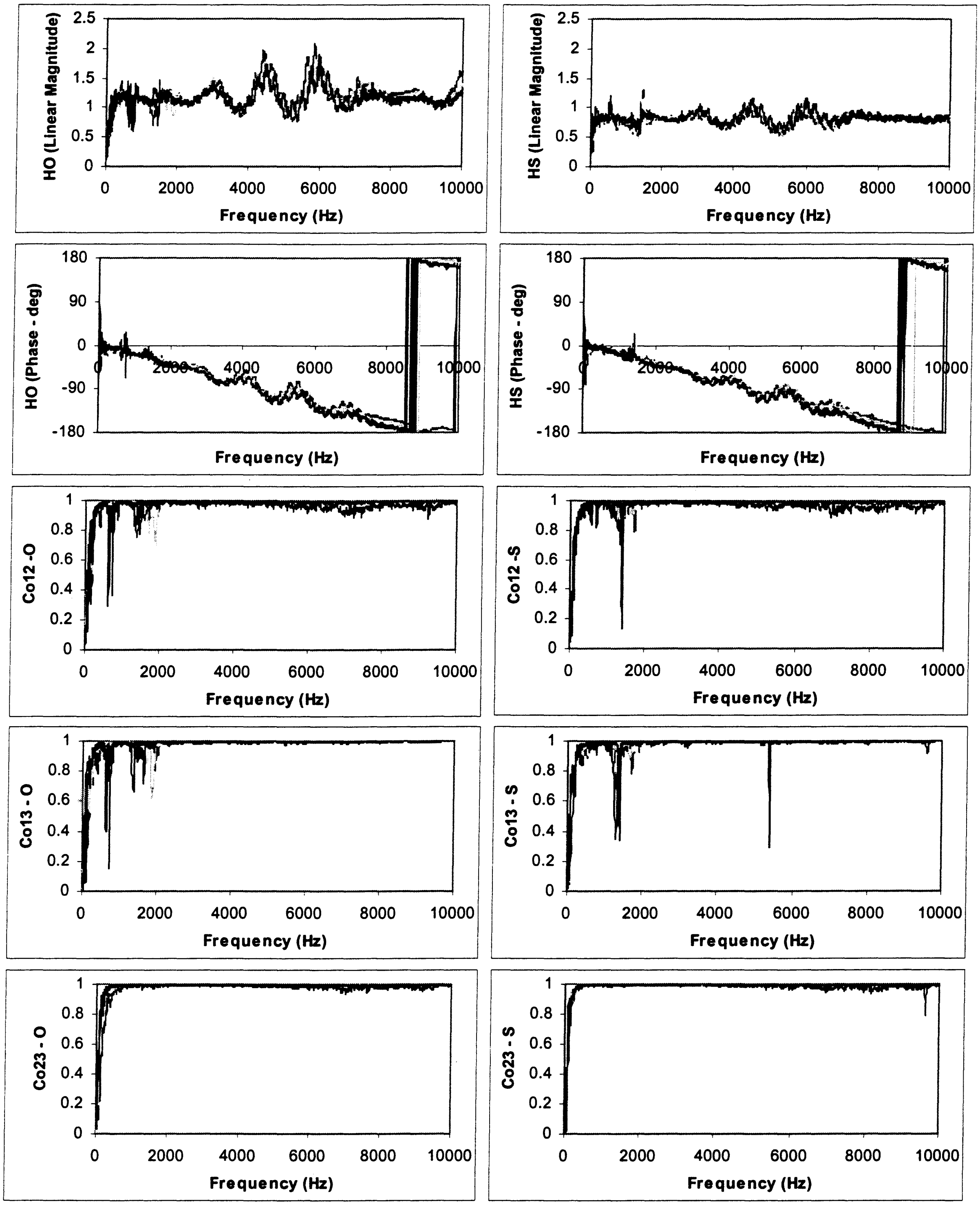

Figure F.6 – Final test results for microphone calibration tests in Nitrogen
Orifice tube: 1.71mm I.D., No downstream screen
"O" means microphones in original orientation, "S" means switched

Appendix G

Radiation Mass

G.1 Definition and equations

When a piston oscillates in a fluid, there is a mass loading increase resulting from oscillation in the medium. In other words, it's as if some of the fluid "sticks" to the piston and causes the effective mass of the piston to increase. Since the mass of the piston is effectively increasing, there may be a marked decrease in the resonant frequency of the oscillator.

$$\omega_o = \sqrt{s/m} \qquad \text{Natural frequency of oscillator} \tag{G.1}$$

$$\omega_o^{'} = \sqrt{s/(m + m_r)} \qquad \text{Natural frequency when oscillating in a fluid} \tag{G.2}$$

$$m_r = X_r / 2\pi f \qquad \text{Radiation mass} \tag{G.3}$$

$$X_r = 4a^2 \rho c \left[\frac{4\pi f a}{3c} - \frac{(4\pi f a)^3}{3^2 \cdot 5c^3} + \frac{(4\pi f a)^5}{3^2 \cdot 5^2 \cdot 7c^5} \right] \qquad \text{Radiation reactance} \tag{G.4}$$

G.2 Results

As described in Appendix F, in order to validate the microphone calibration in Nitrogen for use in refrigerant, the natural frequency of the microphones in both fluids must be nearly equal over the frequency range of interest.

The microphones are assumed to behave as a simple oscillating piston with an absolute natural frequency of 250,000Hz (as given by the manufacturer). The EES code is given below and the results are given in Table G.1 and Figure G.1

```
"Constants"
a=.05convert(in,m) "m"
omega_0=250000 "Hz"
m=0.0015 "kg"
omega_0=sqrt(s/m)

"Nitrogen"
X_1n=(4/pi)(x_n/3-x_n^3/45+x_n^5/1575)
X_rn=pia^2rho_nc_nX_1n
x_n=2k_na
k_n=2pif/c_n
c_n=350
rho_n=Density(Nitrogen,T=21,P=140convert(psi,kPa))
m_rn=X_rn/omega_n
k_n=omega_n/c_n
omega_1n=sqrt(s/(m+m_rn))

"Refrigerant"
X_1r=(4/pi)(x_r/3-x_r^3/45+x_r^5/1575)
X_rr=pia^2rho_rc_rX_1r
x_r=2k_ra
k_r=2pif/c_r
c_r=150
rho_r=Density(R134a,T=65,P=140convert(psi,kPa))
m_rr=X_rr/omega_r
k_r=omega_r/c_r
omega_1r=sqrt(s/(m+m_rr))
```

(Unit settings: kPa, C)

Table G.1 – Average ω'_o in R134a and Nitrogen over the frequency range 20-10,000Hz

Fluid	**Average ω'_o (Hz)**
Nitrogen	249,995
R134a	249,982
Absolute ω_o	*250,000*

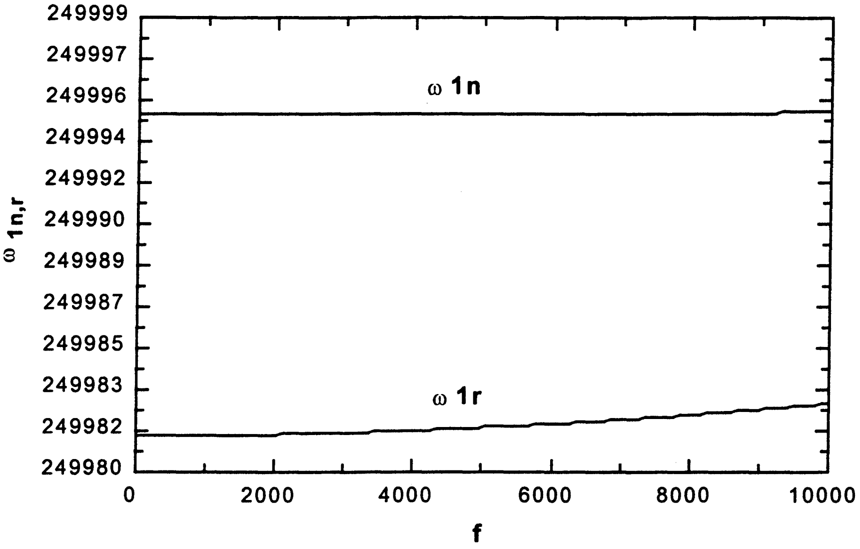

Figure G.1 – Natural frequency of microphones in R134a and Nitrogen
(Both axes in Hz)

As seen in Figure G.1, the natural frequency of the microphone is barely changed by the radiation mass of the two fluids. As such, the microphone calibration in Nitrogen is presumed valid in R134a.

Appendix F

Coherence Measurements

Preliminary tests were initially conducted on the Nitrogen test facility of Figure F.1 to determine if it could be used for the microphone calibration. We wanted to determine if the measured acoustic signal (generated by the orifice tube) in Nitrogen was strong enough to be clearly measured. Also, we wanted to see if the tube coils at the end of the test section could be used to provide an effective anechoic termination. Coherence measurements were taken at for a number of flow conditions and for several test section geometries. A matrix of experiments is shown in Table F.1 and the results are shown in Figure F.1. From the results it was apparent that the several test section configurations could be used for microphone calibration (as indicated by good coherence measurements). It was also clear that the tube coils could be used to provide a semi-anechoic termination. Finally, the effects of reflections on coherence measurements could be clearly seen.

Table F.1 – Test matrix for coherence measurements in Nitrogen.

Configuration	Test	Tin (C)	Pin (psig)	Tube before TS (A)	Tube after TS (B)	Coil at end?
A	1	22.02	50	22in	40in	yes
	2	22.03	150	22in	40in	yes
	3	21.3	250	22in	40in	yes
B	4	22.39	50	22in	40in	no
	5	22.06	150	22in	40in	no
	6	21.12	250	22in	40in	no
C	7	21.39	50	22in	0	no
	8	21.46	150	22in	0	no
	9	20.61	250	22in	0	no
D	10	21.51	50	0	0	no
	11	21.44	150	0	0	no
	12	20.52	250	0	0	no
E	13	21.29	50	0	22in	yes
	14	21.31	150	0	22in	yes
	15	20.5	250	0	22in	yes
F	16	20.94	50	0	22in	no
	17	20.98	150	0	22in	no
	18	19.97	250	0	22in	no

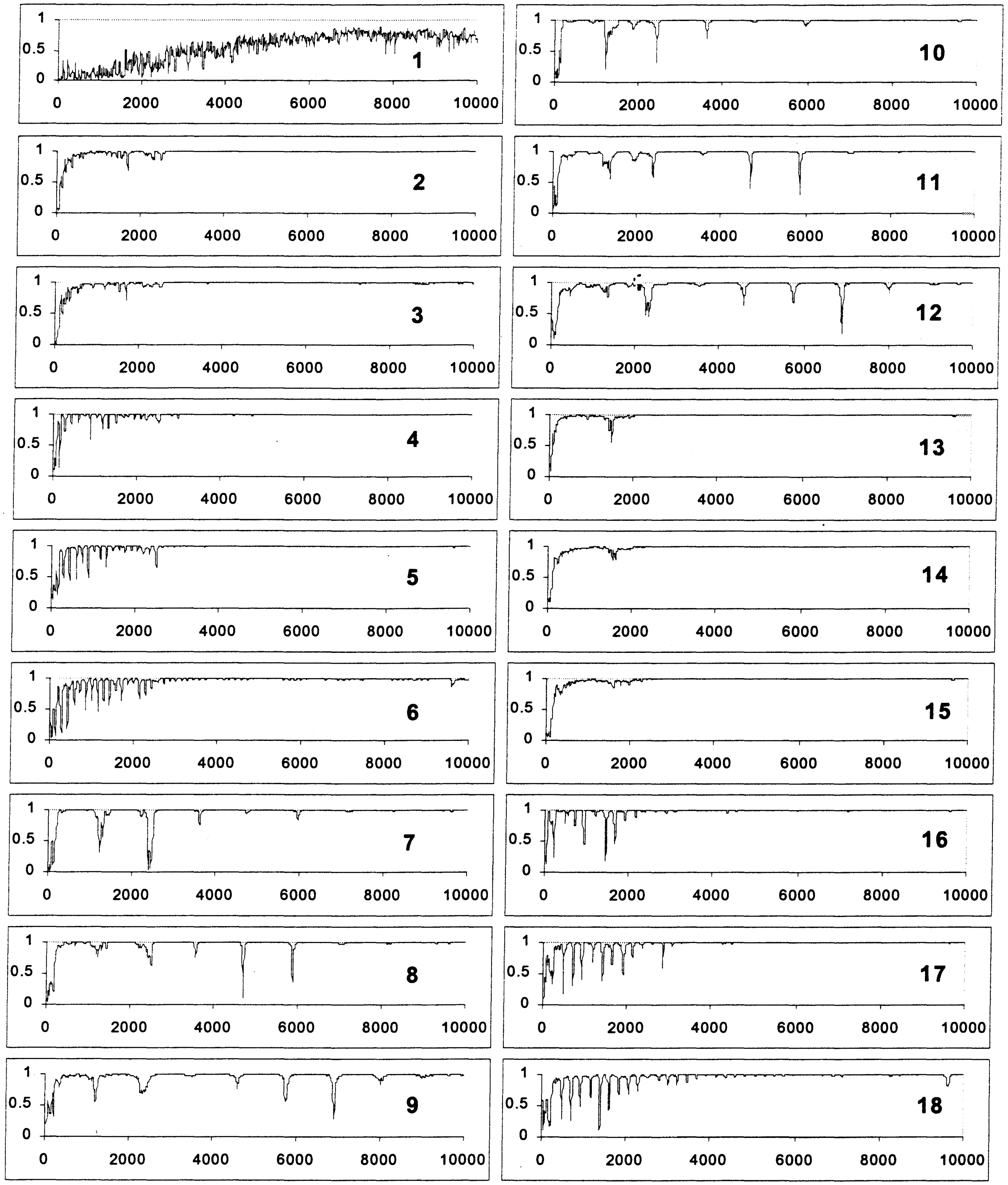

Figure F.1 – Coherence measurements in Nitrogen
Numbers are the test numbers from Table F.1

Appendix I

Electronic Expansion Valve Vibration Measurements

As described in Chapter 6, the electronic expansion valve tested displayed extra low frequency peaks in its external pipe-wall acceleration spectra during vapor flow. Measurements of surface accelerations were taken around the experimental test facility during similar vapor flow conditions to investigate the nature of the peaks. An illustration of the measurement locations is given in Figure I.1 and summarized in Table I.1. The actual measurements and measurement conditions are given in Figure I.2.

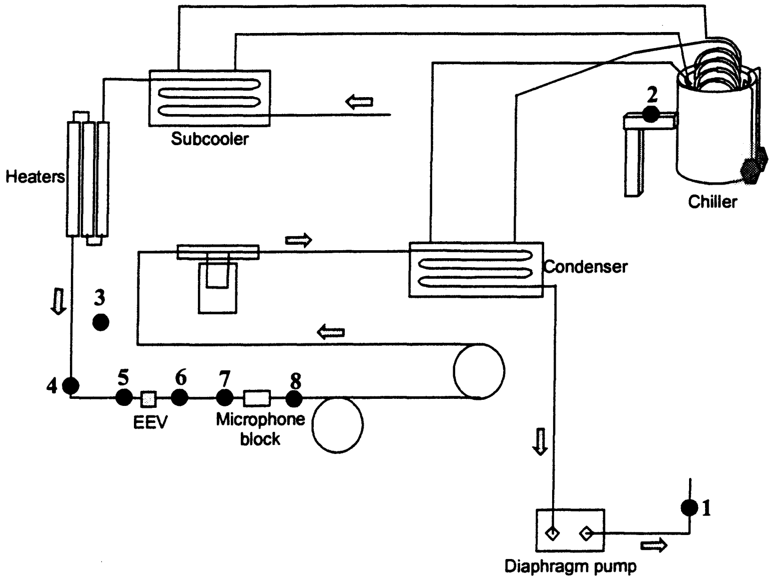

Figure I.1 – Acceleration measurement locations

Since the spectra at locations 1 and 2 show no evidence of the peaks, it can be concluded that neither the pump nor the chillers (the only self-vibrating components in the system) are a cause of the external pipe-wall vibrations at those frequencies. The spectra measured at locations 4, 5, 6, 7, and 8 all show evidence of the mysterious acceleration peaks. Since the peaks are evident both upstream and downstream of the valve and increase in magnitude closest to the valve, one might conclude that the valve itself (or part of it) is excited into some sort of resonance at that frequency. Those vibrations are then transmitted by solid contact along the test section tubing in both directions. Lastly, note that peaks are present downstream at the coincident frequencies, as expected (see Chapter 6).

Table I.1 – Acceleration measurement location descriptions

Location	Description
1	Structure near pump
2	Structure near chiller
3	Structure near test section
4	Tubing at start of test section
5	Tubing just upstream of EEV
6	Tubing just downstream of EEV
7	Tubing just upstresam of microphone block
8	Tubing just downstream of microphone block

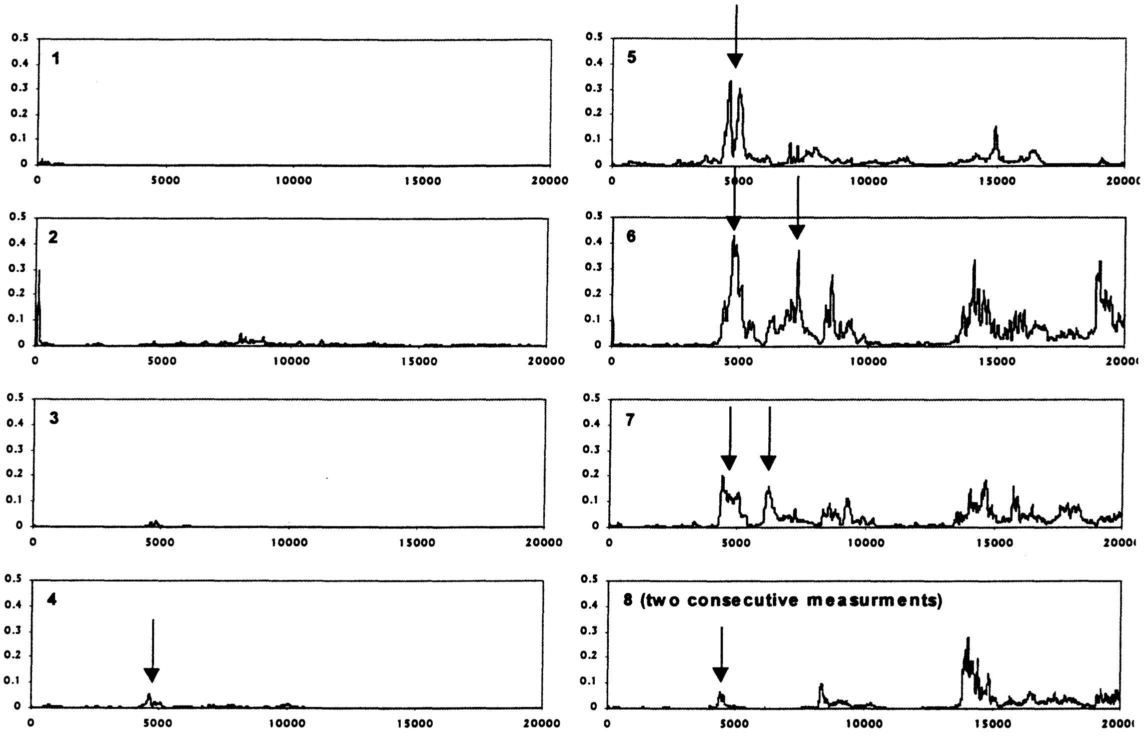

Figure I.2 – Acceleration measurements

All taken consecutively with system in steady state at Pin=21.7bara, Pout=4.25bara, Inlet Superheat = 9C, Outlet superheat = 35C, Mass flow rate = 105 lbm/hr

Arrows indicate the "mysterious" peaks

Appendix J

Outlet Temperature Correction

As mentioned in Appendix K, the outlet temperature for some of our early orifice tube data was measured at the exit of the test section, well downstream of the orifice tube exit (see Figure 2.1). Since the test section contains a very long section of copper tubing between the outlet of the orifice tube and the exit of the test section, there may be significant heat transfer between those two points. As a result, the temperature measured at the test section exit may be very different from the orifice tube outlet temperature. If the flow through the test section were entirely two-phase, the temperature changes would be very small, as only a small pressure drop exists across the tests section (see Appendix C). However, all of the data in question was taken for pure vapor flow through the test section. During vapor flow tests, temperature differences between the expansion device outlet and the test section exit are often greater than 10°C and have been as high as 25°C.

The outlet temperature for those data was corrected in the following manner: At the time the discrepancy was discovered, there existed 36 data points which had measured values for both the orifice tube outlet and the exit of the test section. Assuming isenthalpic expansion, the outlet temperatures for those points could be calculated from the inlet conditions and compared to the measured values. If this method was successful, the same procedure could be used to compute the missing outlet temperatures for the other (59) data points. The results are shown in Figure J.1.

The inlet and outlet enthalpies are very nearly equal, usually within 2-3%. Unfortunately, this leads to much larger over-predictions in temperature, around 13%. One possibility for the poor predictions is the sensitivity of temperature to enthalpy. Figure J.2 shows the vapor enthalpy for R134a over an appropriate temperature range (and vice versa) at 5bara pressure (a typical outlet pressure in our measurements). Recall that vapor enthalpy is a very weak function of pressure and can basically be considered a function of temperature only (see Appendix E).

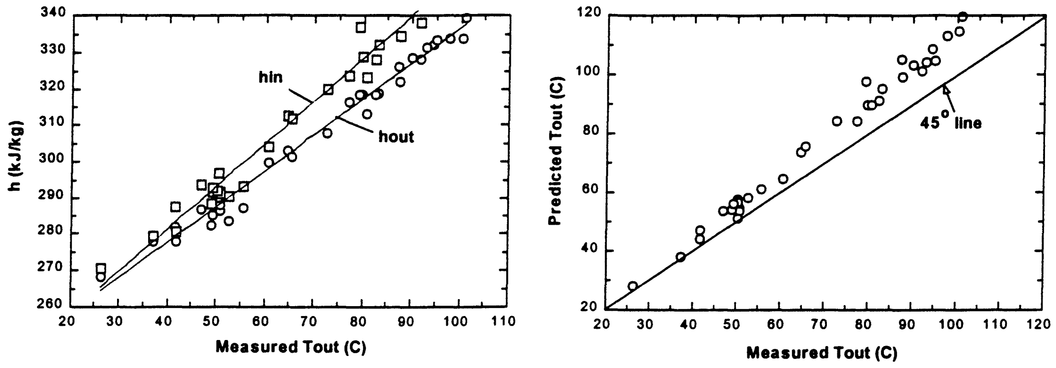

Figure J.1 – Inlet and outlet enthalpy and predicted outlet temperature vs. measured outlet temperature for some orifice tube vapor data.

Line through enthalpy are linear best-fits.

Since the relationship over this temperature range is very nearly linear, dh/dT = slope of the h vs. T curve = 0.978kJ/kg/K. Thus around a moderate temperature value of 45°C (h=282.7 kJ/kg), a one percent change in temperature leads to only a 0.15% change in enthalpy. Thus even highly erroneous temperatures can yield accurate enthalpies. However, dT/dh = slope of T vs. h curve = 1.02K/kJ/kg. Thus a one percent change in enthalpy leads to a 6.6% change in temperature. A two percent change in enthalpy leads to a 13.2% change in temperature, and so on. Thus a 2-3% error in enthalpy could easily yield a 13-20% error in temperature predicted from enthalpy.

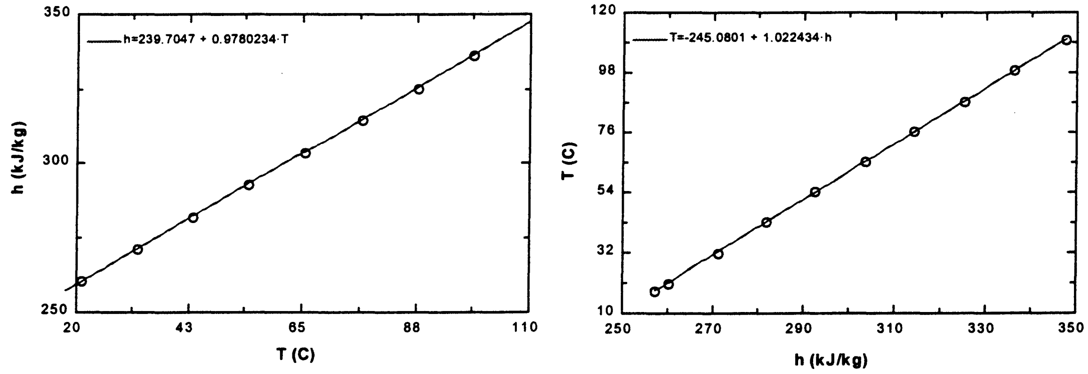

Figure J.2 – Enthalpy vs. temperature and temperature vs. enthalpy for vapor R134a at a pressure of 5bars

However, the predicted temperatures are always over-predicted, indicating a systematic error. One possibility is the isenthalpic assumption. Another is the assumption that the measured outlet temperature, which is measured by as well-insulated surface thermocouple (see Chapter 2), is exactly the internal fluid temperature. If there was indeed a temperature and/or enthalpy loss (as would be the case), this would lead to a constant over-prediction in outlet temperature from outlet enthalpy.

Since the source of this discrepancy is not confirmed, and for consistency amongst all of our data, it would be desirable to have a method to predict the outlet temperatures to match the measured temperatures more closely. This can be achieved by applying a correction factor to the outlet enthalpy. EES was used to determine the correction factor: $h_{in} = h_{out} + c$, where $c = 5.593239 - 0.47979T_{downsteam} + 0.3496268T_{outlet}$. EES can then be used to solve for outlet temperature given inlet pressure and temperature and outlet pressure. The EES code is given below and the results are given in Figure J.3. The results for nearly all vapor data to date (approx. 120 points) for all expansion devices tested is given in Figure J.4 with and without correction applied.

```
hin=Enthalpy(R134a,P=Pin,T=Tin) "kJ/kg"
hout=Enthalpy(R134a,P=Pout,T=Tout) "kJ/kg"
hin=hout+c "kJ/kg"
c=5.593239-4.7979E-01Tdown+0.3496268Tsurf "kJ/kg"
```

(Unit system: bar, C)

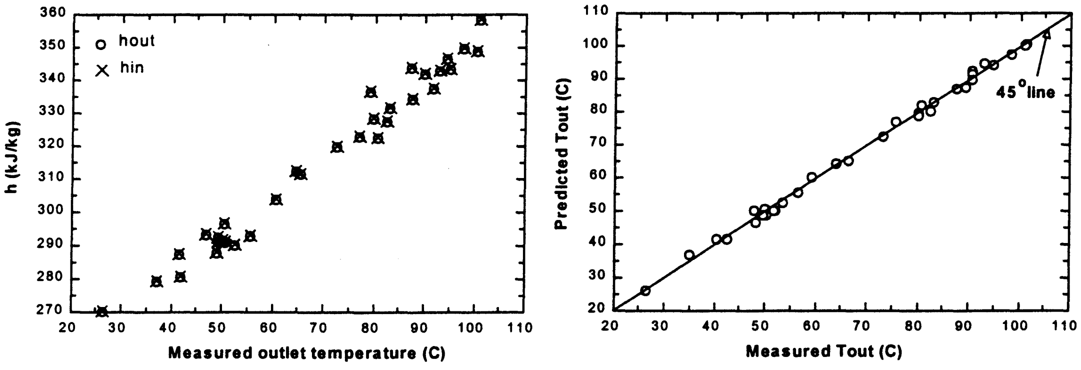

Figure J.3 – Inlet and outlet enthalpy and predicted outlet temperature using correction factor.

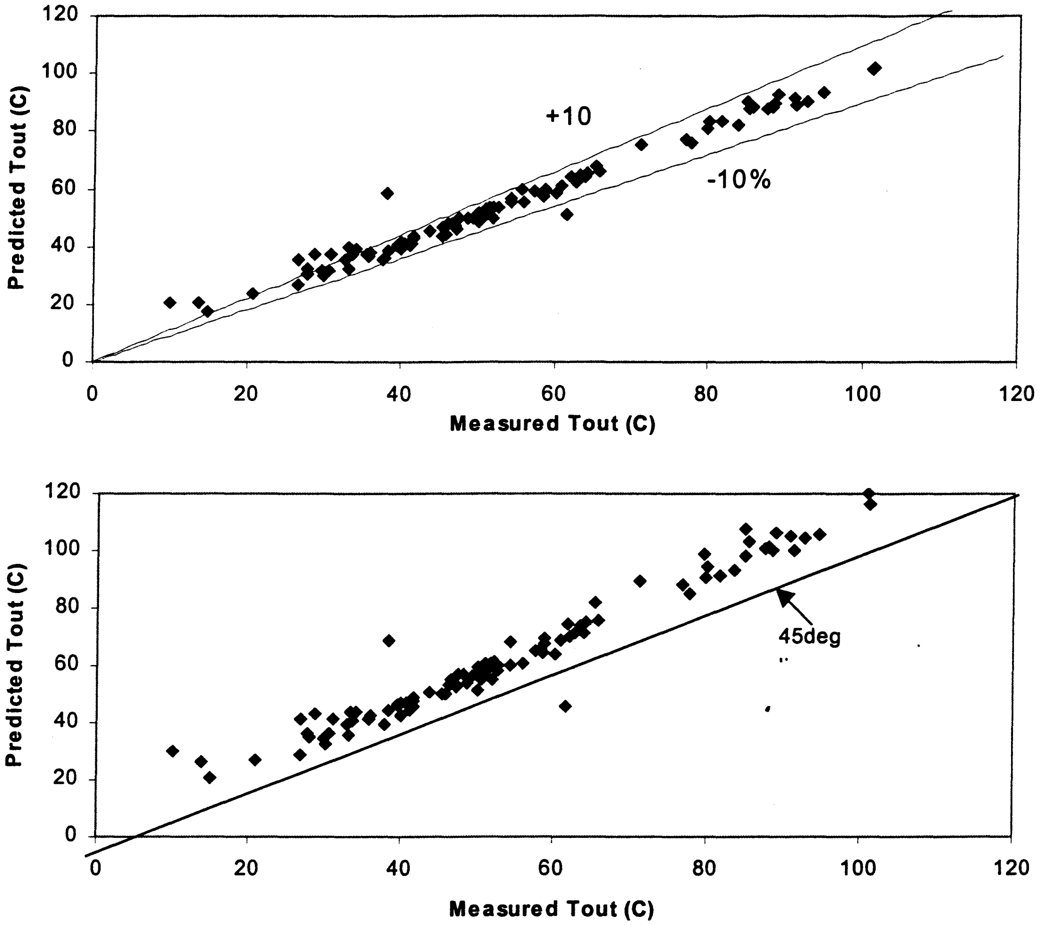

Figure J.4 – Predicted vs. measured outlet temperature for all vapor data to date with correction (above) and without correction (below)

Some additional methods were tried to estimate the missing outlet temperatures: Heat transfer estimation from the test section, conservation of energy applied to the test section, and generalized 1-D flow (heat transfer, friction) integration. However, all of these methods involved an empirical correllation of some sort and in that sense seemed no more fundamental than the current method. These methods all yielded poorer results than the present method and in some cases were a good deal more complicated.

Appendix K

Experimental Data in Refrigerant

This section contains all of the experimental data in refrigerant. The data are combined into and presented in the following categories:

1. **Original orifice tube data** – This is a large set of vapor flow data taken with orifice tubes of three different diameters (blue, orange, and brown) and two different lengths, with and without inlet and outlet screens. The data was taken over a wide but scattered range of mass flow rates, pressures, and superheats. The brown orifice tube data in this set is presented separately from other brown orifice tube data because all other brown orifice tube data sets were taken with mass flow rate and outlet pressure held constant over each set. As this set was the first data set I took, I named it "original" orifice tube data.
2. **Brown orifice tube data**
3. **Brown orifice tube data with downstream screen**
4. **Long (copper) capillary tube data**
5. **Mid-length (copper) capillary tube data**
6. **Short (copper) capillary tube data**
7. **Short (copper) capillary tube data with 5 degree cone**
8. **Short (copper) capillary tube data with 10 degree cone**
9. **Aluminum capillary tube data**
10. **Thermostatic expansion valve data**
11. **Electronic expansion valve data**

Table K.1 - Original orifice tube vapor data
Shading used to separate data sets
Orifice tube outlet temperature estimated (see Appendix J)
Spectra only measured to 10kHz

Orifice Diameter [mm]	Orifice Length [in]	Inlet/ Outlet Screens?	Inlet Pressure [bars]	Outlet Pressure [bars]	Inlet Superheat [C]	Oulet Superheat [C]	Mass flow rate [lbm/hr]	TS exit Temp. [C]	TSPL re 20E-6 Pa [dB]
1.7	0.937	NO/NO	11.79	5.48	50.75	70.39*	69.73	43.60	152.98**
1.7	0.937	NO/NO	14.08	4.69	6.96	27.55*	90.77	31.51	159.03**
1.7	0.937	NO/NO	16.12	5.06	14.51	38.14*	105.23	35.53	160.22**
1.7	0.937	NO/NO	17.14	5.54	28.14	54.19*	106.82	44.10	160.32**
1.7	0.937	NO/NO	20.90	5.93	0.97	19.85*	144.31	31.95	162.07**
1.7	0.937	NO/NO	10.00	5.80	3.64	13.11*	62.50	35.00	148.15**
1.7	0.937	NO/NO	11.56	6.00	57.03	74.24*	65.95	47.93	155.87
1.7	0.937	NO/NO	11.68	6.67	20.72	32.52*	72.73	37.33	155.40
1.7	0.937	NO/NO	10.78	6.75	12.09	21.03*	66.15	33.09	151.46
1.7	0.937	NO/NO	9.84	6.66	79.84	90.7*	52.79	46.82	163.77
1.7	0.937	NO/NO	9.88	6.67	79.33	90.25*	52.19	46.87	148.18
1.7	0.937	NO/NO	10.06	7.34	55.15	63.28*	52.39	43.09	145.77
1.7	0.937	NO/NO	9.49	6.56	37.28	45.97*	54.28	37.21	147.39
1.7	0.937	NO/NO	9.88	6.54	6.14	13.44*	59.07	29.92	149.80
1.7	0.937	NO/NO	14.95	6.18	36.38	57.76*	87.48	48.67	162.31
1.7	0.937	NO/NO	15.13	6.83	72.01	94.55*	83.19	60.93	161.34
1.7	0.937	NO/NO	14.91	6.02	20.06	39.38*	93.36	41.31	162.60
1.7	0.937	NO/NO	15.97	5.49	0.01	17.03*	112.50	19.17	158.37
1.7	0.937	NO/NO	17.85	5.92	14.14	36.13*	115.20	41.66	166.35
1.7	0.937	NO/NO	17.59	5.77	3.06	21.58*	116.39	35.71	166.41
1.7	1.5	YES/YES	13.87	5.59	27.95	48.71*	82.30	40.74	147.72
1.7	1.5	YES/YES	14.01	6.07	63.84	86.68*	77.51	54.42	147.24
1.7	1.5	YES/YES	17.40	5.60	21.87	46.65*	110.21	44.41	148.44
1.7	1.5	YES/YES	15.58	5.57	56.81	84.37*	90.17	57.11	148.02
1.7	1.5	YES/YES	12.67	6.10	46.39	64.87*	74.72	48.53	144.57
1.7	1.5	YES/YES	12.18	5.64	21.49	38.08*	73.52	37.34	145.72
1.7	1.5	YES/YES	15.85	5.69	12.67	32.85*	101.54	38.74	147.46
1.7	1.5	YES/YES	9.68	6.22	42.75	53.51*	54.08	39.63	142.68
1.45	1.5	YES/NO	12.86	5.31	62.28	86.1*	51.59	43.80	157.00
1.45	1.5	YES/NO	12.93	5.57	31.99	51.7*	54.68	38.25	156.85
1.45	1.5	YES/NO	12.61	5.58	13.60	29.9*	56.28	32.37	156.88
1.45	1.5	YES/NO	11.00	5.32	58.77	77.85*	45.81	38.42	153.51
1.45	1.5	YES/NO	11.05	5.31	30.78	47.66*	48.70	36.09	153.55
1.45	1.5	YES/NO	9.21	5.52	35.52	47.48*	38.83	33.08	147.94
1.45	1.5	YES/NO	9.29	5.75	83.61	96.95*	35.04	37.91	147.15
1.45	1.5	YES/NO	19.56	5.27	70.19	107.54*	79.90	61.95	164.58
1.45	1.5	YES/NO	20.18	5.29	42.25	76.38*	85.29	52.59	165.08
1.45	1.5	YES/NO	20.17	5.58	9.14	32.87*	96.45	39.10	165.45
1.45	1.5	YES/NO	16.33	5.93	31.29	55.1*	71.53	43.44	161.21
1.45	1.5	YES/NO	15.97	5.26	61.55	91.9*	66.84	51.75	162.12
1.45	1.5	YES/NO	18.18	5.35	46.31	77.99*	76.41	50.36	163.93
1.45	1.5	YES/NO	18.35	5.62	14.96	38.9*	84.09	38.63	164.36
1.45	1.5	YES/NO	14.38	5.89	23.51	43.15*	65.45	38.17	159.72
1.45	1.5	YES/NO	13.94	5.29	68.30	95.02*	56.28	48.58	160.11

Table K.1 - Original orifice tube vapor data, continued
Shading used to separate data sets
Orifice tube outlet temperature estimated (see Appendix J)
Spectra only measured to 10kHz

Orifice Diameter [mm]	Orifice Length [in]	Inlet/ Outlet Screens?	Inlet Pressure [bars]	Outlet Pressure [bars]	Inlet Superheat [C]	Oulet Superheat [C]	Mass flow rate [lbm/hr]	TS exit Temp. [C]	TSPL re 20E-6 Pa [dB]
1.22	1.5	YES/NO	21.88	4.85	6.41	33.07*	67.54	34.69	160.57
1.22	1.5	YES/NO	21.31	4.83	41.97	79.85*	59.57	42.86	159.99
1.22	1.5	YES/NO	18.96	5.01	57.40	93.63*	50.89	43.05	159.00
1.22	1.5	YES/NO	19.52	5.32	21.93	50.45*	56.67	37.76	159.45
1.22	1.5	YES/NO	18.18	4.82	42.68	76.44*	49.10	40.33	158.51
1.22	1.5	YES/NO	17.74	4.77	9.05	34.06*	53.09	32.17	158.89
1.22	1.5	YES/NO	15.91	4.77	62.22	95.06*	42.82	38.81	157.04
1.22	1.5	YES/NO	15.93	4.93	9.65	32.24*	48.20	30.00	157.79
1.22	1.5	YES/NO	14.02	4.76	64.88	94.33*	36.14	36.36	155.30
1.22	1.5	YES/NO	14.31	4.79	19.37	42.89*	40.42	32.96	155.74
1.22	1.5	YES/NO	12.81	4.81	63.87	90.3*	32.85	33.10	152.80
1.22	1.5	YES/NO	12.83	4.94	17.98	38.15*	37.63	29.71	152.92
1.22	1.5	YES/NO	11.00	4.73	70.28	93.12*	27.36	30.53	149.39
1.22	1.5	YES/NO	11.24	4.78	22.96	41.74*	31.65	28.92	150.02
1.7	1.5	YES/NO	15.89	3.84	41.47	70.00	93.16	49.19	163.44
1.7	1.5	YES/NO	17.39	3.91	15.22	43.70	108.52	38.94	164.47
1.7	1.5	YES/NO	18.30	5.58	9.90	30.88	117.89	40.17	165.02
1.7	1.5	YES/NO	14.74	6.19	54.35	68.76	84.99	54.20	161.12
1.7	1.5	YES/NO	14.15	6.29	15.56	27.44	88.08	39.78	161.72
1.7	1.5	YES/NO	11.36	6.15	54.85	61.30	66.25	48.40	156.71
1.7	1.5	YES/NO	11.24	6.19	10.37	18.56	71.73	33.30	157.14
1.7	1.5	YES/NO	11.46	3.89	67.27	84.66	64.25	48.46	160.24
1.7	1.5	YES/NO	11.91	3.92	9.07	29.41	76.91	30.61	160.76
1.7	1.5	YES/NO	17.60	4.19	21.58	49.74	108.32	43.22	165.35
1.7	1.5	YES/NO	13.75	4.03	63.24	85.54	79.11	54.68	161.64
1.45	1.5	YES/YES	21.18	4.27	39.28	68.90	86.68	50.14	148.87
1.45	1.5	YES/YES	20.29	4.26	15.49	40.69	92.56	38.13	149.46
1.45	1.5	YES/YES	18.11	4.12	55.32	81.17	72.53	50.48	148.48
1.45	1.5	YES/YES	17.20	4.11	14.53	37.17	76.51	35.25	156.86
1.45	1.5	YES/YES	14.14	4.06	76.13	91.73	54.88	46.39	146.85
1.45	1.5	YES/YES	13.99	4.10	12.93	31.97	62.26	32.83	146.86
1.45	1.5	YES/YES	8.96	3.78	69.09	72.47	35.44	33.03	144.49
1.45	1.5	YES/YES	8.99	3.76	5.15	19.68	39.93	28.22	143.73
1.45	1.5	YES/YES	24.10	8.79	33.01	47.09	106.52	55.63	149.75
1.45	1.5	YES/YES	23.71	8.81	8.97	19.54	109.91	41.76	149.84
1.45	1.5	YES/YES	21.06	7.55	44.38	59.20	86.48	55.32	148.60
1.45	1.5	YES/YES	20.97	7.66	7.24	18.76	98.05	38.54	148.64
1.45	1.5	YES/YES	17.77	8.66	62.33	67.15	70.03	54.13	147.37
1.45	1.5	YES/YES	17.59	8.81	11.20	17.88	79.80	39.48	147.58
1.45	1.5	YES/YES	14.15	6.44	33.37	41.89	59.77	39.74	146.28
1.45	1.5	YES/YES	10.79	6.24	21.85	26.58	44.91	34.32	144.11

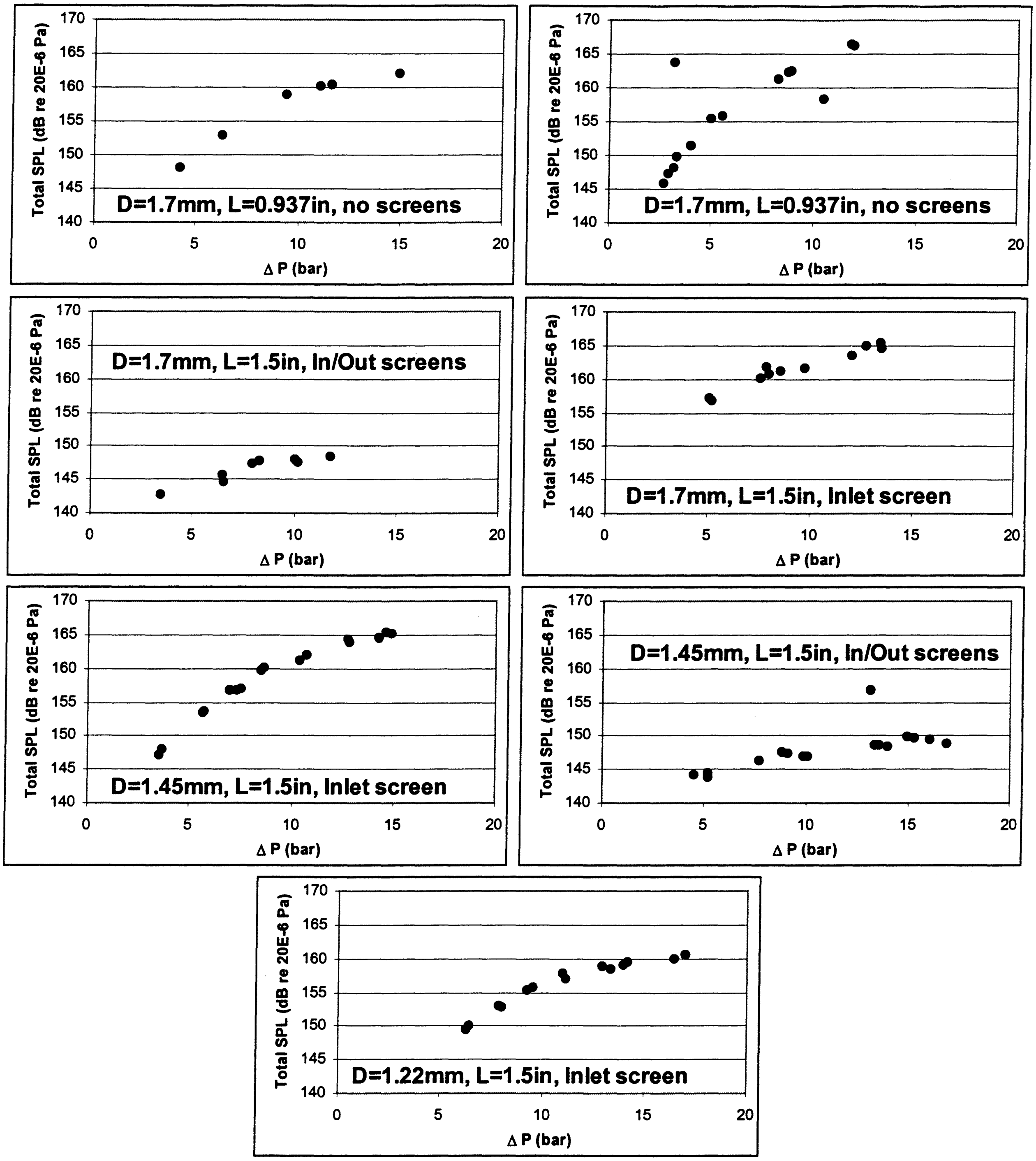

Figure K.1 - Original orifice tube vapor data: TSPL vs. ΔP

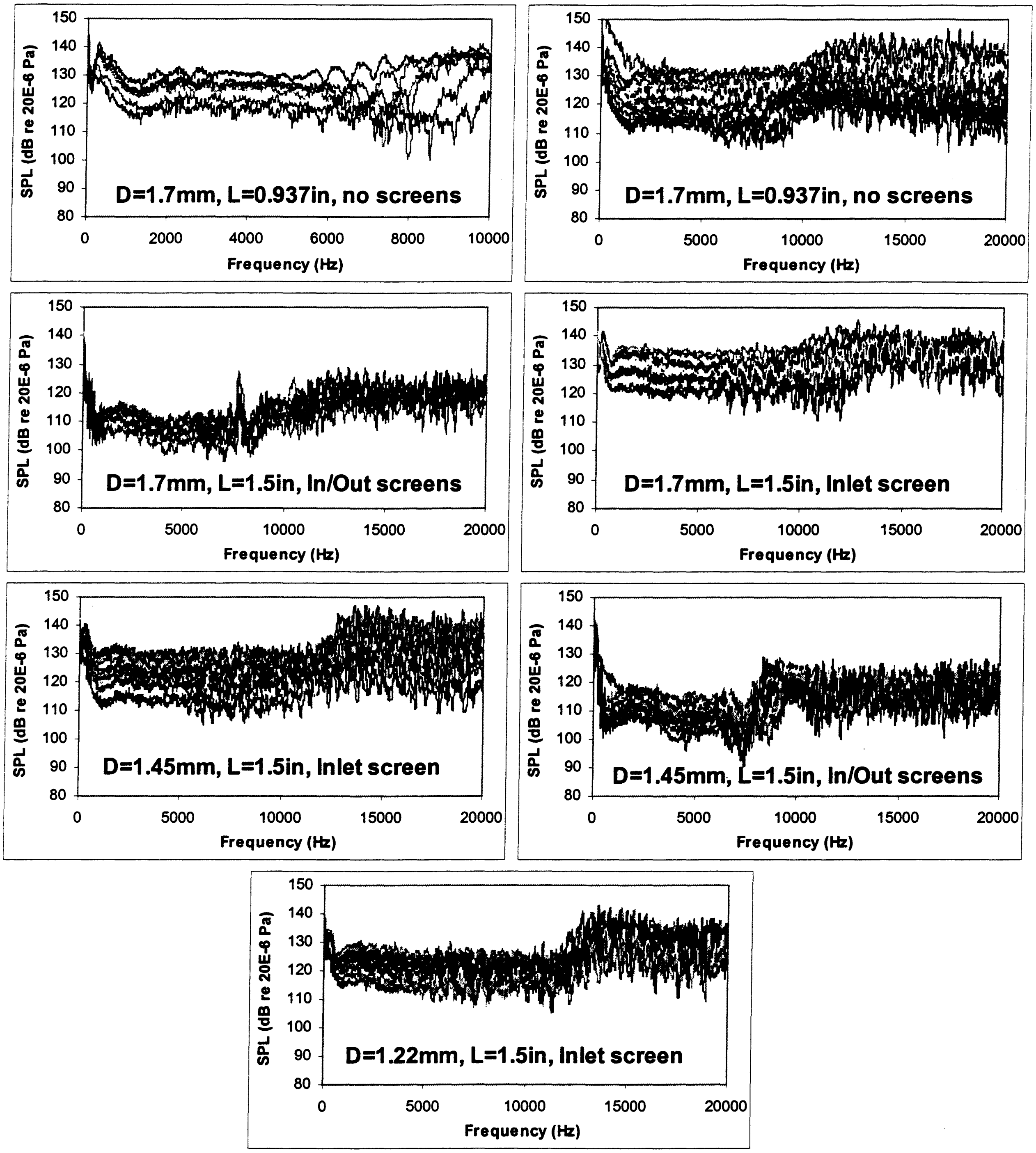

Figure K.2 - Original orifice tube vapor data: SPL

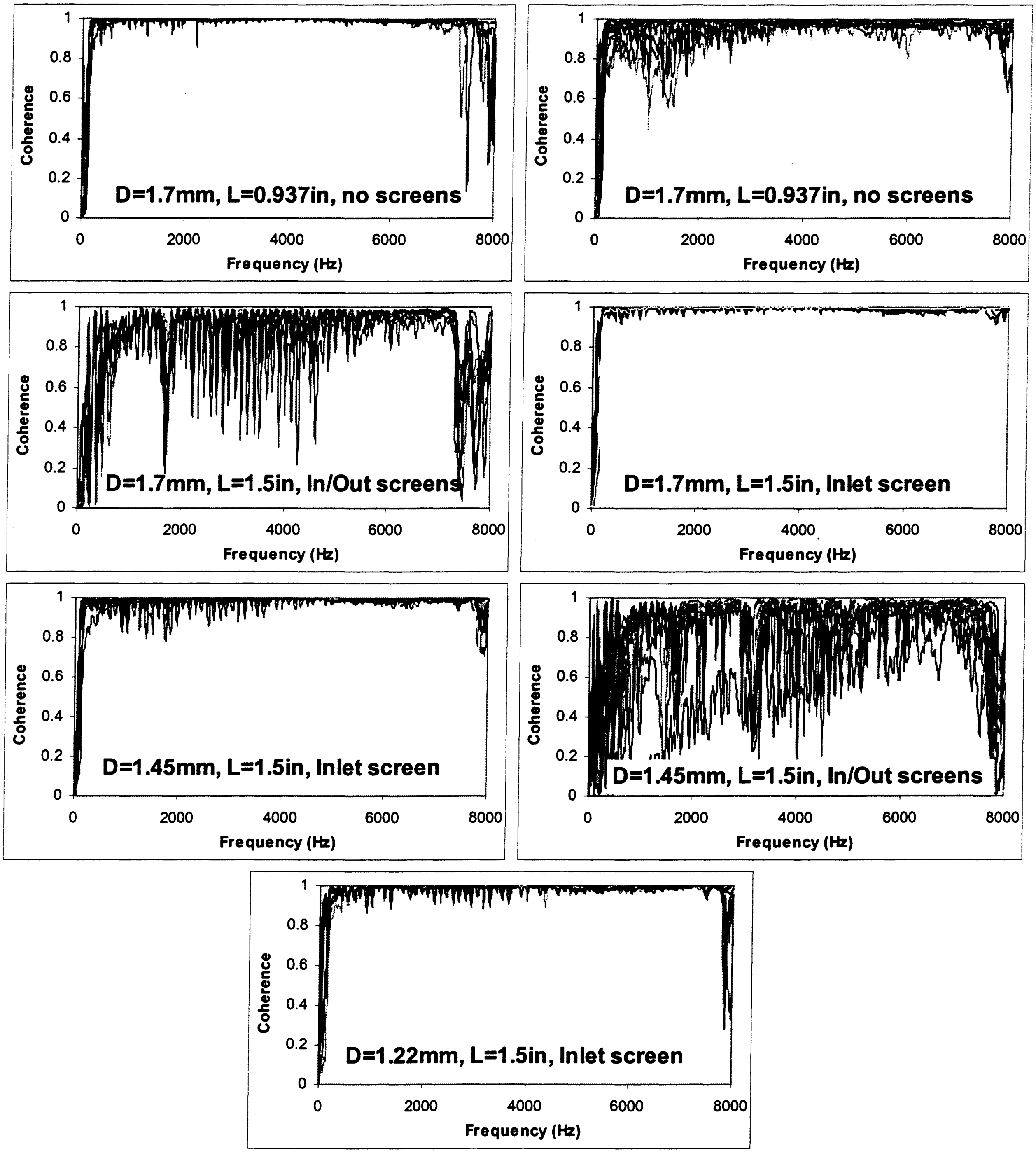

Figure *K.3 - Original orifice tube vapor data: Coherence

Figure *K.2 - Brown orifice tube data
D=1.22mm, L=1.5in, Inlet screen only
Shading used to separate data sets

Inlet	Outlet	Inlet	Oulet	Inlet	Outlet	Mass flow	TS exit	TSPL
Pressure	Pressure	Superheat	Superheat	Quality	Quality	rate	Temp.	re 20E-6 Pa
[bars]	[bars]	[C]	[C]	[-]	[-]	[lbm/hr]	[C]	[dB]
27.67	4.53	two-phase	3.08	0.89	vapor	100.13	13.30	154.78
28.10	4.55	two-phase	2.94	0.94	vapor	99.83	15.03	155.25
26.09	4.14	two-phase	two-phase	0.73	0.98	100.41	10.20	153.07
24.22	3.88	two-phase	two-phase	0.55	0.87	100.66	7.95	151.70
22.31	4.03	two-phase	two-phase	0.44	0.78	100.37	8.64	150.06
20.22	4.32	two-phase	two-phase	0.31	0.66	100.11	11.09	148.88
18.91	4.02	two-phase	two-phase	0.23	0.59	100.54	9.33	147.04
15.74	3.96	two-phase	two-phase	0.12	0.46	100.09	8.37	144.65
13.77	3.98	two-phase	two-phase	0.06	0.37	100.35	8.64	141.58
10.97	3.76	two-phase	two-phase	0.01	0.28	100.31	6.98	135.97
8.53	3.72	-3.16	two-phase	liquid	0.18	99.96	6.65	129.47
26.31	4.42	22.28	51.51	vapor	vapor	75.28	39.26	162.25
25.50	4.38	14.23	40.37	vapor	vapor	74.99	34.84	162.48
24.84	4.33	6.88	30.36	vapor	vapor	75.12	32.06	162.34
23.62	4.19	0.01	17.52	vapor	vapor	74.81	26.79	161.49
21.41	4.33	two-phase	2.05	0.85	vapor	75.74	11.59	151.47
21.36	4.33	two-phase	1.98	0.86	vapor	75.39	11.53	151.60
19.93	4.04	two-phase	two-phase	0.71	0.94	75.09	9.51	149.46
19.09	4.11	two-phase	two-phase	0.65	0.88	75.06	9.70	149.41
17.64	4.16	two-phase	two-phase	0.52	0.77	74.70	10.09	147.74
16.08	4.31	two-phase	two-phase	0.41	0.67	74.97	10.75	146.27
14.40	4.21	two-phase	two-phase	0.32	0.57	74.77	10.57	144.78
12.78	4.22	two-phase	two-phase	0.21	0.46	75.08	10.51	142.85
11.40	4.01	two-phase	two-phase	0.15	0.39	74.46	9.05	140.53
9.67	3.69	two-phase	two-phase	0.07	0.29	75.33	6.60	134.99
8.33	3.52	two-phase	two-phase	0.03	0.22	74.29	5.20	131.31
25.87	3.20	22.33	60.14	vapor	vapor	74.86	37.89	160.66
25.10	3.18	13.00	48.44	vapor	vapor	74.85	34.71	160.53
24.19	3.20	5.61	35.83	vapor	vapor	74.58	28.86	160.81
22.55	3.10	two-phase	13.58	1.00	vapor	74.59	20.18	159.71
20.47	3.01	two-phase	3.90	0.82	vapor	75.21	14.32	149.89
19.41	2.98	two-phase	two-phase	0.72	0.96	74.30	9.61	148.42
16.57	2.88	two-phase	two-phase	0.47	0.77	74.51	0.37	146.20
16.59	2.88	two-phase	two-phase	0.47	0.77	74.47	0.38	146.27
15.17	2.84	two-phase	two-phase	0.35	0.67	75.45	0.08	144.36
13.49	2.78	two-phase	two-phase	0.26	0.57	74.93	-0.44	142.50
11.89	2.86	two-phase	two-phase	0.18	0.47	74.90	0.21	139.39
10.38	2.64	two-phase	two-phase	0.12	0.40	74.37	-2.13	137.44
8.32	2.65	two-phase	two-phase	0.03	0.27	75.29	-1.78	132.36
7.18	2.60	two-phase	two-phase	0.00	0.21	75.29	-2.35	129.85
31.17	7.79	4.91	15.81	vapor	vapor	100.73	35.18	162.59
30.45	8.19	0.09	1.18	vapor	vapor	101.44	32.38	156.11
27.99	8.29	two-phase	two-phase	0.88	1.00	100.28	33.16	153.12
26.87	7.92	two-phase	two-phase	0.75	0.93	100.71	32.31	151.41
25.49	8.53	two-phase	two-phase	0.65	0.85	100.14	34.06	150.74
23.77	8.25	two-phase	two-phase	0.50	0.74	100.46	32.45	149.93
21.80	7.91	two-phase	two-phase	0.39	0.65	98.95	32.23	148.07
19.62	8.25	two-phase	two-phase	0.28	0.52	99.02	31.85	146.76
17.98	8.03	two-phase	two-phase	0.19	0.43	99.56	31.81	145.47
15.89	7.78	two-phase	two-phase	0.11	0.33	100.74	31.89	142.15

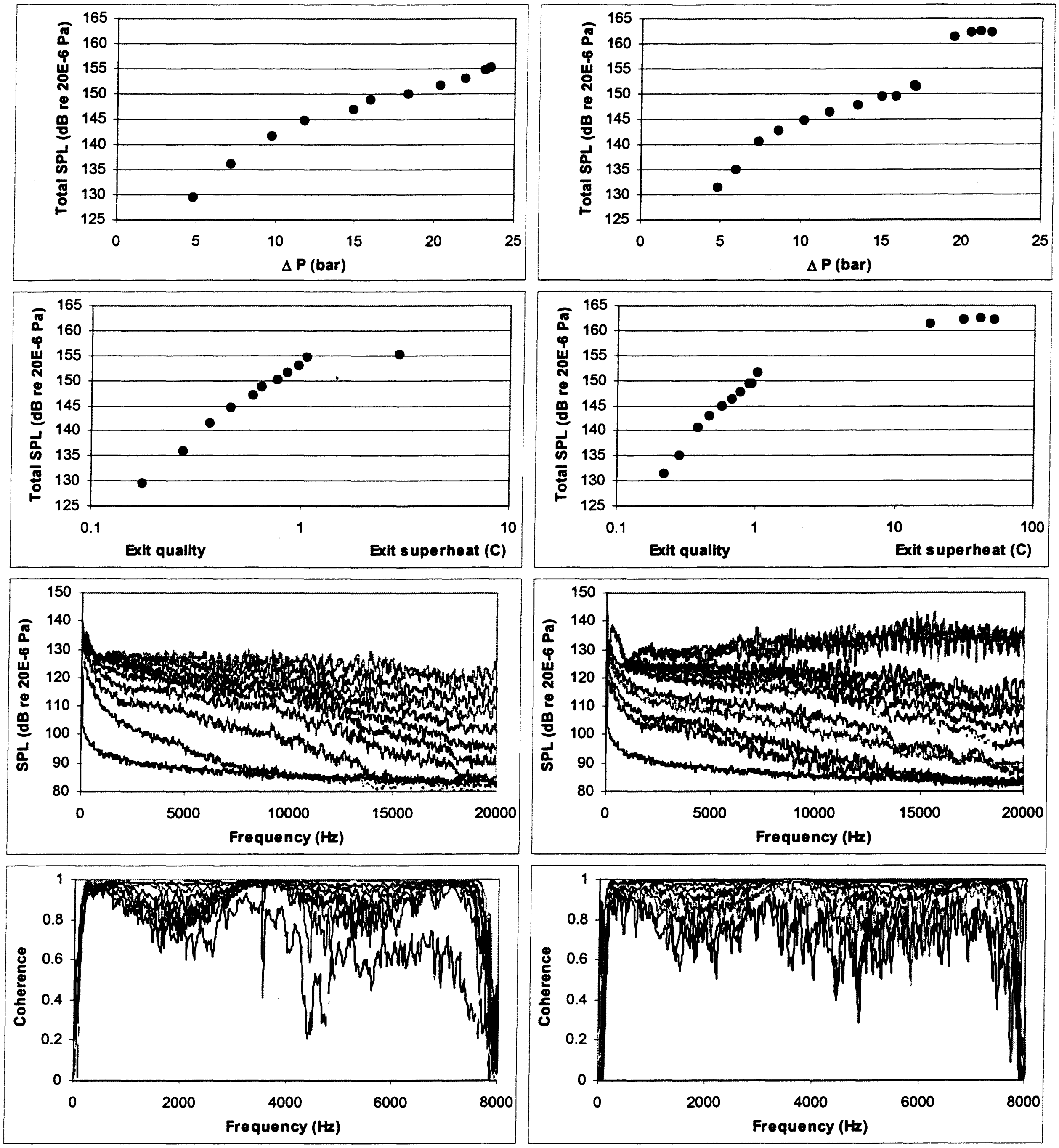

Figure *K.4 - Brown orifice tube data
D=1.22mm, L=1.5in, Inlet screen only
Left column: mass flow rate = 100lbm/hr, outlet pressure = 4bars
Right column: mass flow rate = 75lbm/hr, outlet pressure = 4bars

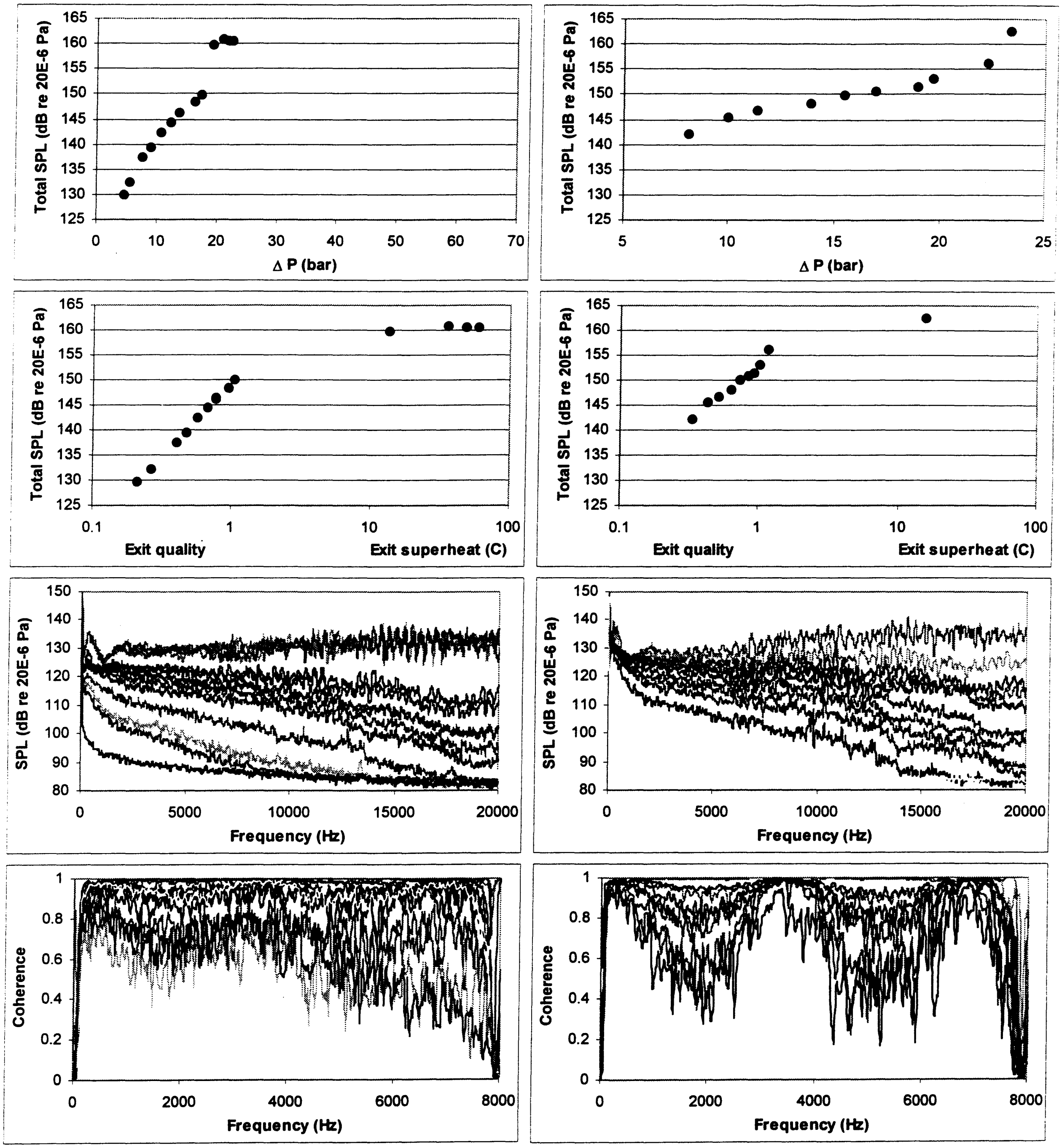

Figure *K.5 - Brown orifice tube data
D=1.22mm, L=1.5in, Inlet screen only
Left column: mass flow rate = 100lbm/hr, outlet pressure = 4bars
Right column: mass flow rate = 75lbm/hr, outlet pressure = 4bars

Table K.3 - Brown orifice tube data with downstream screen
D=1.22mm, L=1.5in, Inlet and outlet screens
Shading used to separate data sets

Inlet Pressure [bars]	Outlet Pressure [bars]	Inlet Superheat [C]	Oulet Superheat [C]	Inlet Quality [-]	Outlet Quality [-]	Mass flow rate [lbm/hr]	TS exit Temp. [C]	TSPL re 20E-6 Pa [dB]
28.74	4.60	two-phase	2.69	0.98	vapor	100.46	17.00	137.76
26.78	4.22	two-phase	two-phase	0.79	1.00	100.19	11.04	136.76
25.03	3.94	two-phase	two-phase	0.61	0.91	100.39	9.16	137.30
23.31	3.89	two-phase	two-phase	0.49	0.83	99.65	8.82	136.07
21.33	4.09	two-phase	two-phase	0.36	0.71	100.07	10.20	135.00
19.40	4.02	two-phase	two-phase	0.26	0.62	99.90	9.63	133.73
17.14	3.94	two-phase	two-phase	0.17	0.52	100.15	9.33	131.77
14.77	4.04	two-phase	two-phase	0.09	0.42	100.09	9.64	128.83
12.44	4.13	two-phase	two-phase	0.04	0.32	100.28	10.03	130.54
9.99	3.92	two-phase	two-phase	0.00	0.23	99.46	8.61	126.43
7.71	3.69	-4.31	two-phase	liquid	0.14	100.45	7.28	127.41
8.63	2.48	-2.36	two-phase	liquid	0.25	100.76	-3.67	136.48
10.70	2.61	two-phase	two-phase	0.02	0.33	99.94	-2.37	133.32
13.32	2.71	two-phase	two-phase	0.07	0.42	99.49	-1.45	133.07
15.98	2.91	two-phase	two-phase	0.15	0.53	99.45	0.33	134.06
18.38	2.98	two-phase	two-phase	0.23	0.62	100.51	1.04	135.26
20.83	3.05	two-phase	two-phase	0.36	0.74	99.34	1.91	136.74
22.90	3.08	two-phase	two-phase	0.44	0.81	101.39	2.04	136.87
25.22	3.22	two-phase	two-phase	0.59	0.92	101.42	3.25	136.49
27.04	3.45	two-phase	two-phase	0.76	1.00	100.32	9.35	135.92
23.58	5.43	9.16		vapor	vapor	97.73	15.66	137.83
28.44	5.53	40.67	69.24	vapor	vapor	75.44	48.65	146.31
28.39	5.56	40.37	68.48	vapor	vapor	75.34	48.81	146.33
27.62	5.33	31.30	59.15	vapor	vapor	75.05	44.59	145.93
26.93	5.24	22.01	46.87	vapor	vapor	74.79	39.36	145.73
26.29	5.06	17.59	42.63	vapor	vapor	74.65	36.90	145.71
24.86	4.82	4.94	25.96	vapor	vapor	75.00	30.46	143.87
25.56	4.85	11.79	35.83	vapor	vapor	74.71	33.58	144.34
23.99	4.05	two-phase	19.43	1.00	vapor	75.20	26.08	143.29
22.17	4.23	two-phase	2.16	0.94	vapor	74.96	16.44	135.32
21.20	4.20	two-phase	two-phase	0.84	1.00	74.95	10.88	134.14
20.60	4.19	two-phase	two-phase	0.74	0.95	75.02	10.77	133.99
19.32	4.18	two-phase	two-phase	0.64	0.88	74.76	10.95	133.33
17.48	4.18	two-phase	two-phase	0.47	0.74	74.84	10.87	132.52
16.04	4.10	two-phase	two-phase	0.36	0.64	74.80	10.31	131.58
14.25	4.08	two-phase	two-phase	0.27	0.54	74.71	10.24	130.89
12.63	4.43	two-phase	two-phase	0.19	0.43	75.61	12.25	132.49
11.37	4.34	two-phase	two-phase	0.12	0.35	74.91	11.83	132.54
9.57	4.03	two-phase	two-phase	0.05	0.26	74.86	9.74	127.54

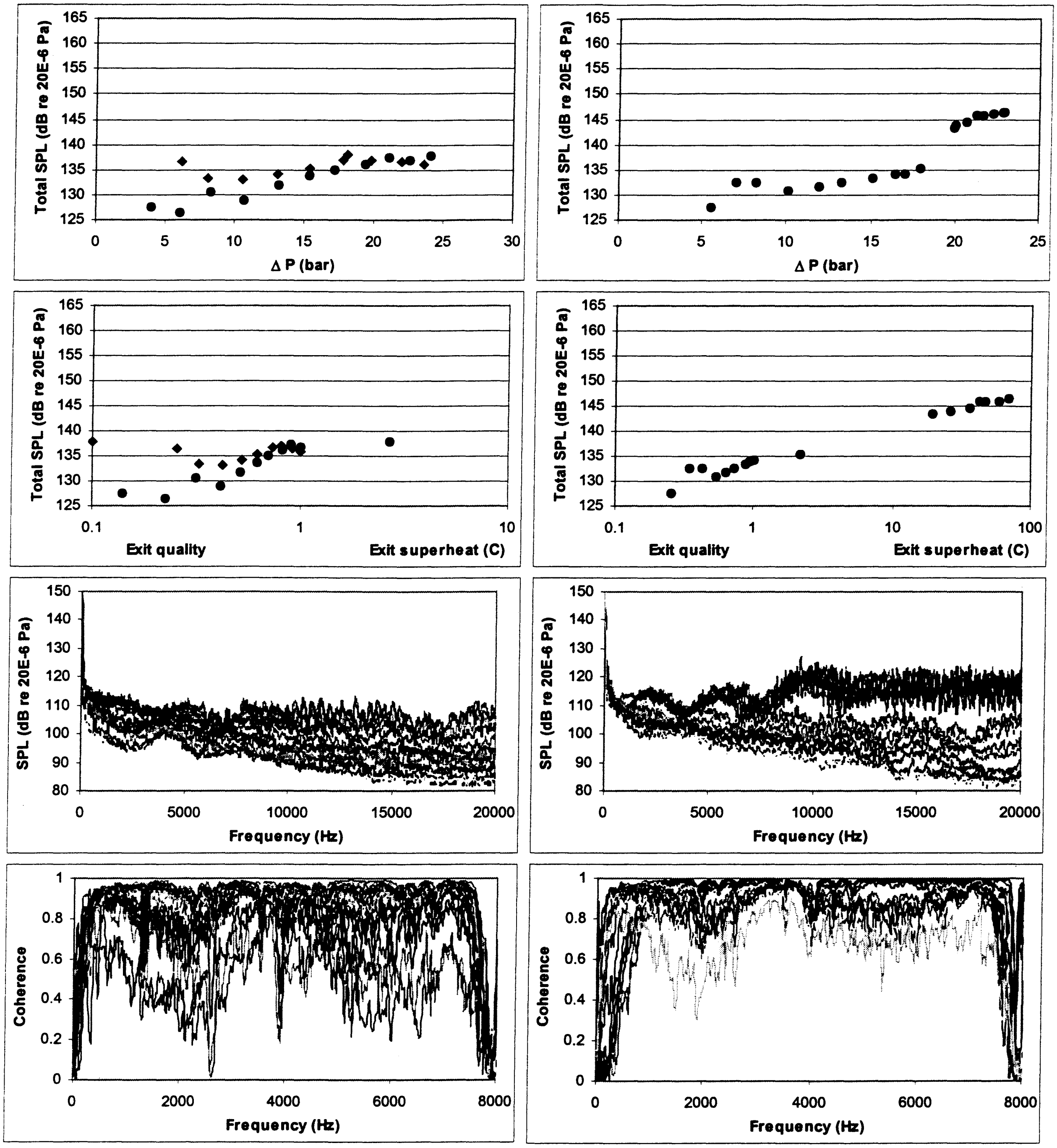

Figure K.6 - Brown orifice tube data with downstream screens
D=1.22mm, L=1.5in, Inlet and outlet screens
Left column: mass flow rate = 100lbm/hr, outlet pressure = 4bars
Right column: mass flow rate = 75lbm/hr, outlet pressure = 4bars

Table K.4 - Long capillary tube data
D=1.626mm, L=127in
Shading used to separate data sets

Inlet Pressure [bars]	Outlet Pressure [bars]	Inlet Superheat [C]	Oulet Superheat [C]	Inlet Quality [-]	Outlet Quality [-]	Mass flow rate [lbm/hr]	TS exit Temp. [C]	TSPL re 20E-6 Pa [dB]
27.49	3.82	-66.50	two-phase	liquid	0.06	194.53	6.86	135.13
28.03	3.97	-55.34	two-phase	liquid	0.16	184.11	8.13	136.31
28.48	4.08	-40.53	two-phase	liquid	0.27	166.50	8.80	140.02
27.77	4.18	-18.46	two-phase	liquid	0.45	134.99	9.66	144.27
29.98	5.35	38.54	56.14	vapor	vapor	48.32	36.70	151.01
29.79	5.30	21.46	38.67	vapor	vapor	50.38	34.79	151.76
29.85	5.30	10.64	25.50	vapor	vapor	53.77	30.79	152.51
29.67	5.26	2.30	13.27	vapor	vapor	57.74	27.97	153.25
29.56	5.24	two-phase	6.15	1.00	vapor	57.99	24.45	152.20
29.56	5.24	two-phase	0.95	1.00	vapor	57.83	21.26	147.85
29.11	4.27	-10.22	two-phase	liquid	0.56	121.01	10.21	145.12
29.97	4.28	-4.12	two-phase	liquid	0.64	108.52	10.35	144.80
29.40	4.37	two-phase	two-phase	0.22	0.73	87.43	10.89	144.82
29.97	4.55	two-phase	two-phase	0.54	0.89	71.31	12.36	143.67
29.68	4.73	two-phase	two-phase	0.81	1.00	62.54	13.50	144.26
29.32	5.26	two-phase	0.85	1.00	vapor	59.81	17.11	144.94
29.66	4.00	-70.18	two-phase	liquid	0.06	197.18	8.08	133.93
29.75	4.09	-58.31	two-phase	liquid	0.15	191.72	8.79	136.95
29.81	4.15	-48.31	two-phase	liquid	0.22	182.37	9.39	137.67
30.00	4.23	-34.29	two-phase	liquid	0.34	164.76	10.12	142.25
29.51	4.34	-22.18	two-phase	liquid	0.44	142.59	10.80	144.70
29.57	4.45	-11.10	two-phase	liquid	0.54	123.90	11.53	145.64
7.01	4.26	-9.07	two-phase	liquid	0.04	52.45	10.13	131.91
8.01	4.28	-3.44	two-phase	liquid	0.14	48.98	10.29	137.51
10.35	4.33	-2.39	two-phase	liquid	0.23	52.20	10.49	140.53
13.27	4.40	-1.33	two-phase	liquid	0.35	52.45	11.14	138.82
29.92	7.02	14.33	23.97	vapor	vapor	51.79	32.71	147.60
29.04	6.98	9.44	17.87	vapor	vapor	51.29	30.76	147.28
28.20	6.94	4.08	9.21	vapor	vapor	49.89	28.54	146.98
27.63	6.47	0.10	-0.37	vapor	vapor	50.80	23.24	142.51
27.03	5.47	two-phase	0.22	1.00	vapor	51.46	17.96	142.04
25.97	5.24	two-phase	two-phase	0.71	0.94	52.86	16.29	140.99
24.53	5.23	two-phase	two-phase	0.55	0.84	51.96	16.57	139.64
22.09	5.01	two-phase	two-phase	0.42	0.74	50.22	15.15	139.62
18.88	5.05	two-phase	two-phase	0.19	0.53	54.68	15.43	138.81
16.17	5.08	two-phase	two-phase	0.13	0.44	52.45	15.61	139.92

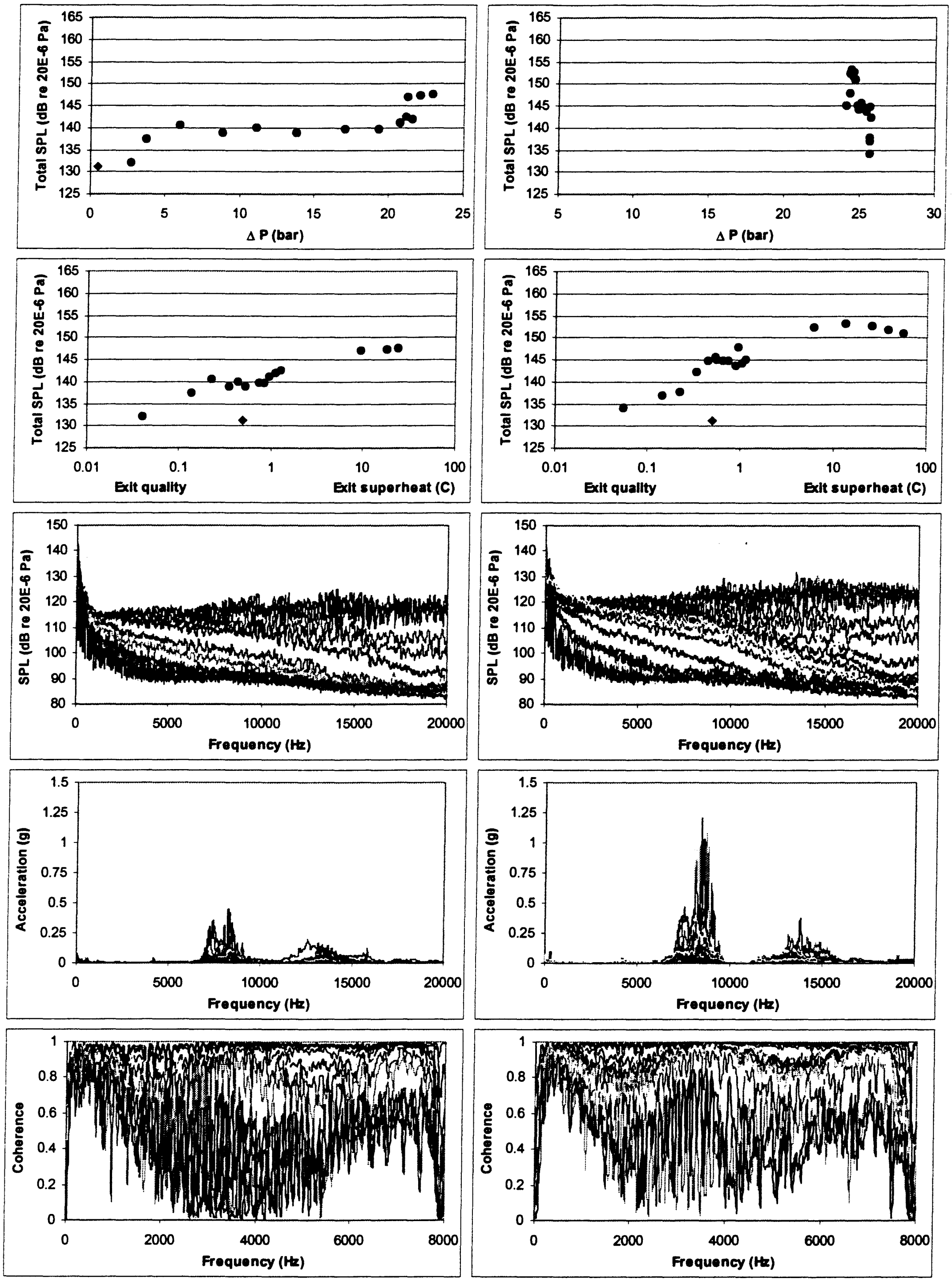

Figure K.7 - Long capillary tube data
D=1.626mm, L=127in
Left column: Mass flow rate = 50lbm/hr
Right column: Inlet pressure = 29bars

Table K.5 - Mid-length capillary tube data
D=1.626mm, L=64in
Shading used to separate data sets

Inlet Pressure [bars]	Outlet Pressure [bars]	Inlet Superheat [C]	Oulet Superheat [C]	Inlet Quality [-]	Outlet Quality [-]	Mass flow rate [lbm/hr]	TS exit Temp. [C]	TSPL re 20E-6 Pa [dB]
10.21	3.61	-13.34	two-phase	liquid	0.16	100.13	5.81	130.20
12.03	3.73	-8.70	two-phase	liquid	0.24	100.60	6.71	134.99
14.79	3.97	-5.03	two-phase	liquid	0.33	100.84	8.57	139.00
17.85	4.12	two-phase	two-phase	0.00	0.44	100.34	9.92	141.54
18.10	4.21	two-phase	two-phase	0.05	0.45	100.32	10.28	141.26
21.79	5.07	two-phase	two-phase	0.10	0.52	99.93	16.18	142.62
25.31	6.03	two-phase	two-phase	0.20	0.62	100.05	21.19	143.65
28.67	7.74	two-phase	two-phase	0.36	0.71	99.53	30.46	143.49
8.22	3.80	-8.27	two-phase	liquid	0.12	76.61	7.34	133.40
10.33	4.05	-2.94	two-phase	liquid	0.23	76.04	9.12	137.01
13.50	4.51	two-phase	two-phase	0.05	0.34	74.53	12.44	140.47
16.35	5.19	two-phase	two-phase	0.11	0.42	74.51	16.84	136.83
19.61	6.19	two-phase	two-phase	0.19	0.51	75.73	22.46	137.82
22.27	7.36	two-phase	two-phase	0.32	0.61	75.26	28.53	139.32
24.66	7.76	two-phase	two-phase	0.47	0.74	76.23	31.40	138.42
11.22	4.28	two-phase	two-phase	0.11	0.34	50.22	11.05	115.63
12.76	4.38	two-phase	two-phase	0.17	0.42	50.05	11.67	134.98
14.60	4.76	two-phase	two-phase	0.26	0.52	49.86	14.18	133.71
16.43	5.10	two-phase	two-phase	0.36	0.62	49.99	16.47	133.13
17.92	5.69	two-phase	two-phase	0.47	0.70	50.80	19.83	135.53
19.38	6.54	two-phase	two-phase	0.64	0.83	50.38	24.11	136.26
20.75	7.74	two-phase	two-phase	0.83	0.95	50.68	30.19	136.14
22.87	7.59	17.71	26.17	vapor	vapor	49.79	34.17	143.78
23.90	7.26	33.20	43.20	vapor	vapor	50.16	36.90	145.98
24.45	7.29	47.45	56.94	vapor	vapor	49.34	40.01	146.90
21.07	6.76	two-phase	1.19	1.00	vapor	49.93	25.61	140.47
20.80	5.77	two-phase	two-phase	0.93	1.00	50.53	19.55	140.27
19.12	4.66	two-phase	two-phase	0.66	0.88	49.16	13.63	136.20
18.84	4.45	two-phase	two-phase	0.61	0.85	50.05	12.46	136.77
17.87	4.35	two-phase	two-phase	0.47	0.73	51.34	11.54	134.94
16.30	4.21	two-phase	two-phase	0.39	0.66	49.31	10.54	133.93
14.51	3.96	two-phase	two-phase	0.24	0.53	51.30	8.58	135.10
12.78	3.89	two-phase	two-phase	0.15	0.42	51.88	8.04	136.50

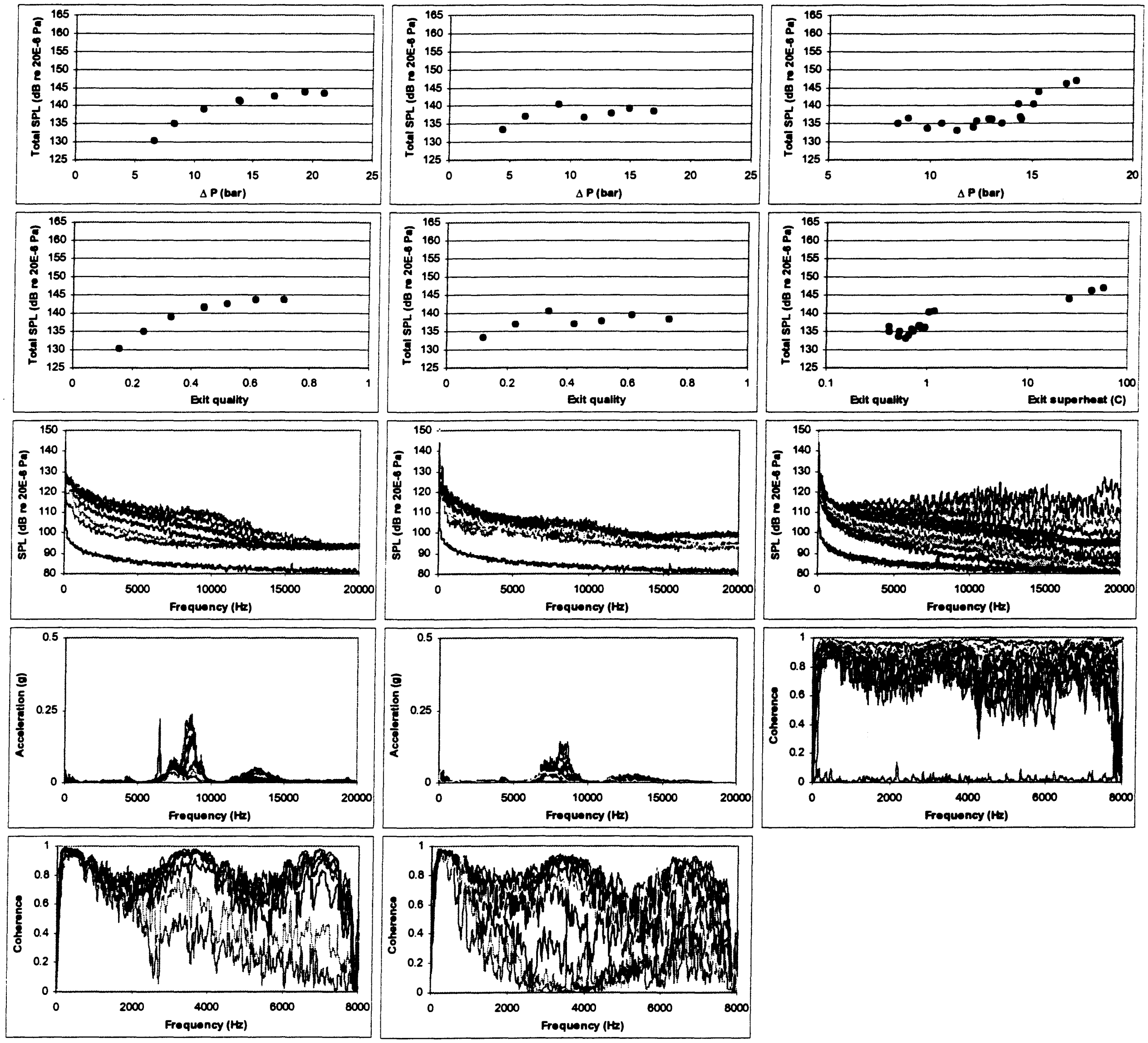

Figure K.8 - Mid-length capillary tube data
D=1.626mm, L=64in
Left column: mass flow rate = 100lbm/hr
Center column: mass flow rate = 75lbm/hr
Right column: mass flow rate = 50lbm/hr

Figure K.6 - Short capillary tube data
D=1.626mm, L=32in
Shading used to separate data sets

Inlet Pressure [bars]	Outlet Pressure [bars]	Inlet Superheat [C]	Oulet Superheat [C]	Inlet Quality [-]	Outlet Quality [-]	Mass flow rate [lbm/hr]	TS exit Temp. [C]	TSPL re 20E-6 Pa [dB]
30.77	5.36	6.20	25.81	vapor	vapor	100.81	34.23	161.80
29.41	5.33	1.59	17.91	vapor	vapor	99.63	29.78	160.05
28.49	5.02	two-phase	10.07	1.00	vapor	100.08	24.55	161.41
27.66	4.82	two-phase	2.27	0.99	vapor	100.52	18.30	153.46
26.88	4.62	two-phase	two-phase	0.88	1.00	100.47	13.29	152.87
25.61	4.24	two-phase	two-phase	0.70	0.96	99.83	10.62	151.67
24.54	4.10	two-phase	two-phase	0.54	0.86	100.34	9.56	149.76
23.12	4.26	two-phase	two-phase	0.40	0.76	100.54	10.65	148.17
21.27	4.10	two-phase	two-phase	0.29	0.67	100.09	9.64	146.11
18.88	4.00	two-phase	two-phase	0.18	0.56	100.14	8.91	144.36
16.79	4.00	two-phase	two-phase	0.11	0.47	99.38	8.84	141.63
14.28	3.96	two-phase	two-phase	0.04	0.37	100.47	8.45	139.80
25.63	4.45	22.57	50.95	vapor	vapor	74.56	40.49	159.03
24.85	4.41	13.68	39.20	vapor	vapor	74.52	36.63	158.83
23.94	4.36	5.67	28.44	vapor	vapor	74.60	31.71	158.61
22.03	4.19	two-phase	8.06	1.00	vapor	74.16	20.95	156.08
21.14	4.27	two-phase	2.02	0.84	vapor	75.38	11.46	148.00
20.25	4.10	two-phase	two-phase	0.72	0.94	74.09	9.78	146.06
19.63	3.93	two-phase	two-phase	0.62	0.87	74.89	8.35	145.20
18.52	4.21	two-phase	two-phase	0.47	0.75	74.95	10.40	142.45
17.35	4.22	two-phase	two-phase	0.39	0.67	74.42	10.46	140.25
15.76	4.21	two-phase	two-phase	0.26	0.56	74.57	10.37	138.24
13.99	4.24	two-phase	two-phase	0.17	0.45	75.40	10.56	136.12
12.46	4.24	two-phase	two-phase	0.12	0.38	74.43	10.62	133.91
10.35	4.23	two-phase	two-phase	0.05	0.27	74.71	10.49	137.96

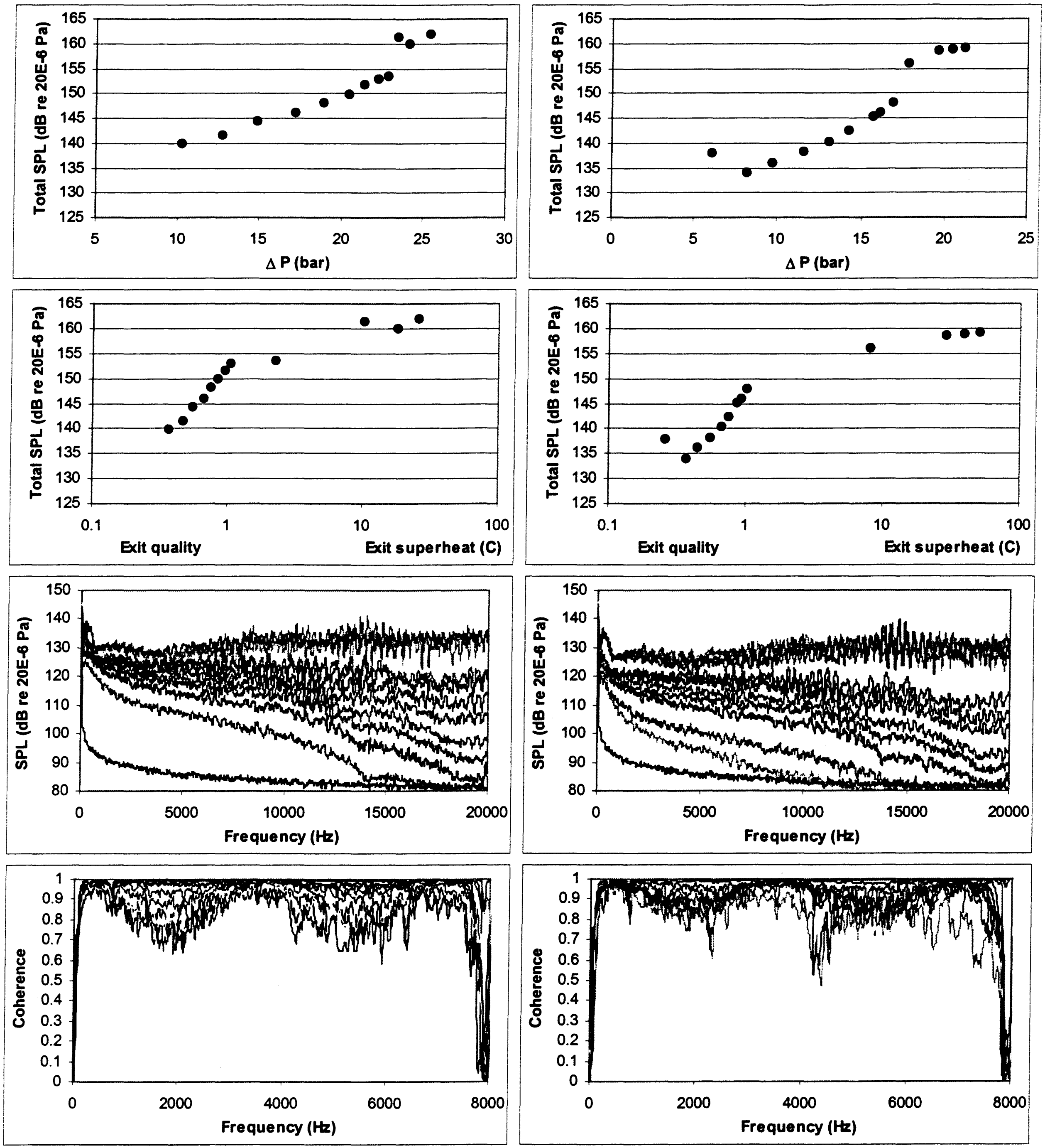

Figure K.9 - Short capillary tube data
D=1.626mm, L=32in
Left column: mass flow rate = 100lbm/hr, outlet pressure = 4bars
Right column: mass flow rate = 75lbm/hr, outlet pressure = 4bars

Table K.7 - Short capillary tube with 5 deg cone data
D=1.626mm, L=32in

Inlet Pressure [bars]	Outlet Pressure [bars]	Inlet Superheat [C]	Oulet Superheat [C]	Inlet Quality [-]	Outlet Quality [-]	Mass flow rate [lbm/hr]	TS exit Temp. [C]	TSPL re 20E-6 Pa [dB]
26.37	4.04	19.87	49.52	vapor	vapor	75.15	34.88	154.93
25.57	4.45	11.45	35.30	vapor	vapor	75.18	32.67	154.61
24.62	4.32	3.23	24.75	vapor	vapor	75.47	30.61	154.16
23.13	4.02	two-phase	3.80	1.00	vapor	75.07	19.30	145.33
21.77	3.95	two-phase	two-phase	0.79	1.00	74.96	9.73	140.52
20.80	4.36	two-phase	two-phase	0.65	0.89	74.66	11.79	142.48
19.68	3.97	two-phase	two-phase	0.53	0.81	73.61	9.58	139.89
18.17	4.55	two-phase	two-phase	0.37	0.66	75.68	13.24	136.89
16.26	4.19	two-phase	two-phase	0.27	0.57	74.99	11.53	132.97
14.43	3.86	two-phase	two-phase	0.18	0.49	74.70	9.00	130.02
12.51	4.89	two-phase	two-phase	0.09	0.33	75.66	13.68	129.36

Table K.8 - Short capillary tube with 10 deg cone data
D=1.626mm, L=32in

Inlet Pressure [bars]	Outlet Pressure [bars]	Inlet Superheat [C]	Oulet Superheat [C]	Inlet Quality [-]	Outlet Quality [-]	Mass flow rate [lbm/hr]	TS exit Temp. [C]	TSPL re 20E-6 Pa [dB]
25.70	4.10	13.09	40.05	vapor	vapor	74.64	32.94	153.91
27.44	4.14	36.03	68.59	vapor	vapor	74.47	41.66	155.15
26.80	4.45	23.67	52.44	vapor	vapor	75.25	39.00	154.22
25.61	4.12	11.63	38.31	vapor	vapor	75.28	34.06	155.13
22.20	4.24	two-phase	two-phase	0.81	1.00	75.17	11.96	150.00
21.12	4.12	two-phase	two-phase	0.66	0.91	75.05	10.86	149.02
19.84	3.96	two-phase	two-phase	0.51	0.80	75.15	9.73	147.79
18.29	3.76	two-phase	two-phase	0.39	0.70	74.93	8.63	144.92
16.29	4.54	two-phase	two-phase	0.26	0.56	74.95	13.12	141.96
14.59	4.25	two-phase	two-phase	0.18	0.47	74.36	11.53	139.85
12.82	4.38	two-phase	two-phase	0.11	0.38	75.08	11.40	137.30
10.73	4.35	two-phase	two-phase	0.04	0.27	74.34	11.96	135.51

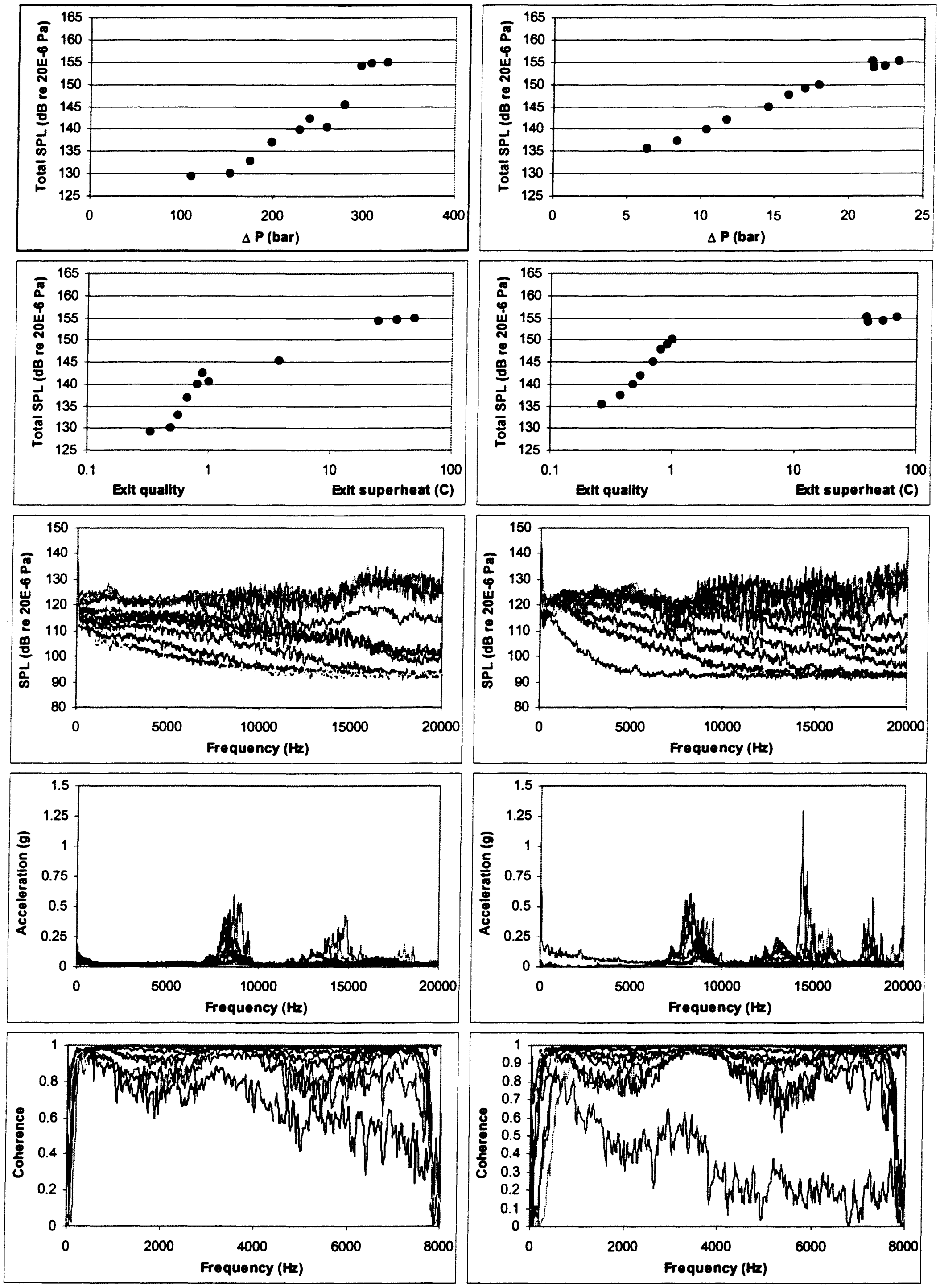

Figure K.10 - Short capillary tube data with outlet cones
D=1.626mm, L=32in
Left column: 5 degree cone
Right column: mass flow rate = 10 degree cone

Figure K.9 - Aluminum capillary tube data
D=1.91mm, L=68in
Shading used to separate data sets

Inlet Pressure [bars]	Outlet Pressure [bars]	Inlet Superheat [C]	Oulet Superheat [C]	Inlet Quality [-]	Outlet Quality [-]	Mass flow rate [lbm/hr]	TS exit Temp. [C]	TSPL re 20E-6 Pa [dB]
25.33	3.98	23.71	52.88	vapor	vapor	74.57	36.87	158.51
24.72	4.03	13.69	40.94	vapor	vapor	74.99	33.87	158.09
24.06	3.82	6.03	31.89	vapor	vapor	74.95	29.89	156.72
23.21	4.40	two-phase	18.40	1.00	vapor	75.11	25.57	155.56
22.89	4.21	two-phase	15.06	1.00	vapor	74.90	23.24	156.64
22.43	4.10	two-phase	2.51	0.94	vapor	75.05	16.52	148.09
22.00	4.03	two-phase	two-phase	0.85	1.00	74.52	13.54	146.98
21.76	4.15	two-phase	two-phase	0.77	0.98	74.85	10.19	147.39
21.06	4.02	two-phase	two-phase	0.62	0.89	74.69	9.74	145.93
19.91	3.80	two-phase	two-phase	0.51	0.80	75.43	8.10	144.40
18.45	3.88	two-phase	two-phase	0.39	0.70	74.55	9.10	141.81
16.58	3.68	two-phase	two-phase	0.26	0.59	74.84	7.58	138.88
14.45	3.84	two-phase	two-phase	0.17	0.48	74.48	9.35	138.08
12.52	4.24	two-phase	two-phase	0.08	0.35	75.52	10.62	142.16
10.83	4.28	two-phase	two-phase	0.04	0.27	75.20	11.25	139.95
9.20	4.15	two-phase	two-phase	0.00	0.19	75.80	10.98	136.27
30.45	4.32	4.62	26.56	vapor	vapor	99.92	28.69	161.26
28.76	4.05	two-phase	13.74	1.00	vapor	100.12	21.48	160.57
28.18	3.97	two-phase	3.71	0.92	vapor	103.78	13.01	153.65
27.55	4.31	two-phase	3.20	0.88	vapor	100.46	11.30	152.79
26.90	3.92	two-phase	two-phase	0.73	0.99	100.24	9.29	151.97
26.25	3.74	two-phase	two-phase	0.62	0.93	100.54	7.86	152.02
25.15	4.50	two-phase	two-phase	0.49	0.82	100.49	11.90	150.05
23.45	4.34	two-phase	two-phase	0.34	0.72	100.60	11.89	149.06
21.35	4.02	two-phase	two-phase	0.23	0.63	100.50	9.96	147.04
18.49	4.69	two-phase	two-phase	0.13	0.49	99.78	13.20	144.17
16.92	3.88	two-phase	two-phase	0.09	0.46	99.18	9.94	141.54
14.21	4.03	two-phase	two-phase	0.03	0.36	100.24	9.31	142.39
11.80	3.81	two-phase	two-phase	0.00	0.28	99.65	8.42	142.47

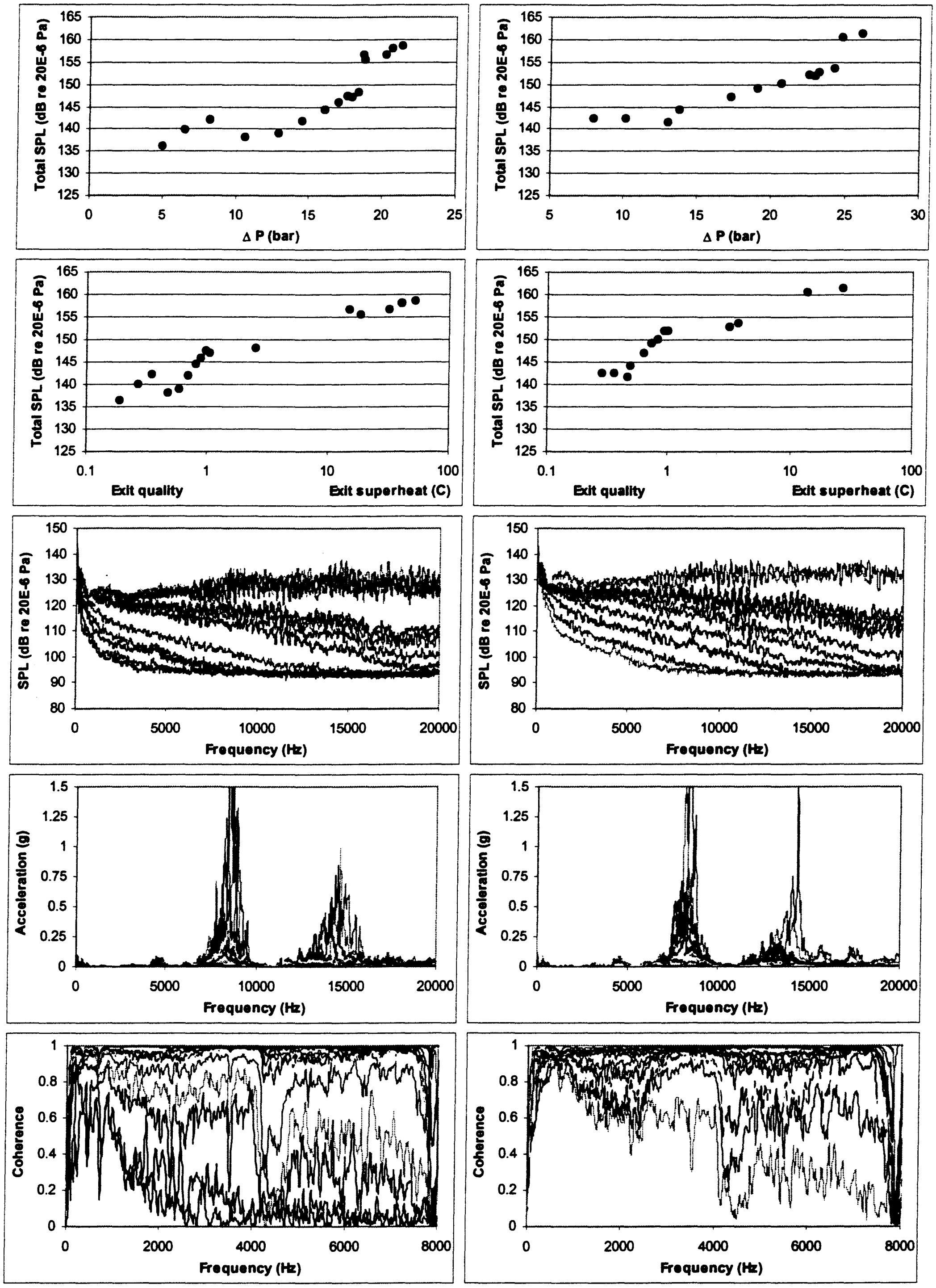

Figure K.11 - Aluminum capillary tube data
D=@mm, L=68in
Left column: mass flow rate = 75lbm/hr, outlet pressure = 4bars
Right column: mass flow rate = 100lbm/hr, outlet pressure = 4bars

Figure K.10 - Thermostatic expansion valve data
Shading used to separate data sets

TXV	Inlet Pressure [bars]	Outlet Pressure [bars]	Inlet Superheat [C]	Oulet Superheat [C]	Inlet Quality [-]	Outlet Quality [-]	Mass flow rate [lbm/hr]	TS exit Temp. [C]	TSPL re 20E-6 Pa [dB]
1	21.69	4.73	10.65	32.99	vapor	vapor	110.71	33.47	157.87
1	20.78	4.35	45.81	73.61	vapor	vapor	90.07	54.71	156.21
1	7.97	5.20	41.66	21.25	vapor	vapor	35.44	33.59	157.51
1	17.29	3.95	47.46	71.54	vapor	vapor	77.41	49.41	154.92
1	17.51	3.95	19.32	44.17	vapor	vapor	82.89	38.00	154.73
1	14.34	3.68	60.61	79.06	vapor	vapor	59.67	44.93	153.41
1	13.63	3.73	3.93	22.86	vapor	vapor	69.83	28.91	153.55
1	14.53	3.76	18.61	39.48	vapor	vapor	67.34	32.25	153.86
1	13.43	3.77	two-phase	2.97	0.93	vapor	82.40	7.60	148.50
1	9.09	3.65	39.98	48.02	vapor	vapor	40.52	29.88	149.00
1	23.30	6.88	18.77	35.94	vapor	vapor	111.51	46.75	158.07
1	22.70	7.02	two-phase	1.91	1.00	vapor	128.85	27.12	153.84
1	23.33	7.05	two-phase	7.15	1.00	vapor	121.78	30.74	156.50
1	17.11	7.13	55.27	61.69	vapor	vapor	73.42	50.08	153.19
1	17.17	7.49	18.74	28.40	vapor	vapor	81.50	42.72	153.37
1	16.58	7.56	two-phase	1.59	1.00	vapor	97.45	30.10	148.65
1	10.21	6.61	46.08	40.57	vapor	vapor	40.92	32.62	146.13
2	18.26	7.29	two-phase	two-phase	0.31	0.55	363.22	28.41	149.42
2	14.59	7.41	two-phase	two-phase	0.69	0.80	194.49	28.76	152.33
2	14.37	8.04	two-phase	two-phase	0.96	1.00	164.60	31.56	154.43
2	12.14	6.63	two-phase	two-phase	0.90	0.97	149.99	25.07	151.46
2	11.53	6.82	14.07	19.62	vapor	vapor	123.37	37.39	156.80
2	12.18	6.87	two-phase	7.13	1.00	vapor	135.13	29.17	157.01
2	9.91	6.38	37.16	40.25	vapor	vapor	92.76	44.35	154.90
2	10.12	6.54	10.09	15.65	vapor	vapor	99.94	33.64	154.92
2	10.10	6.79	two-phase	two-phase	0.72	0.78	107.92	27.35	153.72
2	9.03	6.88	36.50	34.76	vapor	vapor	78.41	40.12	151.18
2	9.39	7.59	12.06	12.02	vapor	vapor	74.72	32.59	149.55
2	11.37	4.63	27.23	42.65	vapor	vapor	115.89	41.50	158.86
2	11.14	4.14	9.88	27.94	vapor	vapor	115.79	31.80	159.27
2	10.88	4.06	two-phase	11.41	1.00	vapor	119.28	21.30	159.40
2	10.62	4.05	two-phase	4.51	1.00	vapor	121.38	14.55	152.94
2	7.50	4.01	two-phase	two-phase	0.57	0.66	82.99	17.85	152.38
2	7.74	4.00	26.82	36.92	vapor	vapor	77.81	32.30	153.53
3	8.19	4.06	two-phase	two-phase	0.77	0.86	100.13	10.17	145.25
3	8.65	4.14	two-phase	two-phase	0.89	0.97	99.93	10.57	147.20
3	9.12	4.09	two-phase	3.83	1.00	vapor	100.47	17.54	150.04
3	8.03	4.09	two-phase	two-phase	0.73	0.82	100.00	10.57	145.15
3	7.63	4.09	two-phase	two-phase	0.64	0.73	99.95	10.14	143.63
3	7.22	4.15	two-phase	two-phase	0.54	0.63	100.32	10.43	142.63
3	6.83	4.34	two-phase	two-phase	0.45	0.52	100.07	12.03	141.98
3	6.28	4.25	two-phase	two-phase	0.37	0.43	99.79	11.44	142.55
3	5.92	4.32	two-phase	two-phase	0.27	0.33	100.71	11.83	140.53
3	5.77	4.47	two-phase	two-phase	0.19	0.24	100.44	12.81	139.37
3	11.52	4.34	two-phase	5.49	1.00	vapor	101.33	18.92	152.34

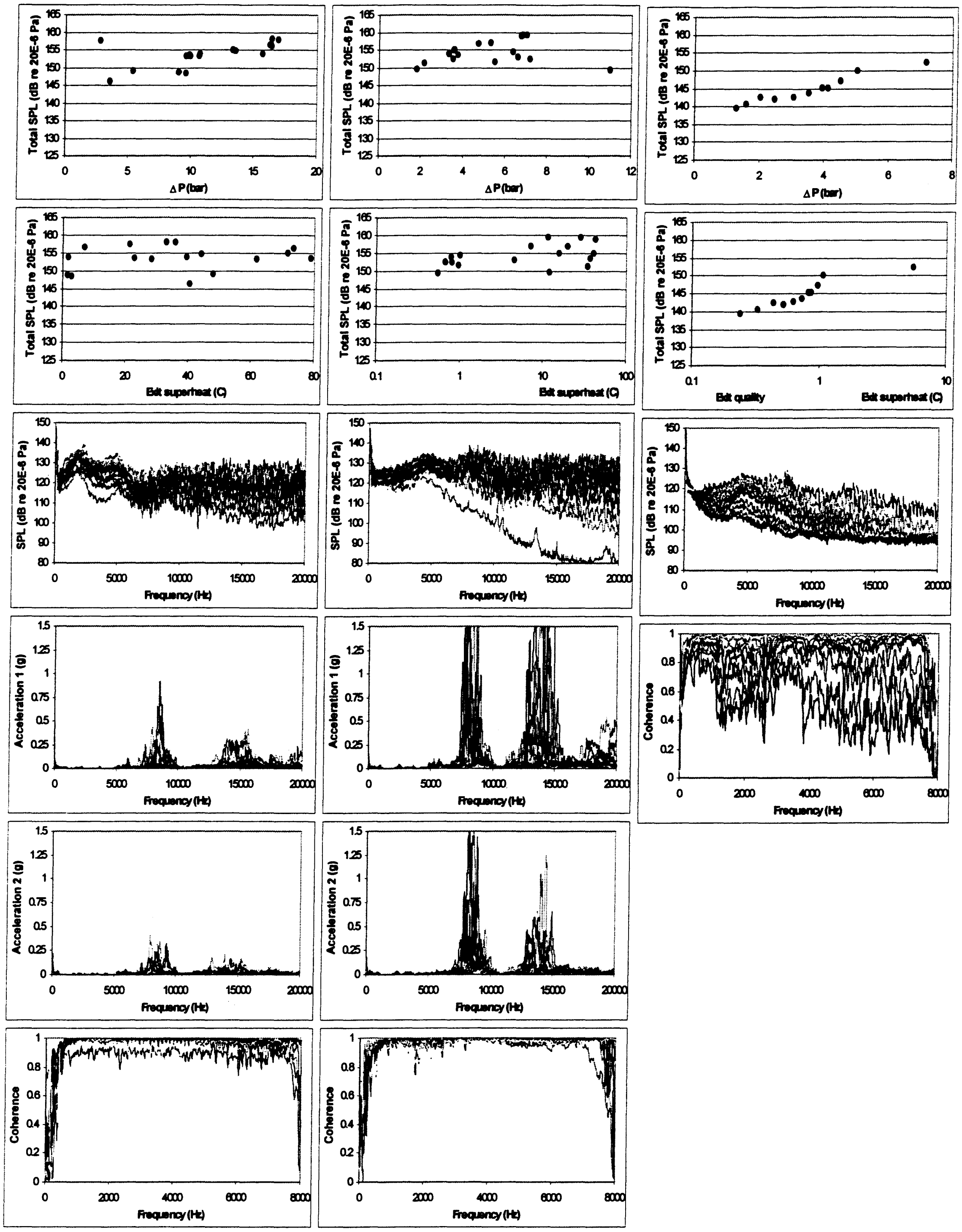

Figure K.12 - Thermostatic expansion valve data
Left column: TXV1
Center column: TXV2
Right column: TXV3, mass flow rate = 100lbm/hr, outlet pressure = 4bars

Table K.11 - Electronic expansion valve data
Shading used to separate data sets

Orifice	Inlet	Outlet	Inlet	Oulet	Inlet	Outlet	Mass flow	TS exit	TSPL
Opening	Pressure	Pressure	Superheat	Superheat	Quality	Quality	rate	Temp.	re 20E-6 Pa
[%]	[bara]	[bara]	[C]	[C]	[-]	[-]	[lbm/hr]	[C]	[dB]
35	21.62	3.83	19.87	50.63	vapor	vapor	100.37	38.50	150.39
35	21.54	3.69	19.25	51.88	vapor	vapor	100.39	39.00	150.55
35	20.93	3.92	9.39	37.00	vapor	vapor	100.31	31.29	150.58
35	21.01	3.96	10.88	38.55	vapor	vapor	100.11	32.87	150.55
35	19.94	3.85	two-phase	20.77	1.00	vapor	100.40	24.74	148.05
35	18.86	4.01	two-phase	3.62	0.93	vapor	101.48	18.11	140.83
35	18.00	3.90	two-phase	two-phase	0.86	1.00	100.19	10.80	138.97
35	17.09	4.01	two-phase	two-phase	0.77	0.95	99.77	10.18	137.22
35	16.09	3.87	two-phase	two-phase	0.67	0.87	100.23	9.44	137.46
35	15.03	4.12	two-phase	two-phase	0.57	0.78	99.16	10.27	136.55
35	13.64	3.98	two-phase	two-phase	0.45	0.68	99.63	9.47	135.41
35	12.14	3.83	two-phase	two-phase	0.34	0.56	100.42	8.31	133.61
35	10.94	3.64	two-phase	two-phase	0.25	0.48	99.97	7.94	132.51
35	9.22	3.88	two-phase	two-phase	0.18	0.36	99.76	9.37	133.27
35	7.82	3.74	two-phase	two-phase	0.11	0.27	99.82	7.42	132.81
20	28.85	3.99	29.03	61.90	vapor	vapor	74.36	39.87	148.40
20	27.31	4.04	13.75	42.35	vapor	vapor	75.58	35.57	148.53
20	27.31	4.03	13.65	41.77	vapor	vapor	75.43	34.88	148.41
20	25.12	3.97	two-phase	21.91	1.00	vapor	74.96	26.34	147.73
20	23.19	4.00	two-phase	2.70	0.95	vapor	75.35	17.74	136.41
20	21.53	3.95	two-phase	two-phase	0.77	0.99	75.62	9.32	133.68
20	20.70	4.16	two-phase	two-phase	0.70	0.93	75.88	10.02	134.20
20	19.25	4.35	two-phase	two-phase	0.60	0.84	74.97	11.25	133.95
20	17.61	4.12	two-phase	two-phase	0.48	0.75	74.89	10.44	130.81
20	15.86	3.85	two-phase	two-phase	0.38	0.66	74.57	8.52	130.89
20	14.15	4.11	two-phase	two-phase	0.31	0.57	74.85	10.08	133.64
20	12.00	3.84	two-phase	two-phase	0.22	0.47	75.03	8.44	131.83
20	9.97	3.79	two-phase	two-phase	0.17	0.38	73.75	8.89	134.48
20	8.21	3.56	two-phase	two-phase	0.09	0.27	74.90	6.67	133.40
20	30.98	4.13	two-phase	two-phase	0.50	0.88	120.47	9.87	136.64
20	27.81	4.02	two-phase	two-phase	0.41	0.82	121.37	9.63	135.45
20	24.71	3.84	two-phase	two-phase	0.32	0.74	119.20	8.56	135.39
20	21.84	4.17	two-phase	two-phase	0.23	0.63	119.28	10.60	136.22
20	18.72	3.87	two-phase	two-phase	0.15	0.54	121.09	8.69	137.24
20	15.73	3.96	two-phase	two-phase	0.10	0.45	119.86	9.76	135.53
20	12.65	4.17	two-phase	two-phase	0.05	0.33	119.90	10.28	134.82
20	10.30	3.96	two-phase	two-phase	0.02	0.25	119.64	9.36	133.49
10	30.61	4.00	two-phase	two-phase	0.40	0.84	76.14	9.87	130.34
10	27.26	3.85	two-phase	two-phase	0.31	0.76	75.27	8.93	133.18
10	23.81	3.90	two-phase	two-phase	0.23	0.67	75.30	9.35	134.88
10	19.45	3.81	two-phase	two-phase	0.15	0.55	75.35	8.67	137.40
10	16.28	4.13	two-phase	two-phase	0.09	0.44	74.79	10.27	137.50
10	12.93	3.88	two-phase	two-phase	0.04	0.35	75.15	9.06	131.68

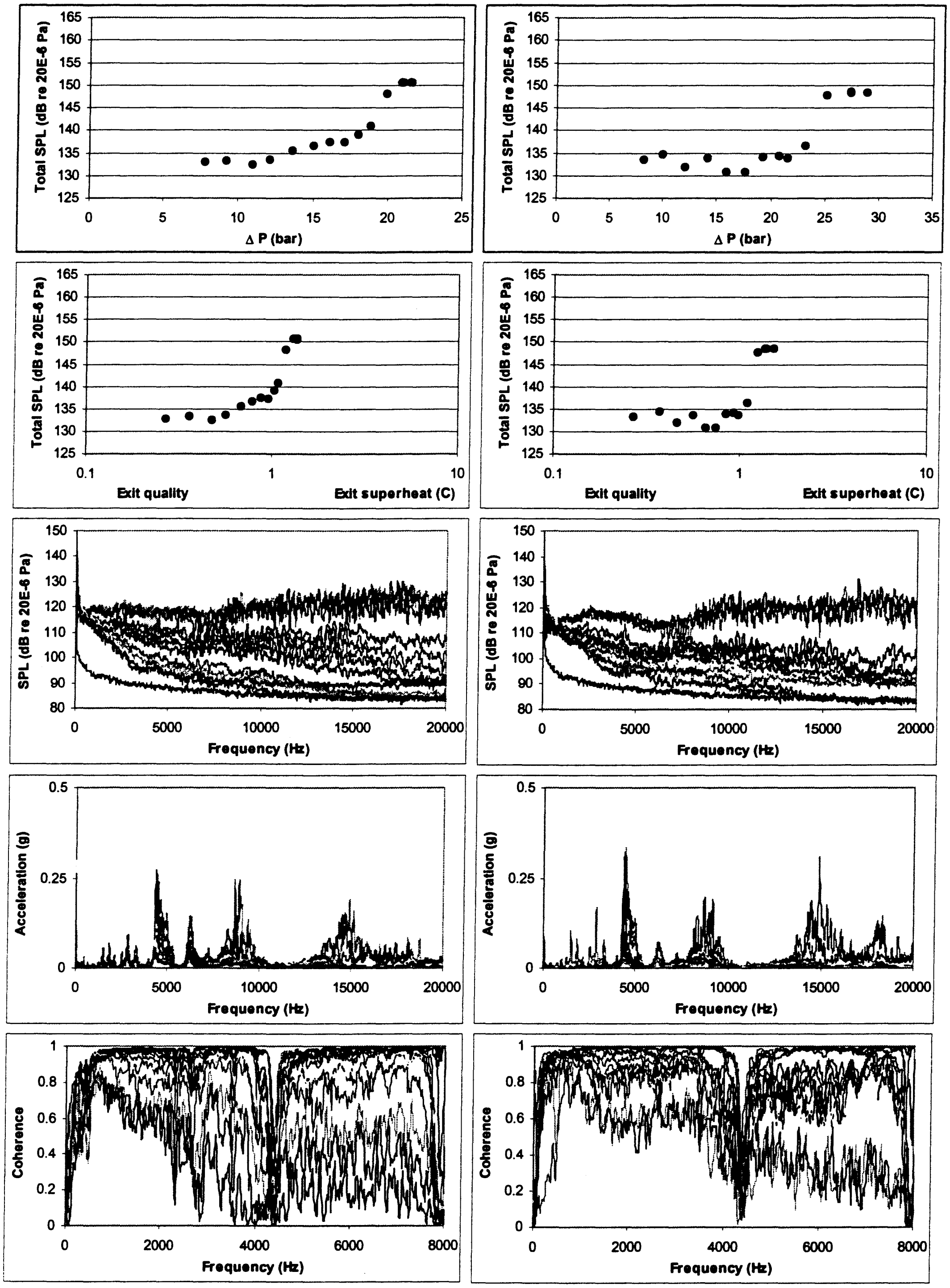

Figure K.13 - Electronic expansion valve data
Left column: mass flow rate = 100lbm/hr, outlet pressure = 4bars, valve opening = 35%
Right column: mass flow rate = 75lbm/hr, outlet pressure = 4bars, valve opening = 20%

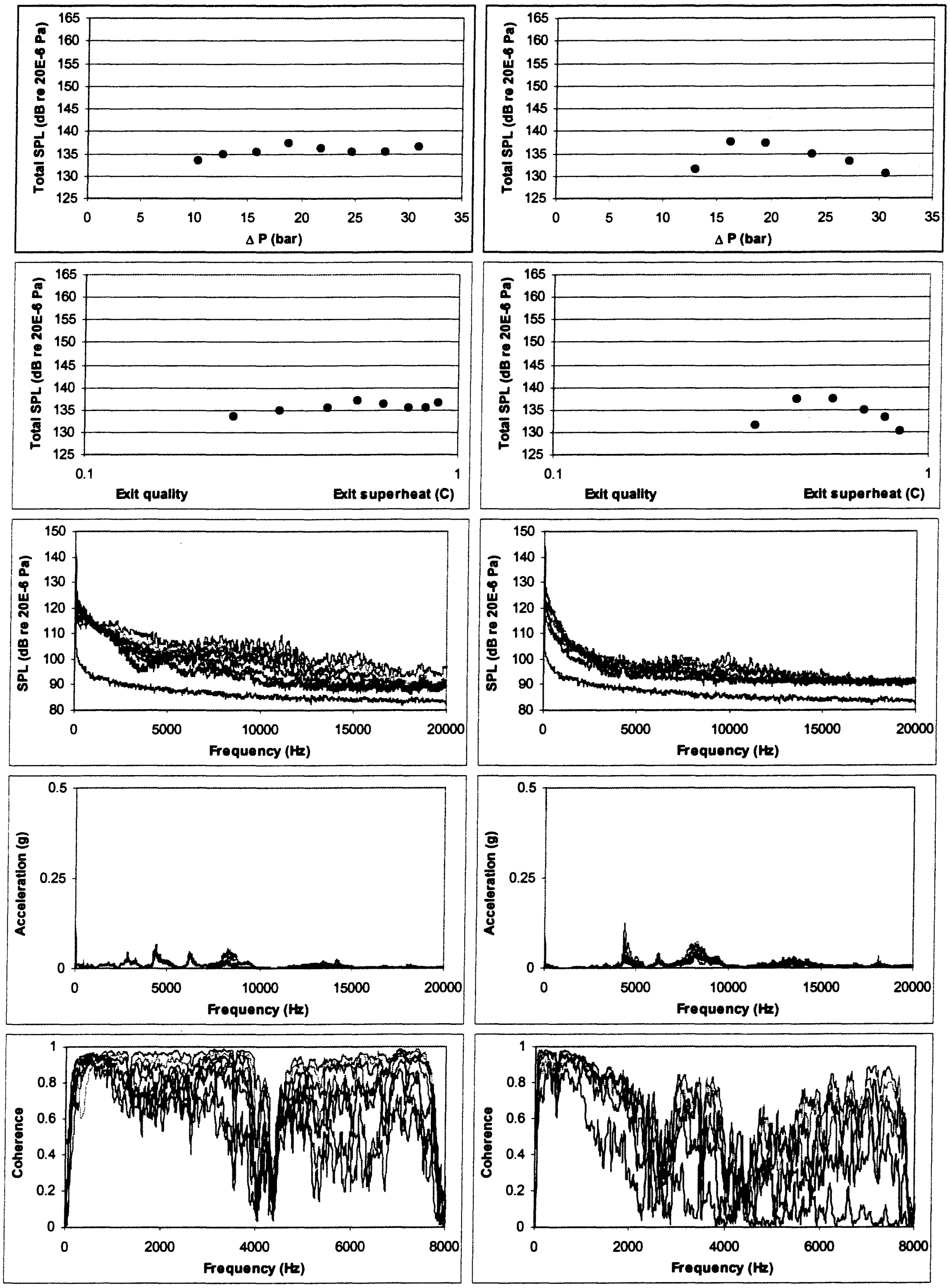

Figure K.14 - Electronic expansion valve data
Left column: mass flow rate = 120lbm/hr, outlet pressure = 4bars, valve opening = 20%
Right column: mass flow rate = 75lbm/hr, outlet pressure = 4bars, valve opening = 10%

Appendix L

Orifice and Capillary Tube Exit Pressure Calculations

L.1 Vapor flow

For pure vapor flow through the tube, exit-plane pressure calculations were done using Fanno-flow relations for a thermally and calorically perfect gas as given in [6]. The *EES* code is:

```
"Constants - Area, tube length, tube diameter"
A=piD^2/4 "m2"
D=DoConvert(mm,m)  "m"
L=LoConvert(in,m)  "m"

"Fanno relations to calculate friction factor and inlet M,
assuming choked ideal gas flow"
psi=1+(((gamma-1))/2)M^2
(4fL)/D=(1-
M^2)/(gammaM^2)+((gamma+1)/(2gamma))ln(M^2(2/(gamma+1)psi)^(-1))
M=(mdotConvert(lbm/hr,kg/s))/(rho_inc_inA)

"Calculate inlet entropy, density, ideal gas speed of sound,
ideal gas constant, and specific heat ratio"
s_in=Entropy(R134a,P=Pin,T=Tin) "kJ/kg-K"
rho_in=Density(R134a,P=Pin,s=s_in) "kg/m3"
c_in=sqrt(gammaR1000(Tin+273.15)) "m/s"
cp=Specheat(R134a,P=Pin,T=Tin) "kJ/kg-K"
R=8.314/MolarMass(R134a) "kJ/kg-K"
cv=cp-R
gamma=cp/cv

"Fanno relations to calculate exit pressure and temperature
assuming choked, ideal gas flow"
Pin=(Pexit/M)((2/(gamma+1))psi)^(-1/2) "bara"
(Tin+273.15)=(Texit/1)((2/(gamma+1))psi)^(-1) "K"

"Calculate exit entropy, density, and ideal gas speed of sound"
s_exit=Entropy(R134a,P=Pexit,T=(Texit-273.15)) "kJ/kg-K"
rho_exit=Density(R134a,P=Pexit,s=s_exit) "kg/m3"
c_exit=sqrt(gammaR1000Texit) "m/s"
```

(Unit settings: bar, C)

L.2 Two-phase flow

For two-phase flow through the tube, an adiabatic 1-D, finite difference, homogeneous flow model was used. The model uses *exactly* the same thermodynamic equations as the capillary tube model of [8] (except where noted) and assumes 100 finite-difference steps along the tube length. The model is based on 1-D conservation of mass, momentum, and energy, and assumes a choked, adiabatic capillary tube and homogeneous two-phase flow. The entrance loss coefficient, friction factor, and surface roughness are the only empirical parameters. Values or relations for all three of these parameters are recommended for capillary tubes in [8] based on studies of these parameters in capillary tubes as described in [8]. The full equations and development of the capillary tube model are well described in [8]. The EES code for the model used here, which is based on the capillary tube model of [8] is given below.

The present model applied the entrance loss coefficient, friction factor, and surface roughness recommended for capillary tubes to both the capillary tube and orifice tube data. The original model of [8] uses property tables which assume a linear change of h, s, and v with x, whereas the present model uses *EES* property calls. The original model also starts at the outlet and, assuming choked flow, marches backwards in pressure steps to the measured inlet conditions and length. The present model starts with the measured inlet conditions and length and marches along the tube in the direction of flow. Future work will include improving this model to check how close the calculated exit conditions are to the critical exit conditions for choked flow.

```
FUNCTION Enth(xin,Tin,Pin)
IF (xin>1) OR (xin<0) THEN Enth:=Enthalpy(R134a,P=Pin,T=Tin)
ELSE Enth:=Enthalpy(R134a,P=Pin,x=xin)
END

FUNCTION Visc(xin,Tin,Pin)
mu_v=viscosity(R134a,P=Pin,T=Temperature(R134a,P=Pin,x=0.5)+1)
mu_l=viscosity(R134a,P=Pin,T=Temperature(R134a,P=Pin,x=0.5)-1)
v_v=volume(R134a,P=Pin,x=1)
v_l=volume(R134a,P=Pin,x=0)
```

```
 IF (xin>1) OR (xin<0) THEN Visc:=Viscosity(R134a,P=Pin,T=Tin)
 ELSE Visc:=(xinv_vmu_v+(1-xin)v_lmu_l)/volume(R134a,P=Pin,x=xin)
 END

 "Inputs"
 e=12E-6 "in"

 "Constants"
A=pi(DConvert(in,m))^2/4 "m2"
mm=mdotConvert(lbm/hr,kg/s) "kg/s"
G=mm/A "kg/m2-s"
delx=LConvert(in,m)/100 "m"
Dp=(1.5(mm^2v[0]/2A^2))Convert(Pa,bar)

"0th step (Solve explicitely)"
P[0]=P_in-Dp "bara"
T[0]=T_in "C"
x[0]=x_in
h[0]=Enth(x_in,T_in,P_in) "kJ/kg"
v[0]=volume(R134a,P=P_in,h=h[0]) "m3/kg"
mu[0]=Visc(x_in,T_in,P_in)
Re[0]=(DConvert(in,m)G)/mu[0]
f[0]=0.25(Log10((e/D)/3.7+5.74/Re[0]^0.9))^(-2)
L[0]=0 "in"
s[0]=Entropy(R134a,P=P_in,h=h[0]) "kJ/kgK"

"nth steps (Solve simultaneously)"
Duplicate n=1,100
P[n]=(P[n-1]Convert(bar,Pa)-(delx((f[n]+f[n-1])/2)((v[n]+v[n-
      1])/2)G^2)/(2DConvert(in,m))-(G^2(v[n]-v[n-
      1])))Convert(Pa,bar) "bara"
h[n]=(h[n-1]1000+(-G^2/2)(v[n]^2-v[n-1]^2))/1000 "kJ/kg"
x[n]=Quality(R134a,P=P[n],h=h[n])
v[n]=volume(R134a,P=P[n],h=h[n]) "m3/kg"
T[n]=Temperature(R134a,P=P[n],h=h[n]) "C"
mu[n]=Visc(x[n],T[n],P[n])
Re[n]=(DConvert(in,m)G)/mu[n]
f[n]=0.25(Log10((e/D)/3.7+5.74/Re[n]^0.9))^(-2)
L[n]=(L[n-1]Convert(in,m)+delx)Convert(m,in) "in"
s[n]=Entropy(R134a,P=P[n],h=h[n]) "kJ/kgK"
End

P_exit=P[100]
T_exit=T[100]
x_exit=x[100]
```

```
s_exit=s[100]
s_in=s[0]
```

L.3 Notes

Data points which contained two-phase at the inlet and vapor flow at the exit of the tube could not be used in the model as given above. Exit pressures were not calculated for those points, which were a small number of the total number of data points (see Figure 6.10).